UNIVERSITÀ DEGLI STUDI DI PAVIA
DOTTORATO DI RICERCA IN FISICA - XXXVI CICLO

High precision theoretical predictions for the MUonE experiment

Ettore Budassi

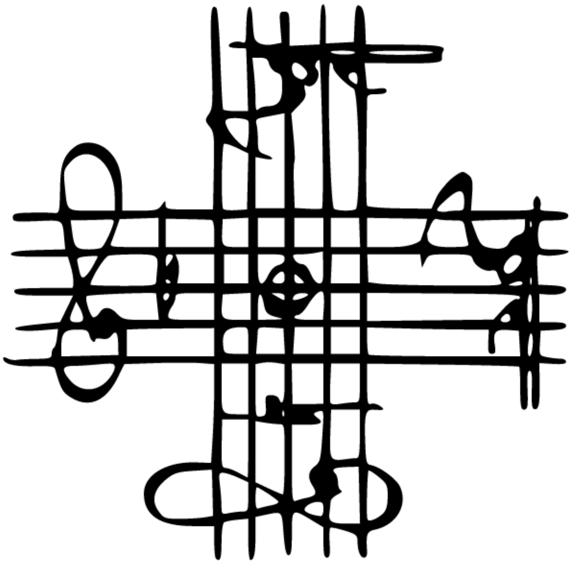

Tesi per il conseguimento del titolo

UNIVERSITÀ
DI PAVIA

Università degli Studi di Pavia

Dipartimento di Fisica

Dottorato di Ricerca in Fisica - XXXVI Ciclo

High precision theoretical predictions for the MUonE experiment

Ettore Budassi

Submitted to the Graduate School of Physics in partial fulfilment of the requirements for the degree of *Dottore di Ricerca in Fisica* at the University of Pavia

Alla nonna Zina —

Bina vides parvo discrimine iuncta sacella
altera pars Musis altera sacra Deo est

CONTENTS

ACKNOWLEDGEMENTS

I would like to wholeheartedly thank Dr. Carlo M. Carloni Calame for his support and help in these years.

Moreover, I express my most sincere indebtedness to Prof. Guido Montagna, Prof. Fulvio Piccinini and Prof. Oreste Nicrosini for their guidance and wise advices.

I also wish to thank all the colleagues without whom I could not have written this thesis: Dr. Clara Del Pio[1], Andrea Gurgone, Dr. Mauro Chiesa, Dr. Syed Mehedi Hasan, Prof. Giovanni Abbiendi, Dr. Riccardo Pilato and all the MUonE collaboration members.

Finally, I would like to thank my family and my close friends.

---

[1] At the time of printing, she will have already graduated as PhD.

NOTATIONS AND ABBREVIATIONS

All the acronyms that will be used in this thesis are defined:

1PI	One-Point-Irreducible
1pF	One-point Fermi
AGS	Alternating-Gradient Synchrotron
BAC	basic acceptance cuts
BMS	Beam Momentum Station
BMT	Bargmann–Michel–Telegdi
BNL	Brookhaven National Laboratory
CERN	Conseil Européen pour la Recherche Nucléaire
ChPT	Chiral Perturbation Theory
CM	center of mass
DHMZ	Davier–Hoecker–Malaescu–Zhang
DR	Dispersion Relation
ECAL	electromagnetic calorimeter
EDM	Electrical Dipole Moment
EM	electromagnetic
Eq.	Equation
EW	electroweak
FB	Fourier–Bessel
Fig.	Figure
FNAL	Fermi National Accelerator Laboratory
FS	final-state
FSR	Final State Radiation
HLbL	Hadronic Light-by-Light
HLO	Hadronic Leading Order
HOVP	Higher-Order Vacuum Polarisation
HVP	Hadronic Vacuum Polarisation

i.e.	id est
IB	Isospin-Breaking
IR	infrared
IS	initial-state
ISR	Initial State Radiation
IsSy	Isospin-Symmetric
J-PARC	Japan Proton Accelerator Research Complex
KLN	Kinoshita–Lee–Nauenberg
KNT	Keshavarzi–Nomura–Teubner
l.h.s.	left-hand side
LIPS	Lorentz-Invariant Phase Space
LO	Leading Order
MC	Monte Carlo
McMule	Monte Carlo for MUons and other LEptons
MCS	multiple Coulomb scattering
MESMER	Muon-Electron Scattering with Multiple Electromagnetic Radiation
MHO	modified harmonic oscillator
MI	Master Integral
N^{3}LO	Next-to-Next-to-Next-to-Leading Order
NLO	Next-to-Leading Order
NMR	Nuclear Magnetic Resonance
NNLO	Next-to-Next-to-Leading Order
NP	New Physics
PhSp	Phase Space
PID	particle identification
ppm	parts per million
pQCD	Perturbative Quantum Chromodynamics
PS	Parton Shower
QCD	Quantum Chromodynamics
QED	Quantum Electrodynamics
QED IB	Electromagnetic Isospin Breaking
QFT	Quantum Field Theory
r.h.s.	right-hand side
Ref.	Reference
rms	root-mean-square
SDR	Subtracted Dispersion Relation
Sec.	Section
SIB	Strong Isospin Breaking
SM	Standard Model
Tab.	Table
TI	Theory Initiative

UV	ultraviolet
VP	Vacuum Polarisation
w.r.t.	with respect to
WP	White Paper
YFS	Yennie–Frautschi–Suura

Furthermore, all the main pieces of notation are once-and-for-all set:

- Natural units are used: $c = \hbar = 1$
- Three-vectors are written in **boldface**: $\mathbf{p} = (p_1, p_2, p_3)$
- Four-vectors are written sans serif: $\mathsf{p} = (p_0, p_1, p_2, p_3)$
- The norm of a four-vector is always intended as the Minkowski norm, namely $\|\mathsf{p}\|^2 = p_0^2 - p_1^2 - p_2^2 - p_3^2$

INTRODUCTION

Subatomic particles exhibit a magnetic dipole moment that depends on their intrinsic properties, such as their electric charge, their mass and their spin. This quantity is expressed proportionally to the Bohr magneton. The proportionality constant is the gyromagnetic factor g which is an adimensional quantity. Studies on the value of the gyromagnetic factor of leptons started from the first developments of Quantum Electrodynamics (QED), in the 1920s. A calculation of the electron g was first addressed by Dirac in his relativistic generalisation of quantum mechanics. In agreement with previous experimental results he found that $g = 2$.

In the late 1940s, a measurement of the magnetic moment of the electron by Kusch and Foley as well as an independent calculation by Schwinger showed a discrepancy of about 0.12 % between what they found and the Dirac calculation of $g = 2$. This discrepancy is called *anomalous magnetic moment* and is defined as: $a = (g - 2)/2$.

The anomalous magnetic moment of the electron and of the muon have been treated with very high interest since the earliest developments of the Standard Model of particle physics (SM). This quantity has been studied both from the theoretical and from the experimental point of view becoming one of the fundamental quantities that are tested with the highest precision in particle physics.

From an experimental point of view, the latest measurement of the muon anomalous magnetic moment has been performed at Fermilab National Accelerator Laboratory (FNAL) by the E989 experiment in 2023 with the very high precision of 0.2 parts per million (ppm). The results from

E989 confirm earlier measurements by the E821 experiment, based at Brookhaven National Laboratory (BNL). The precision goal of the E989 experiment is of 0.14 ppm. Moreover, a new experiment is expected to start at J-PARC in the next few years. This experiment will be able to take new independent data on the same quantity.

From the theoretical point of view, the value of the muon anomalous magnetic moment is calculated within the framework of the SM. The contributions to a_μ can come from all the sectors of the SM: the QED, the weak and the strong sector. Since the 1960s, many theoretical contributions have been calculated with a very high level of precision. The most recent theoretical predictions for the muon anomalous magnetic moment have a relative error of about 0.4 ppm which is comparable to the experimental error by the BNL and FNAL collaborations.

However, the theoretical prediction and the experimental measurement of the muon anomalous magnetic moment are discrepant at the level of about 5 standard deviations. This is one of the largest deviations from a SM prediction seen in an electroweak observable. This is why the determination of a_μ is considered to be one of the most stringent tests for physics beyond the SM.

The accuracy of the SM predictions is limited by strong interaction effects, such as the Hadronic Leading Order (HLO) contributions and the Hadronic Light-by-Light (HLbL) contributions. The error on the HLO term is the largest. The standard way to calculate a_μ^{HLO} uses dispersive integrals together with *timelike* ($q^2 > 0$) experimental data coming from many different $e^+e^- \to$ hadrons experiments. This approach is complicated by the many hadronic resonances that are present in the low-energy region. However, very recently a new measurement of the pion electromagnetic form factor was performed by the CMD-3 collaboration. This measurement was performed using the $e^+e^- \to \pi^+\pi^-$ channel, which is the most important between all the $e^+e^- \to$ hadrons processes. The CMD-3 measurement is significantly discrepant from the previous measurements by all the other collaborations, in the direction that reduces the discrepancy with the experimental value of a_μ.

Moreover, in very recent years the a_μ^{HLO} contribution was calculated in the lattice Quantum Chromodynamics (QCD) framework. The results of these calculations have an accuracy level that is comparable to the *timelike* calculation. The central value of the lattice QCD calculation, when merged with the QED, weak and the other strong contributions to the muon anomaly, is closer to the experimental value that is measured at BNL and FNAL than the calculation that is performed using the *timelike* approach. At present, many research groups are looking at the calculation of a_μ^{HLO} with higher precision.

An alternative approach has been proposed to calculate the a_μ^{HLO} term in an independent way, using a *spacelike* ($q^2 < 0$) process. The main idea is to extract the hadronic contribution to the running of the fine structure constant $\Delta\alpha_{\text{had}}(t)$ from a scattering experiment. In this respect, an experimental proposal called MUonE has been made at CERN to measure $\Delta\alpha_{\text{had}}(t)$. The MUonE experiment is a fixed-target muon-electron scattering experiment with a 160 GeV high-intensity muon beam. The goal is to achieve a 0.3 % statistical uncertainty on a_μ^{HLO} in about 3 years of data taking, in order to make the MUonE determination competitive with the *timelike* and lattice QCD calculations of the HLO contributions to the muon $g-2$. This means that a precision goal of 10 ppm on the differential cross section is needed.

Given the very high precision that is required, a muon-electron scattering Monte Carlo (MC) event generator has to be developed for the analysis of experimental data as well as their correct interpretation. This MC is called MESMER and will need to include effects up to the Next-to-next-to-leading order (NNLO) and a resummation procedure, for example with a Parton Shower (PS) at leading-logarithm (LL) precision matched to the NNLO fixed-order calculation. Moreover, the determination of the main background processes needs to be performed. This will be crucial during the final data analysis procedure.

The MESMER MC event generator will be used for the template fit procedure that will be performed after data taking to extrapolate $\Delta\alpha_{\text{had}}(t)$ and also for the full simulation of all the physics contributions in the MUonE detector.

In this thesis, the latest calculations that were included in the MESMER MC event generator are described in detail and the numerical impact of these processes on the most important differential cross sections are shown. First, the calculation of the NNLO lepton pair contribution will be shown, along with their numerical impact. Then, the calculation of the $\mu e \to \mu e \pi^0$

cross section will be described, with the numerical impact on the differential observables for typical MUonE running conditions. Then, the calculation of the real lepton pair production from the scattering of a muon on a nucleus within the target will be detailed. The impact of this process on the differential observables will also be shown. The structure of the thesis follows.

In Chapter 1, an introduction on the muon anomalous magnetic moment is shown. The state of the art of the measurements and the calculations of a_μ is summarised.

Chapter 2 will be devoted to detailing the calculation of the HLO contribution, which is the main responsible for the theoretical error of the muon anomaly. Details on the *timelike* approach, the lattice QCD approach and the *spacelike* approach will be given.

Chapter 3 will be dedicated to the description of the MUonE experimental setup, how the systematic uncertainties are treated and the procedure to extract $\Delta\alpha_{\text{had}}$.

In Chapter 4, a review of the main calculations that were performed for the MUonE experiment will be discussed. First, all the older ones are summarised. Then, details on the calculations of higher-order corrections to μe scattering in the MESMER MC event generator will be given. A higher insight will be devoted to the NNLO lepton pair contributions and to the single neutral pion production from muon-electron scattering.

In Chapter 5, the main source of background of the MUonE experiment, namely the pair production from muon-nucleus scattering, will be investigated. Phenomenological results are shown for typical MUonE running conditions.

In Appendix A, a brief description of the MESMER MC event generator will be given, with attention on the input values, outputs and event generation details.

Chapter 1

The muon anomalous magnetic moment

The magnetic dipole moment of a particle is a fundamental physical quantity that links the spin angular momentum of such particle with its behaviour in an electromagnetic (EM) field. Since the earliest developments of Quantum Electrodynamics (QED), this quantity has been the focus of both theoretical and experimental investigation.

The first theoretical indication that the value of the electron gyromagnetic factor is $g_e = 2$ was given by Uhlenbeck and Goudsmit in 1925, and was later proved by Dirac in 1927. In 1949, Schwinger computed an anomaly with respect to (w.r.t.) Dirac's calculation. Since then, more precise and complex calculations to determine the electron and muon anomalous magnetic moments have been performed within all the sectors of the Standard Model (SM).

Simultaneously, a productive albeit very challenging experimental effort started in order to measure the anomalous magnetic moments of the electron and of the muon. Such an effort resulted in an emerging discrepancy between the theoretical prediction and the experimental measurement of the muon anomalous magnetic moment.

In this chapter, the muon anomalous magnetic moment a_μ will be defined. Then, a complete overview of the main experimental measurements of a_μ will be shown, with due focus on the latest and most precise results. After that, the SM calculations of the same quantity will be sketched and, in the end, compared to the experimental results.

1.1 The anomalous magnetic moment

Subatomic particles of the SM that have electric charge, mass and spin exhibit a magnetic dipole moment. In classical electrodynamics, a magnetic dipole moment is generated as a charged particle rotates around an axis, thus gaining an angular momentum $\mathbf{L} = m\mathbf{r} \times \mathbf{v}$, where m is its mass. Let Qe be the charge of such particle, the magnetic dipole moment $\boldsymbol{\mu}_m$ is

$$\boldsymbol{\mu}_m = g\frac{Qe}{2m}\mathbf{L}, \tag{1.1}$$

where g is the gyromagnetic factor, and $g = 1$.

At the beginning of the 1920s, it was discovered that quantum particles possess intrinsic spin angular momentum and that their spectrum is quantised (Otto Stern and Walther Gerlach, 1922 [1]) and it was later postulated without proof that the electron had a spin quantum number equal to 1/2 (George Uhlenbeck and Samuel Goudsmit, 1925 [2]). These two results required that the gyromagnetic factor of an electron must be equal to 2. Similarly as in Eq. 1.1, by considering a particle with a spin angular momentum $\mathbf{S} = \boldsymbol{\sigma}/2$ one can define a magnetic dipole moment

$$\boldsymbol{\mu}_m = g\frac{Qe}{2m}\frac{\boldsymbol{\sigma}}{2} \tag{1.2}$$

that for an electron becomes

$$\boldsymbol{\mu}_m = -g\mu_B\frac{\boldsymbol{\sigma}}{2}. \tag{1.3}$$

That is, the gyromagnetic factor g is the proportionality constant between the electron's dipole moment and its spin, in units of the Bohr magneton $\mu_B = e/2m_e$.

Dirac, in 1928, proved that indeed for an electron $g = 2$ [3]: this can be derived from the non-relativistic limit of the Dirac equation, with a non-null EM field $A^\mu(x) = (\varphi, \mathbf{A}) \neq 0$ (Pauli equation):

$$i\hbar\frac{\partial\varphi}{\partial t} = \left[\frac{1}{2m}\left(-i\boldsymbol{\nabla} + e\mathbf{A}\right)^2 - e\Phi + \frac{e}{2m}\boldsymbol{\sigma}\cdot\mathbf{B}\right]\varphi. \tag{1.4}$$

This equation is the non-relativistic Schrödinger equation up to the last spin term which is the potential of a magnetic dipole in an external magnetic field.

In the realm of the SM, to keep track of the full behaviour of a lepton in an external magnetic field, one needs to keep into account all the higher-order contributions. Any non-zero contribution to the lepton's magnetic moment will change the value of the gyromagnetic ratio: thus, one can define the lepton's anomaly as

$$a_\ell = \frac{g_\ell - 2}{2} \tag{1.5}$$

which is the relative discrepancy between the particle's gyromagnetic ratio and Dirac's calculation of $g_\ell = 2$.

For the first time, in 1949 J. S. Schwinger computed an anomaly for the electron [4], confirming a previous measurement by Kusch and Foley [5]: he considered the first higher-order term in the expansion in the fine structure constant α of the electron-photon interaction vertex function in QED. In the end, the electron anomalous magnetic moment at order α in QED amounts to

$$a_e = \frac{\alpha}{2\pi}. \tag{1.6}$$

Such a calculation can be easily generalised to the $\mathcal{O}(\alpha)$ contribution to the muon anomalous magnetic moment a_μ, in QED. Throughout the years, many more higher-order contributions to a_μ have been computed. All the currently known SM contributions to a_μ will be described in Sec. 1.3.

1.2 Measurements of a_μ

From now on, the discussion will be reserved to the anomalous magnetic moment of the muon.

1.2.1 Principle of a_μ experiments

This section will be devoted to understanding the working principle of the most recent muon anomalous magnetic moment experiments: E821 at Brookhaven National Laboratory (BNL) and E989 at Fermi National Accelerator Laboratory (FNAL). A review of all the muon anomalous magnetic moment measurements will be shown in the next section, as well as the idea behind future a_μ experiments.

All the most recent experiments that aim to measure the muon anomalous magnetic moment work in a very similar fashion. They exploit the dynamics of a beam of polarised muons in a magnetic storage ring.

A beam of protons is accelerated and stored in an Alternating-Gradient Synchrotron (AGS). Then, it scatters on a target, producing pions. These particles are unstable and undergo weak decay into muons with the production of a muon neutrino: $\pi \to \mu + \nu_\mu$. The muons carry a spin and, as seen in Sec. 1.1, a magnetic moment that is parallel to the muons' direction of motion. The polarised muons have a definite velocity $\mathbf{v}$. When they enter a region with a uniform magnetic field $\mathbf{B} \perp \mathbf{v}$, their trajectory becomes circular and they can be stored in a magnetic storage ring. Such a circular motion has a characteristic frequency, called *cyclotron frequency*, that depends on the muon charge, mass and velocity, and on the external magnetic field:

$$\boldsymbol{\omega}_c = \frac{e\mathbf{B}}{m_\mu \gamma}, \tag{1.7}$$

where $\gamma = 1/\sqrt{1 - |\mathbf{v}|^2}$ is the Lorentz factor of the muons. In addition to the circular motion of the muon, one must take into account the motion of the spin angular momentum in a homogeneous magnetic field. This precession motion has frequency $\boldsymbol{\omega}_s$:

$$\boldsymbol{\omega}_s = \frac{e\mathbf{B}}{m_\mu \gamma} + a_\mu \frac{e\mathbf{B}}{m_\mu}. \tag{1.8}$$

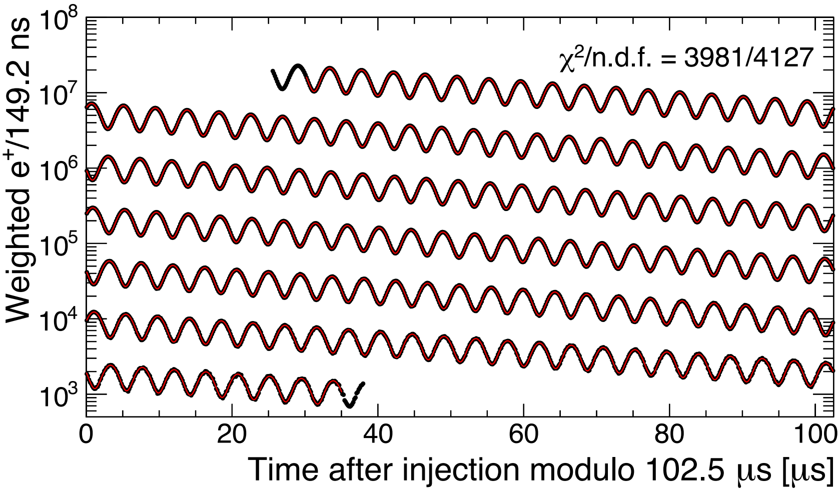

Figure 1.1: Asymmetry-weighted time spectrum for e^+ emission (black) and its fit function (red), obeying Eq. 1.13 [6].

By measuring the quantity

$$\boldsymbol{\omega}_a = \boldsymbol{\omega}_s - \boldsymbol{\omega}_c = a_\mu \frac{e\mathbf{B}}{m_\mu} \tag{1.9}$$

and the magnetic field $\mathbf{B}$ via Nuclear Magnetic Resonance (NMR), one can determine the muon anomaly a_μ.

Inside the muon storage ring, an electric quadrupole field $\mathbf{E}$ is applied to the muon beam in order to keep it as focused as possible. The dynamics of the muons is thus changed, and the new measured frequency $\boldsymbol{\omega}_a$ becomes:

$$\boldsymbol{\omega}_a = \frac{e}{m_\mu}\left[a_\mu \mathbf{B} - \left(a_\mu - \frac{1}{\gamma^2 - 1}\right)\mathbf{v}\times\mathbf{E} - a_\mu \frac{\gamma}{\gamma+1}\left(\mathbf{v}\cdot\mathbf{B}\right)\mathbf{v}\right]. \tag{1.10}$$

This equation is commonly known as the Bargmann–Michel–Telegdi (BMT) equation.

One can choose to store the muons with a specific Lorentz boost γ_m, commonly known as *the magic* γ. It corresponds to a *magic energy* of $E_m = \gamma_m m_\mu \simeq 3.098$ GeV and is specifically defined such that the second term in Eq. 1.10 equals zero:

$$a_\mu - \frac{1}{\gamma_m^2 - 1} = 0. \tag{1.11}$$

Moreover, this high energy increases the lifetime of the muons by the Lorentz factor γ_m up to about 64 μs.

Muons are unstable particles that decay into electrons $\mu^+ \to e^+ + \nu_e + \bar{\nu}_\mu$ and $\mu^- \to e^- + \bar{\nu}_e + \nu_\mu$. For positive muons, the differential decay rate in the muon rest frame is:

$$\mathrm{d}N(E_e) = N(E_e)\left(1 + \frac{1-2x_e}{3-2x_e}\cos(\vartheta)\right)\mathrm{d}\Omega, \tag{1.12}$$

where E_e is the positron energy, $N(E_e)$ is the number of positrons with such energy, x_e is E_e in units of $m_\mu/2$ and ϑ is the angle between the positron momentum and the muon spin direction. By considering $\vartheta = |\boldsymbol{\omega}_a|t + \varphi$, one finds the number of decayed muons into positrons with energy greater than a threshold $\bar{E}$ at a time t:

$$N(t) = N_0(\bar{E})\exp\left\{-\frac{t}{\gamma\tau_\mu}\right\}\left[1 - A(\bar{E})\sin\left(|\boldsymbol{\omega}_a|t + \varphi\right)\right], \tag{1.13}$$

where the factor $A(\bar{E})$, named *asymmetry factor*, is the coefficient of $\cos(\vartheta)$ in Eq. 1.12 at energy $E > \bar{E}$ and τ_μ is the muon lifetime in its rest frame. The data that comes from Run-3a of E989 and its final fit is shown in Fig. 1.1.

1.2.2 Past, present, and future a_μ experiments

Before describing how the theoretical calculations of the possible contributions to the muon anomalous magnetic moment are performed, a short review of all the experimental results that come from past and present muon $g-2$ experiments is shown. Then, a brief overview of the main ideas that are behind future a_μ measurements will be given. As a matter of fact, as is more thoroughly detailed in Sec. 1.4, there is an apparent discrepancy between the SM prediction of a_μ and the experimental results. However, the theoretical prediction seems to have internal inconsistencies, leading to an unclear theoretical value of the muon anomaly. These internal puzzles need to be carefully studied for a correct interpretation of the experimental data. In a parallel effort, on the experimental side, a quest to higher-precision measurements of a_μ is crucial.

In table 1.1 a summary of the experimental values of the muon $g-2$ is shown. The first $g-2$ experiments were performed at Conseil Européen

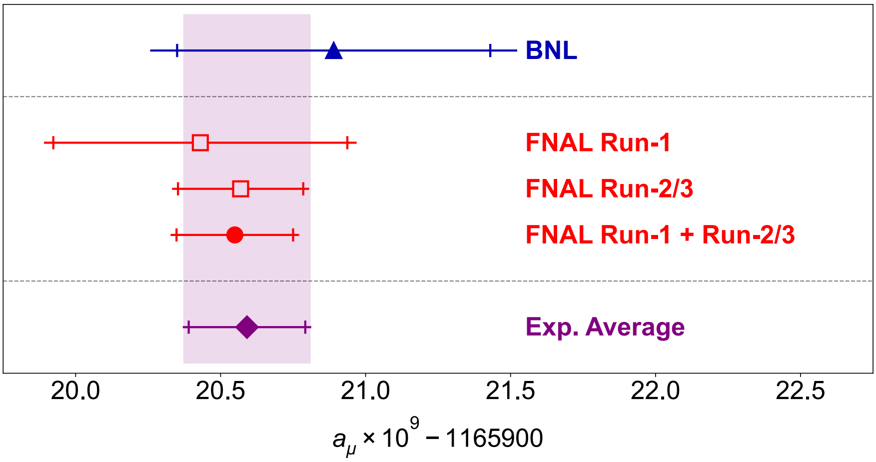

Figure 1.2: In blue, the BNL experimental determination of a_μ [7]. The red squares are the Run-1 [8] and Run-2/3 [6] results from E989 taken singularly, whereas the red circle is their combination. In purple, the average between BNL and the combination of all the FNAL runs [6].

pour la Recherche Nucléaire (CERN) in the 1960s and 1970s [9, 10, 17]. Later, in 1984, the E821 experiment started at BNL and gave definitive results in 2001 [7]. More recently, the muon anomalous magnetic moment has been measured by the Fermilab Muon $g-2$ experiment (E989), using a very similar setup to E821 and reaching an impressive precision of 0.20 parts per million (ppm) [6, 8]. The Muon $g-2$ experiment is expected to release the analysis of the remaining data that comes from runs 4, 5 and 6. The statistical precision is expected to increase by a further factor of two [6]. At the end of the full data analysis, E989 is expected to improve the total experimental error from BNL's 0.54 ppm to about 0.14 ppm, by having a much more precise control on the experimental systematics as well as by reaching a far higher statistics [18, 19], as well as an improvement on BNL's muon Electrical Dipole Moment (EDM) measurement.

In addition to the future analysis of the FNAL data, another experiment is expected to take place and perform an independent measurement of the muon anomaly. The Muon $g-2$/EDM experiment is planned to take place at Japan Proton Accelerator Research Complex (J-PARC) and it plans to measure both a_μ and the EDM [20–22]. The J-PARC experiment will be

Experiment	Year	Polarity	$a_\mu \times 10^{11}$	Precision (ppm)	Reference
CERN I	1961	μ^+	114500000(2200000)	4300	[9]
CERN II	1962/1968	μ^+	116616000(31000)	270	[10]
CERN III	1974/1976	μ^+	116591000(1100)	10	[11]
CERN III	1975/1976	μ^-	116593600(1200)	10	[11]
BNL	1997	μ^+	116592510(1500)	13	[12]
BNL	1998	μ^+	116591910(590)	5	[13]
BNL	1999	μ^+	116592020(150)	1.3	[14]
BNL	2000	μ^+	116592040(90)	0.73	[15]
BNL	2001	μ^-	116592140(90)	0.72	[16]
BNL	Average	$\mu^\pm$	116592080(63)	0.54	[7]
FNAL	2021	μ^+	116592061(41)	0.35	[8]
FNAL	2023	μ^+	116592055(24)	0.20	[6]
FNAL+BNL	Average	$\mu^\pm$	116592059(22)	0.19	[6]

Table 1.1: Summary of the a_μ measurements.

very different from all the other muon $g-2$ experiments. It plans to use ultra-cold muons, instead of ultra-relativistic muons, as in all previous cases. A beam of protons will scatter onto a graphite target, producing a muon beam. The muons are slowed down and then re-accelerated into a storage ring to about 300 MeV such that they can reach a higher polarisation and a lower transverse momentum spread. Since no electric fields are used to focus the muon beam, the precession equation that needs to be used for the final fit is Eq. 1.9. The experimental data will be fitted using the same reasoning explained in Sec. 1.2.1. The precision goal for the J-PARC is of about 0.4 ppm. This experiment will be of utmost importance to independently cross-check the BNL and FNAL measurements of a_μ.

1.3 Standard Model predictions of a_μ

In the previous section, the main experimental features that characterise the most recent a_μ experiments were discussed. In this section, a summary of the main theoretical contributions to the muon anomaly will be shown. A very complete description of all the contributing terms is detailed in [23]. The most recent collection of all the known contributions can be found in [24].

The framework that will be considered is the SM: it is a renormalisable

k	c_k	$a_\mu^{(k)} \times 10^{11}$
1	0.5	116140973.321(23)
2	0.765857420(13)	413217.6258(70)
3	24.05050984(23)	30141.90233(33)
4	130.8782(60)	381.004(17)
5	751.00(87)	5.0783(59)
6	~ 5400	~ 0.1
a_μ^{QED}		116584718.931(104)

Table 1.2: QED contributions to the muon $g-2$. The error in the final value of a_μ^{QED} mostly comes from the estimate of the sixth-order QED contributions. The detail on the error of the total value of a_μ^{QED} can be found in [24].

and relativistic Quantum Field Theory (QFT) that describes the interaction between particles. It is based on a $\text{SU}(2)_\text{L} \otimes \text{U}(1)_\text{Y} \otimes \text{SU}(3)_\text{C}$ symmetry group, broken to a $\text{SU}(2)_\text{L} \otimes \text{U}(1)_\text{em} \otimes \text{SU}(3)_\text{C}$ by the Higgs mechanism. All the ultraviolet (UV) divergences are reabsorbed thanks to the renormalisability of the SM. All the infrared (IR) divergences are exactly cancelled out by higher order virtual corrections, thanks to the Kinoshita–Lee–Nauenberg (KLN) theorem.

In principle, the muon anomalous magnetic moment can have contributions that stem from the three sectors of the SM: the EM sector, the electroweak (EW) sector and the hadronic sector, namely:

$$a_\mu^{\text{SM}} = a_\mu^{\text{QED}} + a_\mu^{\text{EW}} + a_\mu^{\text{had}}. \tag{1.14}$$

Each of the terms in Eq. 1.14 will be investigated in the following sections.

1.3.1 QED contributions

The by far largest contribution to the muon anomalous magnetic moment is due to QED effects. It can be treated perturbatively, *i.e.* a Taylor expansion in the fine structure constant α can be performed, namely the expansion parameter is sufficiently small:

$$a_\mu^{\mathrm{QED}} = \sum_{k=1}^{\infty} a_\mu^{(k)} = \sum_{k=1}^{\infty} c_k \left(\frac{\alpha}{\pi}\right)^k . \tag{1.15}$$

For instance, as briefly shown in Eq. 1.6, the one-loop correction to a_e gives $\alpha/2\pi$.

In general, the expansion depends on the masses of the leptons that are involved: there are terms that depend on a single mass and others that depend on the mass of two leptons. In the latter case, the ratio of the masses is considered:

$$a_\mu^{\mathrm{QED}} = \xi_1 + \xi_2 \left(\frac{m_\ell}{m_\mu}\right) + \xi_3 \left(\frac{m_e}{m_\mu}, \frac{m_\tau}{m_\mu}\right) . \tag{1.16}$$

The term ξ_1 represents all the contributions with purely photonic corrections and with closed lepton loops where the internal lepton is the same as the one on the external leg (*universal contributions*). The term ξ_2 accounts for diagrams with a single-lepton loop that has a different flavour w.r.t. the external one. They include the *heavy-in-light* contributions, with a τ lepton in the loop, and the *light-in-heavy* contributions, with a e in the virtual loop. These terms must be at least two-loop contributions. The last term in Eq. 1.16 includes contributions with both a light and a heavy virtual lepton circulating in a virtual loop: it is at least a three-loop contribution.

Each ξ_i in Eq. 1.16 can be expanded as a power of α:

$$\begin{aligned} \xi_1 &= \sum_{i=1}^{\infty} \xi_1^{(2i)} \left(\frac{\alpha}{\pi}\right)^i \\ \xi_2 &= \sum_{i=1}^{\infty} \xi_2^{(2i+2)} \left(\frac{\alpha}{\pi}\right)^{i+1} \\ \xi_3 &= \sum_{i=1}^{\infty} \xi_3^{(2i+4)} \left(\frac{\alpha}{\pi}\right)^{i+2} \end{aligned} \tag{1.17}$$

The coefficients c_k of order k that figure in Eq. 1.15, then, must be of the form:

$$c_k \equiv c_k(\xi_1, \xi_2, \xi_3) = \xi_1^{(2k)} + \xi_2^{(3k)} \left(\frac{m_\ell}{m_\mu}\right) + \xi_3^{(4k)} \left(\frac{m_e}{m_\mu}, \frac{m_\tau}{m_\mu}\right) . \tag{1.18}$$

Contribution	Value$\times 10^{11}$
$a_\mu^{(1)}$	194.79(1)
$a_\mu^{(2),b}$	−19.96(1)
$a_\mu^{(2),f}$	−21.27(71)
$a_\mu^{\geq 3}$	0.00(20)
a_μ^{EW}	153.6(1.0)

Table 1.3: EW contributions to the muon $g-2$. The values have been taken from Ref. [24].

Throughout the years, contributions up to five loops have been calculated and the impact of the six-loop terms has been estimated. The mass-independent terms have been calculated in [4, 25–36]. The mass-dependent terms have been calculated in [37–50]. All the cross-checks and details about the specific contributions can be found in [24] and in the references therein.

The numerical values of c_k, up to $k = 6$ are summarised in Tab. 1.2. They were obtained using the value of the fine structure constant α:

$$\alpha^{-1} = 137.035999046(27),$$

obtained with a Caesium interferometry experiment [51].

1.3.2 Electroweak corrections

In this section, the set of EW corrections that contribute to the muon anomaly will be briefly described. They weigh significantly less than the QED corrections. Therefore, their impact could not be seen until the jump in precision that came with the BNL experiment. This is mainly due to the large mass of the W, Z and Higgs bosons compared to the muon mass, $m_\mu^2/m_W^2 \sim 10^{-6}$. Moreover, all the EW corrections are higher-order contributions.

In general, they can be written in the following form:

$$a_\mu^{\text{EW}} = a_\mu^{(1)} + a_\mu^{(2),b} + a_\mu^{(2),f} + a_\mu^{\geq 3}, \tag{1.19}$$

where the first term accounts for the EW one-loop contributions. The second term describes the two-loop contributions involving a W, Z or

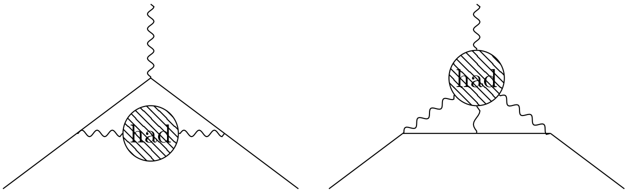

Figure 1.3: The HLO diagram (left) and the HLbL diagram (right).

Higgs boson. The third term includes all the two-loop contributions with a fermionic loop and the last term accounts for all the contributions beyond the two-loop level.

The numerical values of each of the contributions that appear in Eq. 1.19 are summarised in Tab. 1.3 [52, 53]. Precise details on the calculations can be found in [23, 24, 54].

1.3.3 Hadronic corrections

In this section, the terms that contribute to the theoretical prediction of the muon $g-2$ within the strong sector of the SM will be investigated. These are the terms that include quarks, gluons and hadrons. Unlike the two previous sets of contributions, *i.e.* the QED one and the EW one, the hadronic contributions cannot be calculated in a perturbative way. This is due to the fact that the coupling constant of Quantum Chromodynamics (QCD), α_{s}, at low energies is not a small parameter. Thus, it is not a good expansion parameter for the theory.

The hadronic contributions a_μ^{had} can be split into three separate parts:

$$a_\mu^{\mathrm{had}} = a_\mu^{\mathrm{HLO}} + a_\mu^{\mathrm{HOVP}} + a_\mu^{\mathrm{HLbL}}. \tag{1.20}$$

The first term indicates the Hadronic Leading Order (HLO) contributions, the second one takes into account the Higher-Order Vacuum Polarisation (HOVP) terms and the third one includes the Hadronic Light-by-Light (HLbL) effects. All the three terms will be described in the following section.

$a_\mu^{\text{HLO}} \times 10^{11}$	Reference
6871(30)	[57]
6940(40)	[58]
6881(41)	[23]
6928(24)	[59]

Table 1.4: Full calculations of a_μ^{HLO}.

1.3.3.1 Data-driven and dispersive approach

One possible way to compute hadronic corrections makes use of experimental data and Dispersion Relation (DR). In this section, a brief review of all the hadronic contributions that have been calculated, as well as their numerical impact will be shown.

The HLO contributions are the most sizeable between all the hadronic effects in Eq. 1.20. In addition to this, they constitute the most important source of theoretical error between all the contributions to the muon anomalous magnetic moment. They are a $\mathcal{O}(\alpha^2)$ order contribution and they consist of a Hadronic Vacuum Polarisation (HVP) insertion on top of the one-loop vertex correction, as shown in the left diagram in Fig. 1.3. Such effects can be calculated using DR techniques together with $e^+e^- \to$ hadrons experimental data, as in the following equation [55, 56]:

$$a_\mu^{\text{HLO}} = \frac{\alpha^2}{3\pi^2} \int_{m_\pi^2}^{\infty} \frac{\mathrm{d}s}{s} R(s) K(s). \tag{1.21}$$

In the last equation, the lower bound of the integral is the rest mass of the neutral pion, which is the lowest-mass hadronic state. The factors $K(s)$ and $R(s)$ are respectively the kernel function of the DR and the $e^+e^- \to$ hadrons annihilation cross section divided by the $e^+e^- \to \mu^+\mu^-$ cross section, which is called the R ratio.

Above a certain threshold energy value, Perturbative Quantum Chromodynamics (pQCD) can be used together with experimental data. This threshold energy corresponds to center of mass (CM) energies of about $\sqrt{s} \gtrsim 11$ GeV, at the $b\bar{b}$ threshold.

Thus, the calculation of the HLO contribution is performed through the convolution of the analytical kernel function with data coming from

$a_\mu^{\text{HVP, NLO}} \times 10^{11}$	Reference
$-99.3(7)$	[23]
$-98.4(7)$	[64]
$-98.7(9)$	[48]
$-98.3(4)$	[59]

Table 1.5: Evaluations of $a_\mu^{\text{HVP, NLO}}$.

e^+e^- annihilation experiments. Sec. 2.1 will be specifically devoted to how Eq. 1.21 is derived. Moreover, many details regarding the methods and the experiments used to gather the very high precision e^+e^- annihilation measurements, as well as the merging of their data. In this section, only the numerical value of a_μ^{HLO} will be given.

In table 1.4, different full evaluations of a_μ^{HLO} are shown. These values can be merged in order to have a single theoretical prediction for a_μ^{HLO} [58–63]:

$$a_\mu^{\text{HLO}} = 6931(28)(28)(7) \times 10^{-11} = 6931(40) \times 10^{-11}. \tag{1.22}$$

The first error comes from the uncertainties of the experimental data, the second error comes from the experimental systematic uncertainties and the third error is the difference of the evaluations of the HLO contribution based on experimental data and based on pQCD between 1.8 GeV and 2.0 GeV. These three errors are then combined as a quadratic sum [24].

Another possible method to evaluate a_μ^{HLO} makes use of data on semileptonic τ decays, such as $\tau^- \to \pi^-\pi^0\nu_\tau$ [65]. Such data-driven method has consistently been about 2σ away from the experimental value of a_μ [66–74]. The Isospin-Breaking (IB) corrections have been lately computed in [75–78].

The second term in Eq. 1.20 keeps into account all the higher-order insertions of a HVP. At the moment, contributions at Next-to-Leading Order (NLO) and Next-to-Next-to-Leading Order (NNLO) are known:

$$a_\mu^{\text{HOVP}} = a_\mu^{\text{HVP, NLO}} + a_\mu^{\text{HVP, NNLO}}. \tag{1.23}$$

A number of theoretical calculations of $a_\mu^{\text{HVP, NLO}}$ have been done. They are summarised in Tab. 1.5 and a merging has been performed between all

Contribution	$a_\mu^{\mathrm{HLbL}} \times 10^{11}$	Error	Reference
π^0, η, η' poles	93.8	4.0	
π, K loops & boxes	−16.4	0.2	
S-wave $\pi\pi$ rescattering	−8	1	
Scalars and tensors	−1	3	
Axial vectors	6	6	
u, d, s loops and short-distance	15	10	
c loop	3	1	
Total	92	19	[24]
Total (PdRV09)	105	26	[79]
Total (N/JN09)	116	39	[54, 80]
Total (J17)	100.4	28.2	[23]

Table 1.6: Evaluations of a_μ^{HLbL} as in [24]. Below, the same quantity in older calculations.

the calculations, giving a final result of [24]:

$$a_\mu^{\mathrm{HVP,\,NLO}} = -98.3(7) \times 10^{-11}. \tag{1.24}$$

At NNLO, in Ref. [48] the term $a_\mu^{\mathrm{HVP,\,NNLO}}$ was computed. The contribution yields:

$$a_\mu^{\mathrm{HVP,\,NNLO}} = 12.4(1) \times 10^{-11}. \tag{1.25}$$

The last relevant term that figures in Eq. 1.20 consists of HLbL contributions. This term is the second-largest source of uncertainty on the total prediction of a_μ. HLbL contributions are $\mathcal{O}(\alpha^3)$ corrections: this implies that a relative theoretical error of about 10% will be sufficient to match the FNAL expected experimental precision.

Just like for a_μ^{HLO}, the HLbL contribuof discrepancies between the Standard Model theoretical prediction, thetions cannot be treated perturbatively, since the particles that take part in the hadronic loop may have a very small energy and pQCD cannot therefore be used. Many earlier calculations were based on hadronic models that work in the non-perturbative regime. A brief review of those calculations is summarised in [24] and in all the references therein.

Collaboration	$a_\mu^{\mathrm{HLO}} \times 10^{11}$	Reference
ETM-18/19	6921(163)	[83,84]
FHM-19	6990(150)	[85]
BMW-17	7111(75)(175)	[86]
HPQCD-16	6670(60)(120)	[87]
ETM-13 ‡	6740(210)(180)	[88]
Mainz/CLS-19	7200(124)(99)	[89]
PACS-19	$7370(90)(^{+13}_{-18})$	[90]
RBC/UKQCD-18	7174(163)(92)	[91]
Mainz-17 ‡	$6540(320)(^{+21}_{-23})$	[92]
BMW-20	7075(55)	[93]
LM-20	7140(270)(130)	[94]

Table 1.7: Summary of calculations of a_μ^{HLO} using lattice QCD techniques. Not all calculations include all the possible effects: the results that figure with a double-dagger (‡) do not include Strong Isospin Breaking (SIB) or QED corrections. When two errors are present, the first one is statistical and the second one is systematic. Wherever there is only one error bar, the combination of the statistical and systematic uncertainties is intended. The two results after the black horizontal line are not included in the WP final prediction of a_μ^{HLO} [24].

More recently, a dispersive approach was proposed to perform the same calculation [24,81]. The calculation of HLbL contributions using a dispersive method is way more complicated than the HLO case. For the HLO calculation, a single cut in the hadronic blob can be performed for all the intermediate states. This implies, as will be explained in section 2.1, that the HLO contribution to a_μ can be explicitly written as an integral of the $\sigma(e^+e^- \to \text{hadrons})$ cross section. On the other hand, HLbL contributions are more complicated because it is possible to cut the hadronic blob in different ways, causing the dispersion relation to change with the choice of the intermediate states. The original proposals can be found in [81,82]. Details on the calculations can be found in the White Paper (WP) and in the references therein [24]. The latest accepted numerical estimate can be seen in Tab. 1.6 and are compared to the older HLbL calculations that do not use the dispersive approach.

The HLbL contributions at NLO have also been addressed in [95] and they yield:

$$a_\mu^{\mathrm{HLbL,\,NLO}} = 2(1) \times 10^{-11}. \tag{1.26}$$

The HLbL contribution precision goal of 10% is yet to be reached. However, work in this direction is ongoing [24, 96].

1.3.3.2 Lattice QCD approach

Another possible way to compute hadronic corrections makes use of lattice QCD. All the details on the lattice QCD computations of a_μ^{HLO} will be described in Sec. 2.2. In this section, only the numerical results are shown, to complete the overview on the a_μ theory-experiment comparison.

In Tab. 1.7 and in Fig. 1.4, a complete list of all the available evaluations of a_μ^{HLO} is shown. All the results that are included in the WP have been combined in a lattice HLO average:

$$a_\mu^{\mathrm{HLO}} = 7116(184) \times 10^{-11}, \tag{1.27}$$

with an uncertainty of 2.6%. The first result that has a below-percent uncertainty level is the BMW-20 one [93], that is shown in Tab. 1.7. This result alone has an about 2σ tension with the experimental result and with the data-driven HLO calculation. No newer calculations of the full a_μ^{HLO} are available, yet. However, multiple calculations on an intermediate time window have been performed by many collaborations, as will be shown in Sec. 2.2.

Lattice QCD can be used to compute also the more involved HLbL contributions to the muon anomaly, in an independent fashion w.r.t. the dispersive or data-driven approaches described in the previous section. The first complete calculation was performed by the RBC/UKQCD collaboration in [97], after cross-checks with the Mainz collaboration for heavier pion masses [98]. In this calculation, the QED term is computed on a finite volume and then extrapolated to the infinite limit. The result reads:

$$a_\mu^{\mathrm{HLbL}} = 78.7(30.6)(17.7) \times 10^{-11} \tag{1.28}$$

where the first error is the statistical one, and the second is the systematic one.

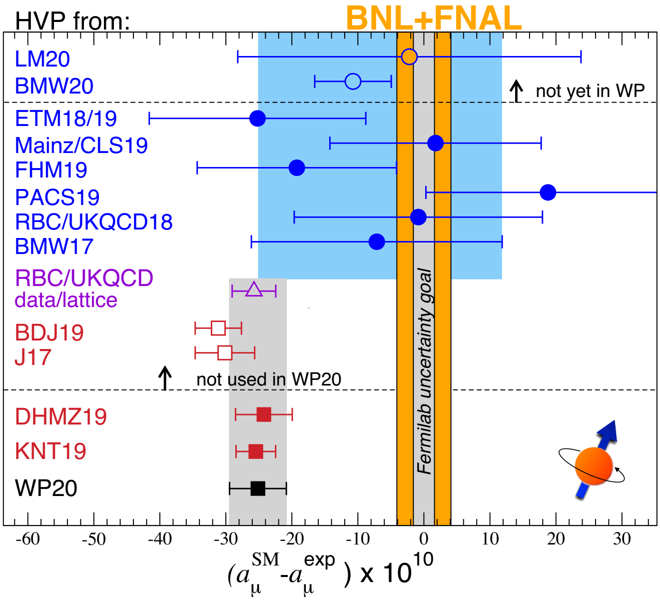

Figure 1.4: Comparison between theoretical predictions of a_μ with the experimental data coming from [7,8], in the orange band. The blue circles refer to the values of Tab. 1.7, summed to all the other SM contributions. BMW-20 and LM-20 are not included in the WP. Red squares are the dispersive results of Tab. 1.4, coming from [58,59]. The black square is the WP result [24]. The purple triangle result comes from [91]. The figure comes from [96].

An alternative complete calculation was performed by the Mainz collaboration, using an infinite-volume method (QED_∞) in Ref. [99]:

$$a_\mu^{\mathrm{HLbL}} = 106.8(14.7) \times 10^{-11}. \tag{1.29}$$

This alternative method was proposed in [100] and then further developed in [101–103]. It is expected that, with both approaches, the uncertainty will decrease under the target 10% by 2025 [96].

Contribution	Value $\times 10^{11}$	Error $\times 10^{11}$	Section
a_μ^{QED}	116584718.931	0.104	1.3.1
a_μ^{EW}	153.6	1.0	1.3.2
a_μ^{HLO}	6931	40	1.3.3
a_μ^{HOVP}	-85.9	7	1.3.3
a_μ^{HLbL}	92	18	1.3.3
a_μ^{SM}	116591810	43	
a_μ^{exp}	116592059	22	1.2.2
$\lvert a_\mu^{\mathrm{exp}} - a_\mu^{\mathrm{SM}} \rvert$	249	48	

Table 1.8: Summary of all the contributions to a_μ^{SM} as in the WP [24] and of the most precise experimental determination of a_μ from the E821 [7] and E989 [6] experiments.

1.4 Status of data-theory comparison

The theoretical contributions that were presented in the previous sections can be all summed to give a final theoretical prediction to the muon $g-2$. By inserting all the numerical values that were presented in the previous sections into Eq. 1.14, one gets a final value for the muon anomalous magnetic moment a_μ^{SM}:

$$a_\mu^{\mathrm{SM}} = a_\mu^{\mathrm{QED}} + a_\mu^{\mathrm{EW}} + a_\mu^{\mathrm{had}} = 116591810(43) \times 10^{-11}. \tag{1.30}$$

The details on the single contributions are summarised in Tab. 1.8. The numbers presented are the most recent and accepted values for a_μ and come from a joint effort of all the theory community for the muon anomalous magnetic moment, called the Theory Initiative (TI). This effort resulted in the publication of a WP, in 2020 [24]. All the numbers in Tab. 1.8 come from the aforementioned WP.

As can be clearly seen from Tab. 1.8 and in Fig. 1.5, there is a clear discrepancy between the theoretical prediction of a_μ in the WP and the most precise experimental measurement of the same quantity, at the level of 5σ. However, the BMW-20 calculation of the HLO contribution a_μ^{HLO} shows a tension from the WP prediction, which is based on e^+e^- annihilation data. Moreover, a new measurement of the $e^+e^- \to \pi^+\pi^-$ cross section from

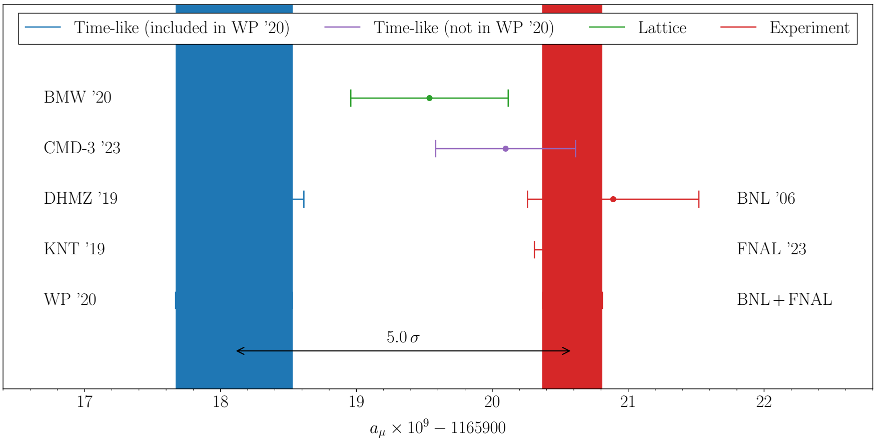

Figure 1.5: In blue, the WP theoretical prediction as of 2020 [24] and the results from [59] and [58]. In red, from top to bottom there are the BNL experimental result [7], the latest FNAL experimental result [6] and their average. In orange, the BMW-20 calculation from [93]. In purple, the theoretical prediction of a_μ if only the CMD-3 data for the $\pi^+\pi^-$ channel are used to calculate a_μ^{HLO} [104, 105]. In green, the BMW lattice QCD result [93]. The plot was taken from [106].

the CMD-3 experiment seems to give a different result w.r.t. older data [104,105]. By inserting only the CMD-3 result into the theoretical prediction for $a_\mu^{\mathrm{HLO},\pi\pi}$ the discrepancy between the SM theoretical prediction of a_μ and the FNAL+BNL experimental result is reduced to about 0.9σ [105]. Many more details and a more coherent context on the new CMD-3 measurement will be given in Sec. 2.1, as well as a thorough description of the e^+e^- annihilation experiments that enter in the DR that is used to compute a_μ^{HLO} and figures in the WP.

The current scenario sees the lattice QCD calculations of a_μ^{HLO} giving different results from the data-driven approach calculations. Moreover, the latter makes use of data that comes from different collaborations and $e^+e^- \to$ hadrons experiments. These experiments seem not to give compatible results, as will be more clearly stated in Sec. 2.1.

As shown in Tab. 1.8, the biggest contribution to the total error of the theoretical prediction of a_μ^{SM} is due to hadronic effects. More specifically, it is known that the HLO contribution is the crucial term that needs to be investigated in order to clearly understand the nature of the discrepancy on the muon $g-2$. With the analysis of the final E989 runs, an important theoretical effort is needed to decrease the error on a_μ^{HLO}. In the next chapter, the most important theoretical ways to do so are detailed.

Chapter 2

THEORETICAL APPROACHES TO a_μ^{HLO}

In Chapter 1, the lepton anomalous magnetic moment was defined. Then, the muon anomalous magnetic moment a_μ was introduced. The main experimental efforts that were made to measure this quantity have been listed. Moreover, the idea behind such experiments was addressed. Later, the SM contributions to the total value of the muon anomaly a_μ have been briefly described. The aforementioned measurements and the theoretical prediction of a_μ have been then compared: there is an evident discrepancy between the SM prediction in which DRs have been employed to calculate a_μ^{HLO} and the most recent and precise measurements. It is well understood that the most dominant contribution to the error of the muon

$g-2$ comes from the HLO term which now becomes the main interest of study. The standard method to compute a_μ^{HLO} requires the use of DRs. However, the current status of the theoretical predictions is complicated by an alternative calculation of a_μ^{HLO} that makes use of lattice QCD: this result has an about 2σ tension with the dispersive calculation. Moreover, very recently, a new measurement of the $e^+e^- \to \pi^+\pi^-$ cross section, performed by the CMD-3 collaboration, looks like it significantly differs from previous measurements of the same quantity.

In this chapter, details on three ways to compute a_μ^{HLO} are given. In section 2.1, the dispersive approach is described. In section 2.2, the lattice QCD approach to compute the HLO term is detailed. In section 2.3, a recent approach to compute the same quantity is introduced: it is based on the use of experimental data in the *spacelike* region, namely it uses data of a scattering process where the transferred momentum squared is negative ($q^2 < 0$).

2.1 Timelike approach to a_μ^{HLO}

The main difficulty that is encountered when calculating the hadronic contributions to a_μ comes from the impossibility of performing a Taylor expansion in the strong coupling constant α_s in the low-energy regime and using a perturbative approach. The calculation of loop integrals with the insertion of HVP in photon propagators can be performed using dispersive integrals. In this section, details on the use of this technique to calculate a_μ^{HLO} will be given.

2.1.1 The theoretical framework

The first ingredient that is introduced to calculate HVP effects is the photon self-energy $\Pi_\gamma'^{\text{had}}$ at one-loop, which can also be referred as *hadronic blob*: this term takes into account HVP corrections to the photon propagator at Leading Order (LO). It is a One-Point-Irreducible (1PI) function, meaning that it cannot be split into two disconnected diagrams by cutting a single internal propagator.

One can exploit causality and the analyticity of the photon self-energy function to write a DR. Since the EM current correlator has logarithmic UV singularities, the DR will be written in the form of a Subtracted Dispersion Relation (SDR):

$$\Pi_\gamma^{\prime\,\mathrm{had}}(q^2) - \Pi_\gamma^{\prime\,\mathrm{had}}(0) = \frac{q^2}{\pi}\int_0^\infty \mathrm{d}s \frac{\mathrm{Im}\,\Pi_\gamma^{\prime\,\mathrm{had}}(s)}{s(s-q^2-i\varepsilon)}. \tag{2.1}$$

The DR that is needed to write the HLO contribution to the muon anomalous magnetic moment follows [107, 108]:

$$a_\mu^{\mathrm{HLO}} = \frac{\alpha}{\pi}\int_0^\infty \mathrm{d}s \frac{K(s)}{s}\,\mathrm{Im}\,\Pi_\gamma^{\prime\,\mathrm{had}}(s), \tag{2.2}$$

for timelike squared transferred momenta, namely $s = q^2 > 0$. In Eq. 2.2, $K(s)$ is the kernel function. It is defined as:

$$K(s) = \int_0^1 \mathrm{d}x \frac{x^2(1-x)}{x^2 + s(1-x)/m_\mu^2}. \tag{2.3}$$

The unitarity of the $\mathcal{S}$ matrix implies the validity of the optical theorem, which states that the imaginary part of the HVP contribution is proportional to the total cross section of the e^+e^- annihilation process into hadrons. In this respect, one can write:

$$\sigma(e^+e^- \to \mathrm{hadrons}) = \frac{4\pi\alpha(\mathrm{s})}{\mathrm{s}}\,\mathrm{Im}\,\Pi_\gamma^{\prime\,\mathrm{had}}(\mathrm{s}), \tag{2.4}$$

which is valid in the *timelike* region, *i.e.* for positive exchanged momentum $q^2 > 0$.

Then, one can introduce the hadronic ratio $R(s)$ as:

$$R(s) = \frac{\sigma(e^+e^- \to \mathrm{hadrons})}{\sigma(e^+e^- \to \mu^+\mu^-)}. \tag{2.5}$$

Eq. 2.2, then, becomes [55, 56]:

$$a_\mu^{\mathrm{HLO}} = \frac{\alpha^2}{3\pi^2}\int_{m_{\pi_0}^2}^\infty \frac{\mathrm{d}s}{s} R(s)K(s), \tag{2.6}$$

where the lower limit of the dispersive integral is the square of the neutral pion mass, π_0, since the lowest-mass hadronic state that can be produced is $\pi_0\gamma$.

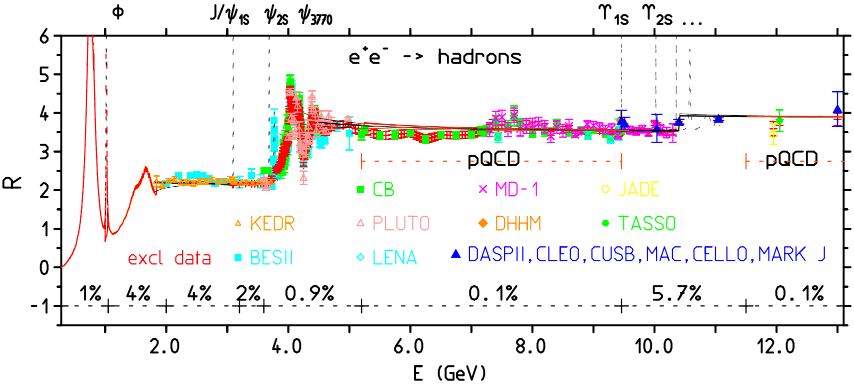

Figure 2.1: The R ratio $R(s)$ and the $e^+e^- \to$ hadrons data. At the bottom the systematic errors are shown for different energy regions [24].

Eq. 2.6 can be separated into two energy domains:

$$a_\mu^{\mathrm{HLO}} = \frac{\alpha^2}{3\pi^2}\left[\int_{m_{\pi_0}^2}^{\varepsilon^2} \frac{\mathrm{d}s}{s} R_{\mathrm{data}}(s)K(s) + \int_{\varepsilon^2}^{\infty} \frac{\mathrm{d}s}{s} R_{\mathrm{pQCD}}(s)K(s)\right], \qquad (2.7)$$

where ε is an energy threshold below which a perturbative approach can no longer be used. Above this threshold, summing all the final-state (FS) exclusive channels is not possible because many measurements do not range up to these high energies. Moreover, at such high energies, many high-multiplicity final states would need to be taken into account. For these reasons, for energies above about $\sqrt{s} \gtrsim 11$ GeV, pQCD seems to be a good method to compute $R(s)$. However, for CM energies between about 2 GeV and 11 GeV, there is not a consensus on the use of inclusive data or pQCD [24]. It is crucial to keep in mind that in Eq. 2.6 the integrand goes like $\sim K(s)/s$, namely the most important contributions to a_μ^{HLO} correspond to small s processes. In Fig. 2.1, one can see the plot of the R ratio $R(s)$ as a function of the CM energy.

2.1.2 The hadronic data

At low energies the total hadronic cross section needs to be calculated performing a summation of all the possible hadronic final states. The most important channel is the $\pi\pi$ channel, accounting for about 70% of a_μ^{HLO}. Sub-leading contributions consist of the $\pi\pi\pi$ channel, the KK channel and the $\pi\pi\pi\pi$ channel. Higher-multiplicity of final states have become relevant to give the most accurate description of the hadronic production cross section. To give a final value of a_μ^{HLO}, the experimental data need to be properly combined and analysed. Not all data sets span the whole energy range, or come with equally fine binning. On top of this, there might even be correlations between different sets. For this reason, the most cautious approach to analyse them would be to firstly combine the data sets, and in a second step to integrate them, to give the $g - 2$ prediction.

There are two main experimental approaches that can be used to gather the needed $e^+e^- \to$ hadrons data for the a_μ^{HLO} contribution at low energies: the scan method and the Initial State Radiation (ISR) approach.

The scan method makes use of e^+e^- data that is taken at fixed CM energy. Different CM energies are then explored in order to get many data points within the full energy range that is required. To give a precise determination of the cross section, the integrated e^+e^- luminosity needs to be calculated using known QED cross sections ($e^+e^- \to e^+e^-$, $\mu^+\mu^-$, $\gamma\gamma$). The main advantages of this method are the fact that the CM energy is known very precisely and that the energy resolution is very good. This makes it possible to study narrow resonances, like the ω and the ϕ. However, since data points can be taken only at discrete CM energy values, an interpolation procedure between those data points needs to be performed. Moreover, at low energies the luminosity decreases, making the calculation of the cross sections more difficult. All these considerations imply that many experiments that operate at specific energies, run by different collaborations need to span the full energy range. The scan method was used by CMD-2 for the $\pi^+\pi^-$ channel [109–111], for the KK final states [112, 113] and for multi-hadronic channels [111, 114–117]. Moreover, SND detectors at Novosibirsk measured the $\pi^+\pi^-$ channel [118], the $\pi^0\gamma$ final state [119,120], the KK final states [121–123], the $n\bar{n}$ final state [124] and multi-hadronic channels [125–129]. More recently, the CMD-3 collaboration measured the $\pi^+\pi^-$ final state [104,105], the KK final states [130], the $p\bar{p}$ final state [131] and multi-hadronic channels [132–135]. Inclusive measurements have been performed at BES-II [136–138] and KEDR [139, 140]. A full compilation of data sources and experiments is present in Refs. [23, 24, 141].

The ISR approach makes use of processes where a hard photon is emitted, keeping a fixed CM energy $\sqrt{s}$. If the ISR photon has an energy fraction of $x = 2E_\gamma/\sqrt{s}$, the e^+e^- annihilation has an energy of $\sqrt{s'} = \sqrt{(1-x)s}$, and the cross section for $e^+e^- \to$ hadrons can be derived from the $e^+e^- \to \gamma_{\mathrm{ISR}} +$ hadrons:

$$\frac{\mathrm{d}N_{\mathrm{ISR}}}{\mathrm{d}\sqrt{s'}} = \frac{\mathrm{d}\mathcal{L}_{\mathrm{ISR}}}{\mathrm{d}\sqrt{s'}} \varepsilon_{\mathrm{X}\gamma}(\sqrt{s'}) \sigma^0_{\mathrm{X}(\gamma)}(\sqrt{s'}). \tag{2.8}$$

In the previous equation, on the left-hand side (l.h.s.) there is the number of events of the $e^+e^- \to \gamma_{\mathrm{ISR}} +$ hadrons process, whereas $\mathrm{d}\mathcal{L}_{\mathrm{ISR}}/\,\mathrm{d}\sqrt{s'}$ is the effective ISR luminosity, $\varepsilon_{\mathrm{X}\gamma}(\sqrt{s'})$ is the acceptance and $\sigma^0_{\mathrm{X}(\gamma)}(\sqrt{s'})$ is the cross section for $e^+e^- \to$ hadrons, also including possible Final State Radiation (FSR) effects. The ISR approach was used by the KLOE collaboration at DAΦNE for the $\pi^+\pi^-$ channel [142–145] and by the BABAR experiment for the $\pi^+\pi^-$ channel [146–148], for the K^+K^- channel [146, 147], for multi-hadronic channels [149–159] and for $p\bar{p}$ channel [160, 161]. Recently, also BESIII [162] and CLEO-c [163] obtained results using this method. The main advantage of the ISR method is the fact that the cross section is measured over a continuous energy range that goes from the lower-bound threshold and arrives close to the $\sqrt{s}$ of the experiment. In the KLOE experiment, the CM energy is 1.02 GeV. The BABAR experiment has a higher value of $\sqrt{s} = 10.58$ GeV: this limits the accessible statistics of the signal. The main disadvantage of the ISR approach is related to the number of possible background processes and radiative corrections to the ISR process.

This underlines the extreme importance of having a very accurate Monte Carlo (MC) code for simulating the radiative corrections and the luminosity processes. At the moment, the most used MC generators for the e^+e^- luminosity are MCGPJ [164], BHWIDE [165], KKMC [166] and BABAYAGA [167]. The MC generator that is used to compute the annihilation processes into hadrons is PHOKHARA [168, 169].

2.1.2.1 Tensions between data sets

Since the hadronic data comes from different experiments and collaborations, it is possible that not all data sets are perfectly statistically

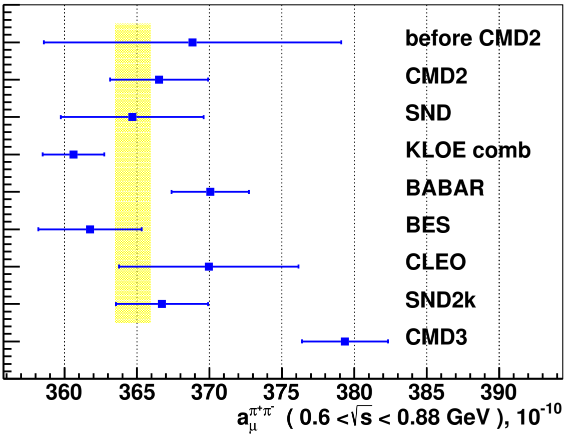

Figure 2.2: The $e^+e^- \to \pi^+\pi^-(\gamma)$ contribution to a_μ^{HLO} between $0.6\,\mathrm{GeV} < \sqrt{s} < 0.88\,\mathrm{GeV}$, coming from the CMD-3 data and compared to the results of other previous experiments [104].

compatible, given the very high precision that is required. Such incompatibilities alter the precision of the combined cross section that is used to compute a_μ^{HLO}.

The most important tensions that need to be addressed are in the $e^+e^- \to \pi^+\pi^-$ channel, since this channel accounts for more than 70% of the HLO contribution to the muon $g-2$. In this respect, the KLOE, the BABAR and the CMD-3 experiments do not agree within their uncertainties. This can clearly be observed in Fig. 2.2: the CMD-3 result is clearly higher than the results of all the other e^+e^- experiments, that rely either on the energy scan or on the ISR approach. It is also very interesting to look at the measurements of the pion form factor $|F_\pi|^2$, for $0.327\,\mathrm{GeV} < \sqrt{s} < 1.2\,\mathrm{GeV}$ and to compare the results of the different collaborations. This comparison is shown in Fig. 2.3, taken from [105]. The yellow band represents the systematic error of the CMD-3 experiment. In the middle plot, the CMD-3 fit is compared to the ISR experiments, whereas in the bottom plot it is compared to the energy scan experiments. The disagreements seem to be localised between $0.5\,\mathrm{GeV} < \sqrt{s} < 0.85\,\mathrm{GeV}$:

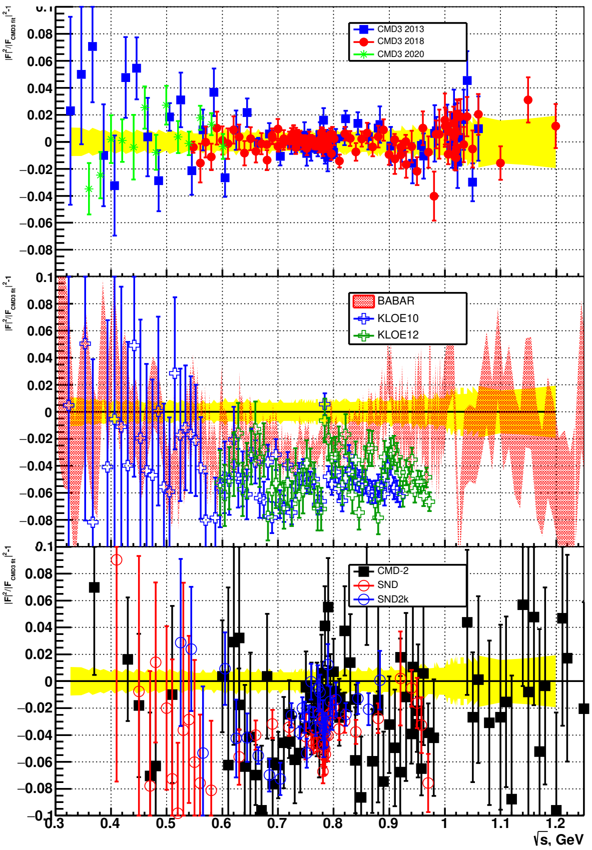

Figure 2.3: The three plots show the relative differences between the pion form factor and the fit of CMD-3 results. In the top plot, the fit is compared with the CMD-3 experimental data. In the middle plot the fit is compared with the most precise ISR measurements (BABAR, KLOE10 and KLOE12). In the bottom plot, the fit is compared with the most precise energy scan experiments (CMD-2, SND and SND2k) [105].

the largest discrepancy is between CMD-3 and the KLOE measurements, at the level of about 5%, as can be seen in the central plot of Fig. 2.3, whereas the discrepancy between CMD-3 and the other experiments is at the level of about 2 to 3%. The most important difference is observed at the l.h.s.

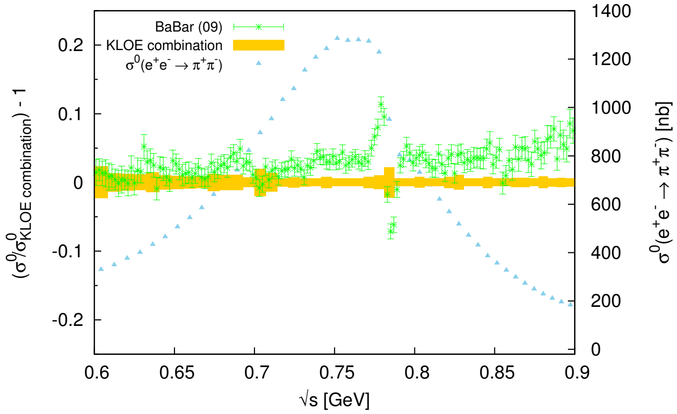

Figure 2.4: The combined KLOE $e^+e^- \to \pi^+\pi^-$ cross section compared to the BABAR data points between $0.6\,\mathrm{GeV} < \sqrt{s} < 0.9\,\mathrm{GeV}$. The KLOE result is represented by the yellow band and the uncertainties are the combination of both statistical and systematic errors in quadrature [170].

of the ρ meson peak, namely at about $0.6\,\mathrm{GeV} \lesssim \sqrt{s} \lesssim 0.75\,\mathrm{GeV}$ [105].

Also the determinations of $a_\mu^{\mathrm{HLO}}[\pi\pi]$ coming from the BABAR and KLOE experiments do not agree well within their uncertainties. Around the $\rho - \omega$ interference region, the BABAR measurement of the $e^+e^- \to \pi^+\pi^-$ cross section is higher than the one performed by the KLOE collaboration, as can be seen in Fig. 2.4 [170]. The determination of $a_\mu^{\mathrm{HLO}}[\pi\pi]$ by SND, BESIII and CMD-2 are statistically compatible with either the KLOE or the BABAR data [24].

Some tensions were present also in the KK channel at the level of about 20% between BABAR [160] and SND [122], but are resolved by the latest SND result [123].

2.1.3 Data merging

In order to get a single value of a_μ^{HLO} it is crucial to properly combine all the $e^+e^- \to$ hadrons experimental data in a consistent way. Therefore, a merging procedure needs to be performed. This is required not only to provide a correct prediction of the central value of a_μ^{HLO}, but also to keep into account the uncertainty propagation that comes from many experimental data sets and many different collaborations and experiments. In general, the biggest issues come from the interpolation of different data sets into a single form of the function $R(s)$ that enters the DR for the HLO contribution. Moreover, the inclusion of pQCD prediction in certain energy intervals is not uniquely defined or straightforward. Different analysis groups provided their method to compute a_μ^{HLO}, as shown in Tab. 1.4.

The Davier–Hoecker–Malaescu–Zhang (DHMZ) approach [58, 60, 70] is based on a second-order polynomial combination of data coming from the same experiment, instead of a trapezoidal, *i.e.* linear, combination. After combining each data set, an averaging procedure is employed, keeping into account the correlations between measurements and experiments, and the different densities of data or different bin widths. Moreover, the uncertainty on each contribution is estimated by generating a pseudo-data set for the given experiment. pQCD is used above 1.8 GeV, except for around the charmonium region, where inclusive data is used in the dispersive integral.

The Keshavarzi–Nomura–Teubner (KNT) approach [59, 61] is based on the compilation of the hadronic data with a clustering technique. This procedure determines the best binning in a algorithmic way: the algorithm scans all the possible bin widths and then fits the data. The optimal bin width is determined by the global and local fit quality and the final uncertainties on the contributions to a_μ^{HLO}. A too wide binning would lose important information on the behaviour of the $R(s)$ function. A too narrow binning would place too few data points in each bin, thus leading to no advantage in the procedure. The fit is performed using an iterative χ^2 procedure that includes all the covariance matrices and thus all the possible correlations. pQCD is used for energies above the $b\bar{b}$ threshold, *i.e.* $\sqrt{s} > 11.199$ GeV.

2.2 Lattice determination of a_μ^{HLO}

In Sec. 1.3.3.2, the results of the calculation of a_μ^{had} using lattice QCD were shown. Then, in Sec. 1.4 they were compared to the dispersive results that make use of the timelike approach (as in Sec. 2.1) to compute a_μ^{HLO} and to the experimental measurements of a_μ. In this Section, a lattice QCD-based approach to calculate the HLO contribution to the muon anomaly will be shown.

2.2.1 Theoretical framework

Any lattice QCD calculation of the HLO contribution to a_μ starts from the EM current correlator:

$$C_{\mu\nu}(\mathsf{x}) = \left\langle j_\mu^{\mathrm{em}}(\mathsf{x}), j_\nu^{\mathrm{em}}(0)\right\rangle, \tag{2.9}$$

where the EM current $j_\mu^{\mathrm{em}}(\mathsf{x})$ is defined as:

$$j_\mu^{\mathrm{em}}(\mathsf{x}) = \sum_{i=1}^{N_f} Q_i \bar{\psi}_i(\mathsf{x})\gamma_\mu \psi_i(\mathsf{x}). \tag{2.10}$$

The index i labels the quark flavours, N_f is the number the flavours and Q_i is the quark charge, in units of the elementary electric charge. The Vacuum Polarisation (VP) tensor is introduced by Fourier transforming the correlator:

$$\Pi_{\mu\nu}(\mathsf{q}) = \int \mathrm{d}^4\mathsf{x} e^{i\mathsf{q}\cdot\mathsf{x}} C_{\mu\nu}(\mathsf{x}). \tag{2.11}$$

The HLO contribution can be determined by convolving the VP tensor with an appropriate kernel function:

$$a_\mu^{\mathrm{HLO}} = \left(\frac{\alpha}{\pi}\right)^2 \int_0^\infty \mathrm{d}q^2 f(q^2)\hat{\Pi}(q^2), \tag{2.12}$$

where the UV-finite VP tensor was introduced:

$$\hat{\Pi}(q^2) = 4\pi^2 \left[\Pi(0) - \Pi(q^2)\right] \tag{2.13}$$

and the kernel function is defined as:

$$f(q^2) = \frac{m_\mu^2 q^2 Z^3(1 - q^2 Z)}{1 + m_\mu^2 q^2 Z^2}, \qquad Z = -\frac{q^2 - \sqrt{q^4 + 4m_\mu^2 q^2}}{2m_\mu^2 q^2}, \tag{2.14}$$

for spacelike momenta $q^2 < 0$ [171–173].

A key point of any lattice QCD calculation lies in the choice of the most appropriate VP function $\hat{\Pi}(q^2)$. One possible choice is known as the *hybrid* *method* [174]: the q^2 range can be divided into three parts, by introducing two cuts q_1^2 and q_2^2, such that $q_1^2 < q_2^2$. Then, Eq. 2.12 can be rewritten as:

$$
\begin{aligned}
a_\mu^{\mathrm{HLO}} = \left(\frac{\alpha}{\pi}\right)^2 \Bigg[& \int_0^{q_1^2} \mathrm{d}q^2 f(q^2)\hat{\Pi}(q^2) \\
& + \int_{q_1^2}^{q_2^2} \mathrm{d}q^2 f(q^2)\hat{\Pi}(q^2) \\
& + \int_{q_2^2}^{\infty} \mathrm{d}q^2 f(q^2)\hat{\Pi}_{\mathrm{pert}}(q^2) \Bigg].
\end{aligned} \tag{2.15}
$$

In the third integral, perturbation theory is used to compute $\hat{\Pi}(q^2)$. In the second region, lattice results are very accurate and the integral can be performed using numerical techniques. The contribution below q_1^2 is the most important one. Therefore, a reliable description of $\hat{\Pi}(q^2)$ is crucial. One possible solution that has been proposed is to use Padé approximants to model the VP in this regime [174,175]. Another possibility is to perform a change of variables using conformal polynomials [174].

Another possible method to compute a_μ^{HLO} is known as the *time moments* method. It is used as a way to compute the VP effects at small q^2 [176]. By considering the four-momentum q with only the time component, namely $\mathsf{q} = (\omega, 0, 0, 0)$, one can write the VP function in terms of the Fourier transform of the current correlator:

$$\omega^2 \Pi(\omega^2) = \int \mathrm{d}^4\mathsf{x} e^{i\mathsf{q}\cdot\mathsf{x}} C_{jj}(\mathsf{x}), \tag{2.16}$$

where the index j is only spatial. One can average over the three spatial directions and use that $\mathsf{q}\cdot\mathsf{x} = \omega\bar{x}$. Eq. 2.16 becomes:

$$\omega^2 \Pi(\omega^2) = -\int \mathrm{d}\bar{x} e^{i\omega\bar{x}} C(\bar{x}), \tag{2.17}$$

where

$$C(\bar{x}) = -\frac{1}{3}\sum_{j=1}^{3}\int \mathrm{d}^3\mathbf{x} C_{jj}(\mathbf{x}). \tag{2.18}$$

The time moments are given by:

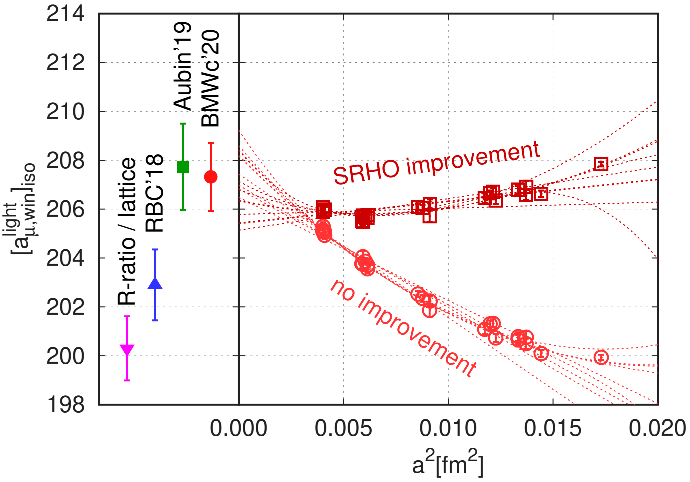

Figure 2.5: The plot shows the continuum extrapolation of the IS contributions to $a_\mu^{\mathrm{HLO}}(ud)$ on the window, as defined in Eq. 2.28. Two ways to perform this extrapolation are shown, one without any improvement on the data and one with corrections from a model that includes the ρ meson (SRHO). On the left panel, the result is compared with the results of other lattice groups: RBC/UKQCD [91], Aubin [177] and the $R(s)$-based determination [59]. The plot comes from [93].

$$G_{2n} = \int_{-\infty}^{\infty} \mathrm{d}\bar{x}\bar{x}^{2n} C(\bar{x}). \tag{2.19}$$

The VP function then can be written as:

$$\Pi(q^2) = -\frac{1}{2} G_2 + \sum_{n=1}^{\infty} \frac{(-1)^{n+1}}{(2n+2)!} G_{2n+2} (q^2)^n. \tag{2.20}$$

An alternative possible way to write the UV-finite subtracted VP function was determined in Ref. [178]:

$$\hat{\Pi}(q^2) = 4\pi^2 \int_0^{\infty} \mathrm{d}\bar{x} C(\bar{x}) \left[\bar{x}^2 - \frac{4}{q^2} \sin^2\left(\frac{q\bar{x}}{2}\right)\right]. \tag{2.21}$$

Eq. 2.12 then becomes:

$$a_\mu^{\mathrm{HLO}} = \left(\frac{\alpha}{\pi}\right)^2 \int_0^{\infty} \mathrm{d}\bar{x} C(\bar{x}) \tilde{f}(\bar{x}), \tag{2.22}$$

where

$$\tilde{f}(\bar{x}) = 8\pi^2 \int_0^\infty \frac{\mathrm{d}\omega}{\omega} f(\omega^2) \left[\omega^2 \bar{x}^2 - 4\sin^2\left(\frac{\omega\bar{x}}{2}\right)\right]. \tag{2.23}$$

2.2.2 Contributions and uncertainties

At the order $\mathcal{O}(\alpha^2)$, one can separate the full HLO contribution into two parts:

$$a_\mu^{\mathrm{HLO}}(\alpha^2) = a_{\mu,\,\mathrm{c}}^{\mathrm{HLO}} + a_{\mu,\,\mathrm{d}}^{\mathrm{HLO}}, \tag{2.24}$$

where the c subscript indicates the quark-connected contractions, whereas the d subscript stands for the quark-disconnected ones. In general, one can calculate all the connected contractions that come from the quarks separately, namely:

$$a_{\mu,\,\mathrm{c}}^{\mathrm{HLO}} = a_\mu^{\mathrm{HLO}}(ud) + a_\mu^{\mathrm{HLO}}(s) + a_\mu^{\mathrm{HLO}}(c) + a_\mu^{\mathrm{HLO}}(b). \tag{2.25}$$

In the previous equation on the right-hand side (r.h.s.), the contractions of up and down, strange, charm and bottom quarks are intended, respectively. No contributions coming from the electric charge of valence and sea quarks are included in Eq. 2.24, nor the effects due to the up-down mass difference (isosymmetric limit).

If one also considers the SIB and the Electromagnetic Isospin Breaking (QED IB) contributions, it is possible to write:

$$a_\mu^{\mathrm{HLO}} = a_\mu^{\mathrm{HLO}}(\alpha^2) + \delta a_\mu^{\mathrm{HLO}}, \tag{2.26}$$

where

$$\delta a_\mu^{\mathrm{HLO}} = \delta a_\mu^{\mathrm{HLO}}(ud) + \delta a_\mu^{\mathrm{HLO}}(s) + \delta a_\mu^{\mathrm{HLO}}(c) + \delta a_{\mu,\,\mathrm{d}}^{\mathrm{HLO}}. \tag{2.27}$$

In $\delta a_\mu^{\mathrm{HLO}}(ud)$ QED IB and SIB corrections are present. In $\delta a_\mu^{\mathrm{HLO}}(s)$ and in $\delta a_\mu^{\mathrm{HLO}}(c)$, only QED IB effects are included. It is crucial to understand that the most important contribution comes from the connected contribution of light quarks $a_\mu^{\mathrm{HLO}}(ud)$. This term accounts for about 90% of the whole $a_\mu^{\mathrm{HLO}}(\alpha^2)$. Contributions from connected strange and charm quarks, namely $a_\mu^{\mathrm{HLO}}(s)$ and $a_\mu^{\mathrm{HLO}}(c)$ respectively account for about 8% and 2% of the total value of $a_\mu^{\mathrm{HLO}}(\alpha^2)$.

All the lattice QCD calculations are performed on a discretised space-time: therefore, the Phase Space (PhSp) integrals are substituted by sums over finite lattice volumes. To recover the continuum limit, one needs to perform a limit for infinite lattice volumes $V \to \infty$ as well as a limit for small lattice spacings $a \to 0$. This procedure is called *continuum extrapolation*. An example of how lattice data points are modified in the continuum extrapolation limit can be seen in Fig. 2.5, relative to the calculation of the Isospin-Symmetric (IsSy) contributions to $a_\mu^{\mathrm{HLO}}(ud)$ on the intermediate window.

This limit is based on different simulations that are run at different values of the lattice spacings and then a fit is performed, combining also Chiral Perturbation Theory (ChPT) interpolations around the IsSy point. ChPT introduces some error but, at the moment, they are acceptably small, *i.e.* at the level of few percent. However, in the future, in order to reach a sub-percent precision, all the lattice calculations should not be based on the ChPT fit functions, but only on the ensembles at the IsSy physical point [24].

2.2.3 Windows

The calculation of the whole HLO term using lattice QCD is limited in precision by the continuum extrapolation. It is possible to split Eq. 2.22 into three parts, that divide the whole time range into three different time regions. This is done to separately study the short-distance or the long-distance systematic effects. In this respect, the *window method* was proposed by RBC/UKQCD [91]. This method breaks the time integral into three separate contributions:

$$\begin{aligned}
a_\mu^{\mathrm{HLO}} &= a_\mu^{\mathrm{SD}} + a_\mu^{\mathrm{W}} + a_\mu^{\mathrm{LD}} \\
&= \left(\frac{\alpha}{\pi}\right)^2 \left[\int_0^\infty \mathrm{d}\bar{x} C(\bar{x}) \tilde{f}(\bar{x}) [1 - \Theta(\bar{x}, t_0, \Delta)] \right. \\
&\qquad + \int_0^\infty \mathrm{d}\bar{x} C(\bar{x}) \tilde{f}(\bar{x}) [\Theta(\bar{x}, t_0, \Delta) - \Theta(\bar{x}, t_1, \Delta)] \\
&\qquad \left. + \int_0^\infty \mathrm{d}\bar{x} C(\bar{x}) \tilde{f}(\bar{x}) \Theta(\bar{x}, t_1, \Delta) \right],
\end{aligned} \tag{2.28}$$

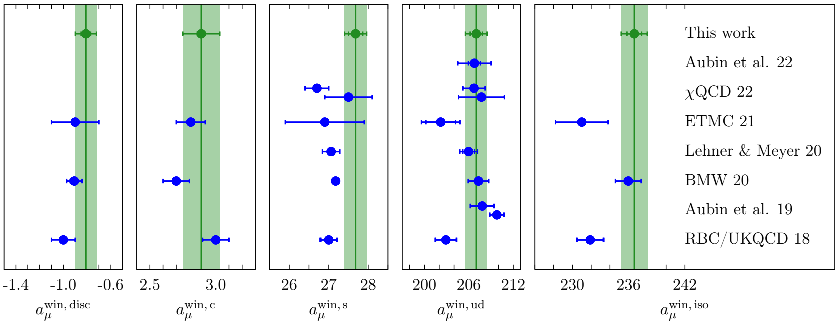

Figure 2.6: Comparison of lattice results for specific quark contributions to a_μ^{HLO} in the intermediate window and at the IS point. From left to right, the quark-disconnected, the charm, the strange and the up-down contributions are shown. In the last panel, the total value for a_μ^{W} is shown. From top to bottom, the results come from [179], [180], [181], [182], [94], [93], [177] and [91]. Consider that more recent results have been published by the RBC/UKQCD and ETMC collaborations, as shown in Fig. 2.7. The plot comes from [179].

where the smoothing function is defined as

$$\Theta(t, t', \Delta) = \frac{1 + \tanh[(t - t')/\Delta]}{2}. \tag{2.29}$$

The parameter Δ indicates the width of the window, whereas the two parameters t_0 and t_1 separate the short-distance and the long-distance effects. The intermediate window is less sensitive to the error that comes from the discrete lattice. This implies that the calculation of the muon anomaly on the window can be a good way to determine if the different lattice methods give statistically compatible results. Moreover, given the high precision that is needed for the calculation of a_μ^{HLO}, careful studies of the systematic effects that derive from the spacetime discretisation are crucial.

A lot of effort is currently devoted to the determination of the quantity a_μ^{W}. Recent results have been published by the RBC/UKQCD collaboration [91, 184], by the ETMC collaboration [182, 183], by the CLS collaboration [179] and by the BMW collaboration [93]. The CLS and RBC/UKQCD

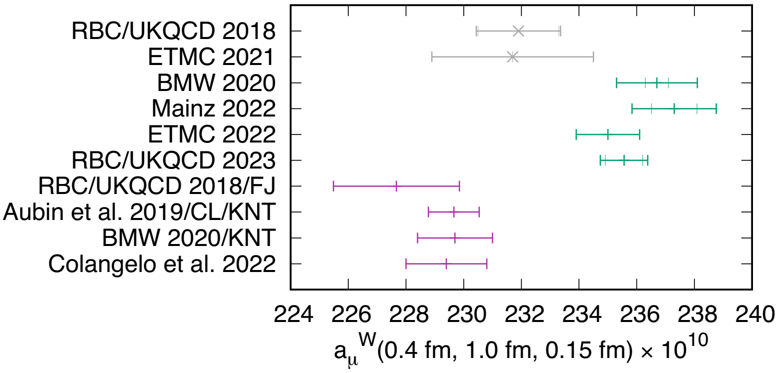

Figure 2.7: Comparison of the $a_\mu^{\rm W}$ contribution. The grey points are the older lattice QCD calculations. From top to bottom, they come from [91]and [182]. The green points are the most recent lattice QCD calculations. From top to bottom, they come from [93], [179], [183] and [184]. The green points are the dispersive results, on the window. From top to bottom, they come from [91], [61, 177], [59, 93] and [185]. The plot comes from [184].

results lie about 3.8σ above the most recent evaluation of the window contribution using the data-driven method [185]. In Fig. 2.6, a list of lattice results for various quark sub-contributions in the intermediate window is shown. A list of results of the complete window observable $a_\mu^{\rm W}$ coming from the different collaborations is shown in Fig. 2.7. The most recent results seem to agree with each other within the errors.

2.3 Spacelike approach to $a_\mu^{\rm HLO}$

In the two previous sections, two independent methods to compute the HLO contribution to the muon anomalous moment were presented. Moreover, as shown in Sec. 1.4, they seem to give two discrepant predictions of $a_\mu^{\rm HLO}$, the lattice QCD result being closer to the experimental measurement performed by BNL and FNAL. In recent years, a novel approach has been presented to calculate the HLO contribution. It uses data coming from a process in the *spacelike* region, namely a process where the transfer of the total four-momentum squared is negative. The determination of $a_\mu^{\rm HLO}$ derives from the measurement of the running of the fine structure constant

α [186].

The starting point is Eq. 2.2 [107, 108]:

$$a_\mu^{\mathrm{HLO}} = \frac{\alpha}{\pi} \int_0^\infty \mathrm{d}s \frac{K(s)}{s} \operatorname{Im} \Pi_\gamma'^{\,\mathrm{had}}(s), \tag{2.30}$$

where the kernel function is given in Eq. 2.3:

$$K(s) = \int_0^1 \mathrm{d}x \frac{x^2(1-x)}{x^2 + s(1-x)/m_\mu^2}. \tag{2.31}$$

By exchanging the order of the integration between s and x, one obtains [171]:

$$\begin{aligned} a_\mu^{\mathrm{HLO}} &= \frac{\alpha}{\pi} \int_0^1 \mathrm{d}x(1-x) \int_0^\infty \mathrm{d}s \frac{1}{s} \frac{\operatorname{Im} \Pi_\gamma'^{\,\mathrm{had}}(s)}{\pi} \frac{x^2}{x^2 + s(1-x)/m_\mu^2} \\ &= \frac{\alpha}{\pi} \int_0^1 \mathrm{d}x(x-1) \int_0^\infty \mathrm{d}s \frac{1}{s} \frac{\operatorname{Im} \Pi_\gamma'^{\,\mathrm{had}}(s)}{\pi} \frac{t(x)}{s - t(x)}, \end{aligned} \tag{2.32}$$

where $t(x) < 0$ is the squared transferred four-momentum:

$$t(x) = \frac{x^2 m_\mu^2}{x-1} < 0. \tag{2.33}$$

If one considers $t(x) = q^2$, the second integral in the last member of Eq. 2.32 becomes equal to the r.h.s. of Eq. 2.1. By combining the two results, one obtains:

$$a_\mu^{\mathrm{HLO}} = \frac{\alpha}{\pi} \int_0^1 \mathrm{d}x(x-1) \left\{ \Pi_\gamma'^{\,\mathrm{had}}\left[t(x)\right] - \Pi_\gamma'^{\,\mathrm{had}}(0) \right\}. \tag{2.34}$$

By considering that

$$\Delta\alpha_{\mathrm{had}}[t(x)] = -\operatorname{Re}\left\{ \Pi_\gamma'^{\,\mathrm{had}}\left[t(x)\right] - \Pi_\gamma'^{\,\mathrm{had}}(0) \right\} \tag{2.35}$$

and $\operatorname{Im} \hat{\Pi}(q^2) = 0$ for negative q^2, Eq. 2.34 becomes:

$$a_\mu^{\mathrm{HLO}} = \frac{\alpha}{\pi} \int_0^1 \mathrm{d}x(1-x) \Delta\alpha_{\mathrm{had}}[t(x)]. \tag{2.36}$$

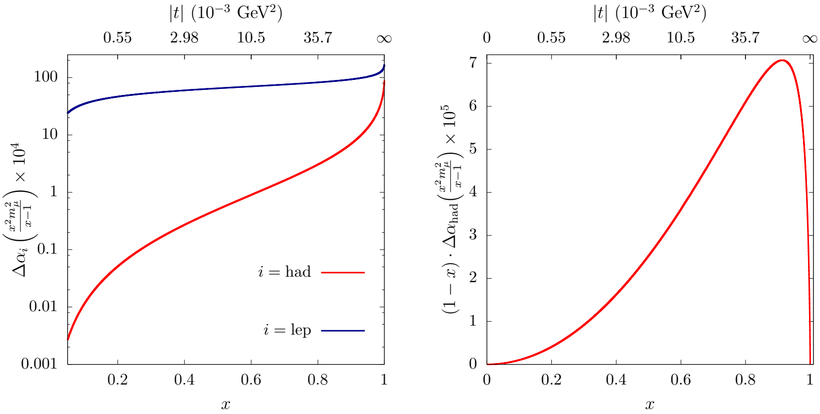

Figure 2.8: On the l.h.s. a comparison between $\Delta\alpha_{\rm had}[t(x)]$ in red and $\Delta\alpha_{\rm lep}[t(x)]$ in blue. On the r.h.s. the smooth integrand of Eq. 2.36. The plots come from [187].

Eq. 2.36 is the master equation for determining the HLO contribution to the muon anomalous magnetic moment, in the spacelike region. In principle, one can measure the effective EM coupling in the spacelike region and then insert it in this equation to give a theoretical prediction for $a_\mu^{\rm HLO}$. By changing the kernel function in Eq. 2.36, it is also possible to calculate the higher-order terms $a_\mu^{\rm HOVP}$ [188].

The total running of the fine structure constant depends on the leptonic contributions and on the hadronic contributions. The former can be calculated order-by-order in perturbation theory. It is known up to the three loop accuracy in QED [189] and at four loops [190]. One can write the running of α as follows:

$$\alpha(t) = \frac{\alpha(0)}{1-\Delta\alpha(t)} = \frac{\alpha(0)}{1-\Delta\alpha_{\rm had}(t)-\Delta\alpha_{\rm lep}(t)}. \tag{2.37}$$

By inverting this relation and solving for $\Delta\alpha_{\rm had}(t)$, one gets:

$$\Delta\alpha_{\rm had}(t) = 1 - \frac{\alpha(0)}{\alpha(t)} - \Delta\alpha_{\rm lep}(t), \tag{2.38}$$

where the leptonic contribution to the running of α can be computed and the total running of α can be measured in the spacelike region.

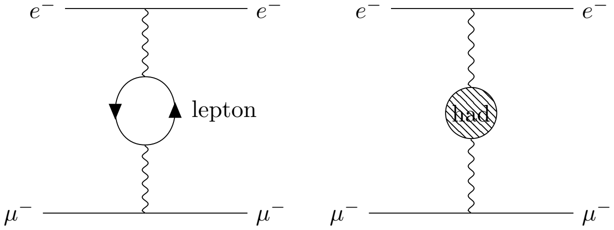

Figure 2.9: The Vacuum Polarisation diagrams that contribute to the leptonic (left) and hadronic (right) running of the EM coupling constant α.

In Fig. 2.8 one can see the contributions of the leptonic and hadronic running of the fine structure constant as a function of the Feynman variable $x \in [0, 1]$ or the momentum transfer $|t| \in [0, \infty)$. The integrand has its maximum value at $x_{\text{max}} \simeq 0.914$, or $t_{\text{max}} \simeq -0.108$ GeV^2 and $\Delta\alpha_{\text{had}}(t_{\text{max}}) \simeq 7.86 \times 10^{-4}$ [186, 187]. The main advantage of the spacelike approach is that the integrand function is smooth, as can be seen in the right panel of Fig. 2.8. On the other hand, as shown in Section 2.1, the timelike $R(s)$ ratio relies on the timelike $e^+e^- \to$ hadrons experimental data in the low energy region, making the integrand function much more fluctuating due to the uncertainty of the experiments and the narrow resonances. Moreover, the running of α can be measured in principle by a single experiment in the spacelike region. This implies that the combination of the experimental data would not require any complicated merging between different data sets, a crucial procedure that is needed with the timelike approach.

The most suitable processes to measure $\Delta\alpha_{\text{had}}(t)$ are Bhabha scattering ($e^+e^- \to e^+e^-$) and muon-electron scattering ($e^-\mu^\pm \to e^-\mu^\pm$). The former can be a s-channel or a t-channel process at tree level, whereas the latter is a pure t-channel process. This makes μe scattering the optimal process to investigate the hadronic running of α [187].

It is estimated that a precision of about 10^{-5} on $\Delta\alpha_{\text{had}}(t)$ is needed to compete with the latest dispersive and lattice results. Since the LO contribution to the μe scattering cross section is quadratic in the coupling constant $\alpha(t)$, one can estimate the required precision on the cross section [186]:

$$\frac{1}{2}\frac{\delta\sigma}{\sigma} \simeq \frac{\delta\alpha}{\alpha} \simeq \delta\Delta\alpha_{\rm had}. \tag{2.39}$$

Therefore, an experimental accuracy of 10^{-5} on the differential cross section is required. This is a very challenging goal that requires a dedicated experimental effort.

In this respect, the MUonE experiment was proposed to measure the muon-electron scattering cross section at the level of 10 ppm on the differential observables, to determine the HLO contribution to the muon $g-2$ in the spacelike region. A description of the experiment will be given in Sec. 3.1.

Chapter 3

The MUonE experiment

In Chapter 2, the main theoretical approaches to calculate the HLO contribution to the muon anomalous magnetic moment were discussed. In Sec. 2.3, a novel approach to calculate a_μ^{HLO} was described. This method exploits the measurement of the running of the EM coupling constant α in the *spacelike* region, namely with negative transferred squared momenta $q^2 < 0$, to determine the HLO contribution. In order to do so, a very promising process that has been identified is muon-electron scattering, which is a purely t-channel process. The measurement of the total running of the coupling constant $\alpha(t)$ and the calculation of the leptonic contribution to the running $\Delta\alpha_{\mathrm{lep}}(t)$ allow for a determination of the hadronic contribution to the running $\Delta\alpha_{\mathrm{had}}(t)$. This quantity enters the DR that is exploited to calculate a_μ^{HLO}, as shown in Eq. 2.36. In this respect, the MUonE experiment has been proposed at CERN to precisely measure the

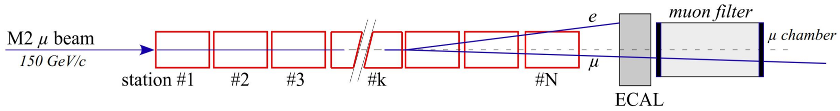

Figure 3.1: A scheme of the MUonE experimental setup [191].

running of the fine structure constant $\alpha(t)$.

In Sec. 3.1, the MUonE experiment will be described. Moreover, the extraction of $\Delta\alpha_{\text{had}}(t)$ from the experimental data and the MC simulations, and the expected statistical accuracy and systematics will be briefly discussed in Sections 3.2 and 3.3, respectively.

3.1 The MUonE experiment at CERN

MUonE is an experiment that was proposed to measure the cross section of μe elastic scattering. From this measurement, the hadronic running of the EM coupling constant $\Delta\alpha_{\text{had}}(t)$ can be extracted and used to give a prediction of a_μ^{HLO}. A muon beam with energy of about $E_\mu = 160$ GeV and an average rate of about 1.3×10^7 muons per second is scattered on a fixed target. The M2 muon beam at CERN North Area has been identified as the perfect candidate for the MUonE experiment [191]. The fixed target of the experiment will be made of beryllium, which is a low Z material which minimises possible background effects, as will be shown in Chapter 5, as well as multiple Coulomb scattering (MCS) effects.

The experimental setup consists of a sequence of 40 stations each of which has a 15 mm thick beryllium target and tracking sensors which are used to measure the scattering angles of the FS particles with high precision, as shown in Fig. 3.1. The main advantage of having a series of stations is that the muon beam can be re-used, allowing for a higher number of μe scattering events. Moreover, the use of forty 15 mm targets instead of a single 60 cm beryllium piece greatly reduces the systematic effects of MCS. An electromagnetic calorimeter (ECAL) will be placed downstream of all the 40 stations. Its purpose is to provide the particle identification (PID) for the electrons and the muons that have an angle of about 2 mrad to 3 mrad. As a matter of fact, in this region, the muons and the electrons that undergo elastic scattering tend to have similar scattering

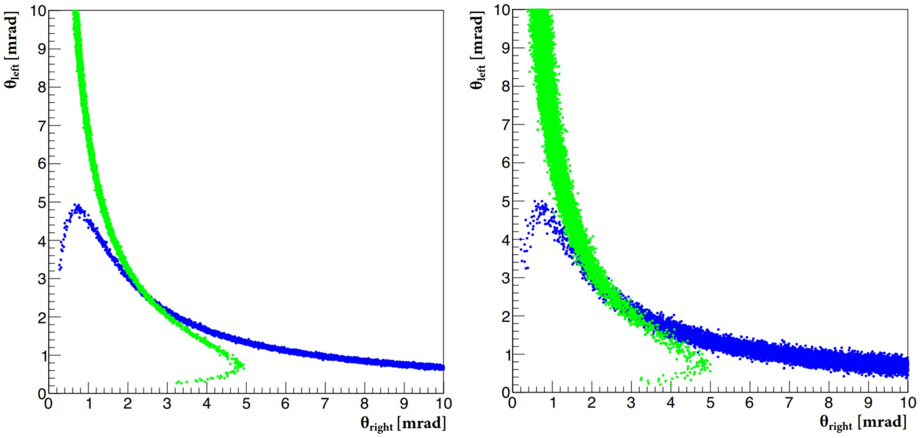

Figure 3.2: Distribution of the two measured scattering angles in mrad. In the l.h.s. plot, the events have been simulated assuming an angular resolution of 20 μrad, which is the experimental goal. In the r.h.s. plot, the events have been simulated assuming an angular resolution of 100 μrad [191].

angles, as can be seen in Fig. 3.2. Moreover, a muon filter will be placed downstream of the ECAL, in order to provide an assessment of a possible pion contamination of the muon beam.

The most important element of the experimental hardware is the tracking system. It allows for a very precise measurement of the scattering angles of the FS electron and muon, w.r.t. the direction of the incoming muon. Since the maximum scattering angle is of about 30 mrad, due to kinematical constraints, the needed area of the tracking stations is of about 10×10 cm^2, given the 1 m distance between the tracker and the beryllium target. Considering the geometry of the tracking stations and the spatial resolution of the tracker planes, which is expected to be of about 20 μm, a final angular resolution of about 20 μrad is expected.

The ECAL provides crucial information concerning the PID of the particles. In the kinematic region where $\vartheta_e \simeq \vartheta_\mu$ the sole tracking station cannot distinguish the two FS particles. An ECAL can resolve the elastic scattering kinematics by using the electron angle or electron energy measurements. Moreover, in the case of multiple EM showers, the ECAL clearly recognises the radiative events.

Many more details on the MUonE experimental setup can be found in [192–194].

3.2 Kinematics and the extraction of $\Delta\alpha_{\text{had}}(t)$

In this section, the kinematics of the MUonE experiment will be described. Moreover, the procedure that will be used to extract the hadronic running of the fine structure constant from the experimental data will be discussed.

In the muon-electron scattering process, the initial-state (IS) muon impinges on the beryllium target. The muon can hit an electron, embedded in the target at rest. The four-momenta of the particles that are involved in the process are:

$$\begin{aligned}
\mathsf{p}_1 =& (E_\mu, 0, 0, |\mathbf{p}|)\\
\mathsf{p}_2 =& (m_e, 0, 0, 0)\\
\mathsf{p}_3 =& (E_\mu^f, |\mathbf{p}_3| \sin\vartheta_\mu, 0, |\mathbf{p}_3| \cos\vartheta_\mu)\\
\mathsf{p}_4 =& (E_e, -|\mathbf{p}_4| \sin\vartheta_e, 0, |\mathbf{p}_4| \cos\vartheta_e),
\end{aligned} \tag{3.1}$$

where $E_i = \sqrt{|\mathbf{p}_i|^2 + m_i^2}$. The t Mandelstam variable is:

$$t = \|\mathsf{p}_1 - \mathsf{p}_3\|^2 = \|\mathsf{p}_2 - \mathsf{p}_4\|^2 = 2m_e^2 - 2m_e E_e, \tag{3.2}$$

and the s Mandelstam variable is:

$$s = \|\mathsf{p}_1 + \mathsf{p}_2\|^2 = \|\mathsf{p}_3 + \mathsf{p}_4\|^2 = m_e^2 + m_\mu^2 + 2m_e E_\mu, \tag{3.3}$$

where the usual Minkowski norm is intended. By defining r as

$$r \equiv \frac{\sqrt{E_\mu^2 - m_\mu^2}}{E_\mu + m_e} \tag{3.4}$$

and by imposing the energy-momentum conservation, one can calculate the FS electron energy E_e and scattering angle ϑ_e:

$$E_e = m_e \frac{1 + r^2\cos^2\vartheta_e}{1 - r^2\cos^2\vartheta_e}; \quad \vartheta_e = \arccos\left(\frac{1}{r}\sqrt{\frac{E_e - m_e}{E_e + m_e}}\right). \tag{3.5}$$

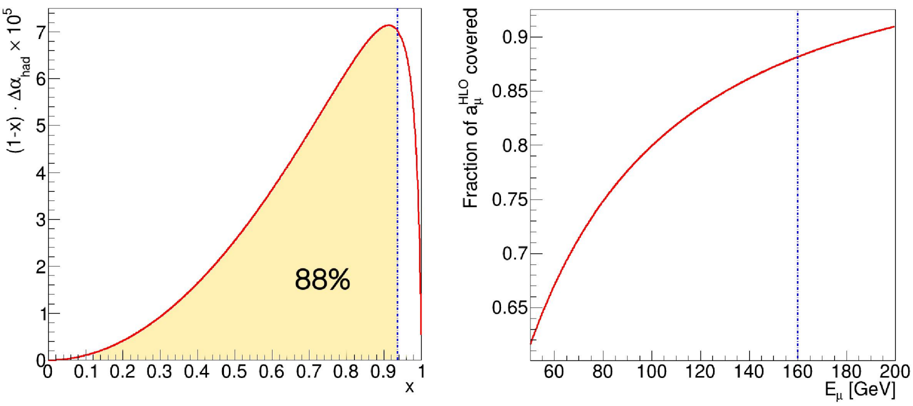

Figure 3.3: On the l.h.s., there is the integrand function in Eq. 2.36 for a IS muon energy of $E_\mu = 160$ GeV. On the r.h.s., there is the fraction of $a_\mu^{\rm HLO}$ covered as a function of the muon energy [192].

The transferred momentum t can go from a minimum value of $t_{\rm min} = -\lambda(s, m_\mu^2, m_e^2)/s$ to a maximum value of $t_{\rm max} = 0$. By inverting Eq. 2.33 for x, one can find the maximum value of x, which is $x_{\rm max} \simeq 0.936$. This implies that a 160 GeV muon beam cannot cover the whole integrand domain. As a matter of fact, it can allow to compute about 88% of the total integral that is used to calculate $a_\mu^{\rm HLO}$. This fact is shown in the r.h.s. panel in Fig. 3.3. The remaining part of the integral which corresponds to $x \in [0.936, 1]$ is not accessible, if one uses the data that come from the MUonE experiment. An extrapolation of the hadronic running can be performed, using an appropriate parametrisation for $\Delta\alpha_{\rm had}(t)$ and a MC template fit procedure. This procedure consists in the generation of multiple MC samples that have a dependence on a set of parameters which are fixed by the choice of parametrisation for $\Delta\alpha_{\rm had}(t)$.

One possible parametrisation function that has been identified imitates the QED LO contribution to the running of the fine structure constant $\alpha(t)$ for negative transferred momenta t:

$$\Delta\alpha_{\text{had}}(t) = KM\left[-\frac{5}{9} - \frac{4M}{3t} + \left(\frac{4M^2}{3t^2} + \frac{M}{3t} - \frac{1}{6}\right) \times \frac{2}{\sqrt{1-\frac{4M}{t}}} \ln\left|\frac{1-\sqrt{1-\frac{4M}{t}}}{1+\sqrt{1-\frac{4M}{t}}}\right|\right]. \tag{3.6}$$

In the previous equation, the two free parameters are K and M. The choice of this parametrisation is consistent with the fact that for large negative transferred momenta $|t|$ the hadronic running of α behaves similarly as $\ln |t|/M$.

The template fit procedure requires that a grid of points is generated in the parameter space where K and M live. Then, for each pair of generated parameters, it is possible to fit Eq. 3.6 with a calculation of $\Delta\alpha_{\text{had}}(t)$ that uses a DR in the timelike region [195]:

$$\Delta\alpha_{\text{had}}(q^2) = -\frac{\alpha q^2}{3\pi} \operatorname{Re} \int_{m_{\pi_0}^2}^{\infty} \mathrm{d}s \frac{R(s)}{s(s-q^2-i\varepsilon)}. \tag{3.7}$$

Subsequently, a MC sample is generated using a dedicated MC event generator, MESMER. The generation within MESMER can be unweighted or weighted. In the first case, each event has a constant weight in the distributions. Moreover, it has to undergo an acceptance-or-rejection procedure which reduces the generation efficiency, depending on the kinematical constraints that are imposed by the selection criteria. This means that in order to have the very high number of elastic events that is needed for the analysis, which is of about $\mathcal{O}(10^{12})$ elastic events, the number of generated events will be much higher than that, increasing the simulation runtime. This is the reason that led to the implementation of weighted generation: in order to increase the generation efficiency, weighted events can be used. In this case, each event has a specific weight attached to it which needs to be taken into account when calculating observables and generating samples for the data analysis.

In addition to the generation of weighted events, MESMER is able to replace the weights of each generated event with new ones, whenever different contributions are included in the MESMER calculation, without re-generating the whole MC sample. This procedure is called *reweighting*.

Many more details and technicalities of the MESMER MC code will be described in Appendix A.

The MC sample is generated and then reweighted to simulate different contributions to the hadronic running of the EM constant $\Delta\alpha_{\text{had}}(t)$, without changing the initial seed of the generation and thus keeping full correlation between the generated data sets. This allows for a further reduction of statistical fluctuations in the final data analysis. The very same procedure is then performed for different values of the parameters (K, M). Then, a best fit calculation between the experimental data and the generated templates is performed, for example by using a χ^2 test or a log-likelihood test. This determines the best-fit values for $K = \bar{K}$ and $M = \bar{M}$ that, when inserted in Eq. 3.6, provide the best extrapolating function outside the MUonE kinematical boundaries that gives the total value of a_μ^{HLO}.

Very recently, an alternative method to extract a_μ^{HLO} has been proposed for the MUonE experiment. It allows to extract about 99% of the total value of a_μ^{HLO} from the data that is gathered by the MUonE experiment, exploiting some mathematical properties of the kernel function $K(s)$. The remaining 1% can be computed combining pQCD with data of the timelike $e^+e^- \to$ hadrons processes [196].

3.3 Experimental precision goal and systematic uncertainties

The MUonE experiment needs to match the precision of the timelike and the lattice QCD predictions of a_μ^{HLO}, in order to give a significantly useful contribution to the muon anomalous magnetic moment puzzle. To do so, the relative statistical and systematic uncertainties on a_μ^{HLO} need to reach about 0.3%.

This level of precision can be obtained with a total running time of about 4×10^7 s, distributed in about 3 years of data taking. The total luminosity that will be reached is of about 1.5×10^7 nb^{-1}. This is equivalent to measuring the elastic muon-electron scattering differential cross section with a precision of about 10 ppm [187]. Such a high precision goal on the measurement requires a very high control on the experimental systematic effects.

The main systematic effects can be determined in the so-called normal-

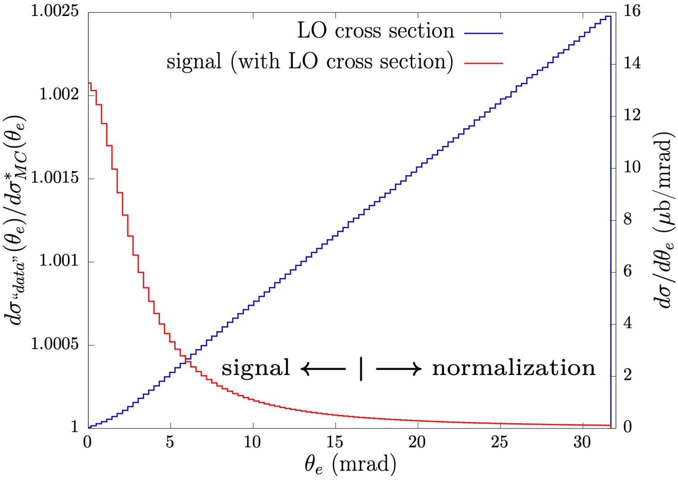

Figure 3.4: The red line shows the effect of the hadronic running of α on the Leading Order muon-electron scattering process, with its scale to the left. In blue, the theoretical LO muon-electron scattering cross-section with respect to the electron scattering angle ϑ_e is plotted with its scale to the right [197].

isation region. This is a specific kinematic region where the effects of the hadronic running of the EM constant $\Delta\alpha_{\text{had}}(t)$ are very small and do not contribute significantly to the total value of a_μ^{HLO}. In this region, as can be seen in figure 3.4, the elastic μe scattering cross section is larger than in the signal region. This allows for a very precise determination of the main systematic effects that need to be taken into account for the measurement in the signal region.

The determination of the systematic uncertainties will be done by introducing nuisance parameters in the fit procedure that was described in Sec. 3.2 using the `combine` tool [198, 199]. They are employed to keep into account any possible modification of the fit parameters due to systematic effects. One nuisance parameter is assigned to each independent systematic effect. More specifically, two kinds of nuisance parameters are used in the MUonE data analysis.

The first kind consists in *normalisation nuisances*, labelled as ν. They are included in the analysis in order to include possible shifts in normalisation between the experimental data and the generated MC samples. They change the number of events in each bin as

$$n_i \to \bar{n}_i = n_i(1+\varepsilon)^\nu, \tag{3.8}$$

where ε indicates the modulus of the relative systematic uncertainty.

Another class of nuisance parameters is composed by the so-called *shape nuisances*. They refer to any systematic effect that modifies the shape of the differential observable. Each insertion of shape nuisance modifies the number of events in each bin as

$$n_i \to \bar{n}_i[1 + s_i(\mu)], \tag{3.9}$$

where $s_i(\mu)$ is a spline function that preserves continuity and differentiability [198]:

$$s_i(\mu) = \begin{cases} \frac{1}{2}\left[(\delta_i^+ - \delta_i^-)\mu + \frac{1}{8}(\delta_i^+ - \delta_i^-)(3\mu^2 - 10\mu^4 + 15\mu^2)\right] & |\mu| \leq 1 \\ \delta_i^+ \mu & \mu > 1 \\ -\delta_i^- \mu & \mu < -1, \end{cases} \tag{3.10}$$

and

$$\delta_i^\pm = \frac{n_i(\mu = \pm 1) - n_i(\mu = 0)}{n_i(\mu = 0)}. \tag{3.11}$$

The main systematic effect comes from MCS in the beryllium target, in particular for electrons that have a large scattering angle ϑ_e which corresponds to low energy E_e. The smearing that is due to MCS effects is parametrised as a Gaussian function on the orthogonal plane with respect to the beam axis and has been studied for electrons with an energy of $E_e \in [12, 20]$ GeV on thin carbon targets in 2017 [200]. The measured angular distributions agree within ±1% with the predictions from GEANT4 simulations.

Another important systematic effect comes from the degree of knowledge of the average beam scale. At the accelerator level, it is known at the level of about 1%. On top of this, the Beam Momentum Station (BMS) can measure individual muons with a 0.8% precision [201]. However, the average beam scale needs to be controlled using μe scattering [191] and the ultimate precision goal for the final detector is about 3 MeV in a week of runtime [202].

A further systematic effect which needs to be controlled is the bias in the angular resolution. As in the MCS smearing, a Gaussian smearing is applied to the angles of the FS particles. The intrinsic angular resolution of the MUonE tracking system will be of about 0.02 mrad. An uncertainty on this quantity of about ±10% is estimated to be a reasonable guess for a fast simulation analysis.

Many precise details on the template fit procedure in the presence of systematic effects can be found in [192]. A description of a test run with muons as well as a first analysis of elastic events in a realistic scenario can be found in [203].

Chapter 4

PRECISION THEORY FOR μe SCATTERING

In Chapter 3, the MUonE experiment was described, as well as the main ideas of the template fit procedure to extract the hadronic running of the fine structure constant in the spacelike region, $\Delta\alpha_{\text{had}}(t)$. The precision goal for MUonE is about 0.3 % on a_μ^{HLO}, which corresponds to about 10 ppm on the μe scattering differential cross section. It is clear that both statistical and systematic experimental uncertainties have to be kept under this threshold. However, the theoretical uncertainties need also to be just as small.

For this reason, there has been in recent times a very strong drive to compute the muon-electron scattering cross section with very high precision. To reach the required precision of 10 ppm on the differential observables, a calculation of NNLO QED effects matched to a QED Parton Shower (PS) is crucial.

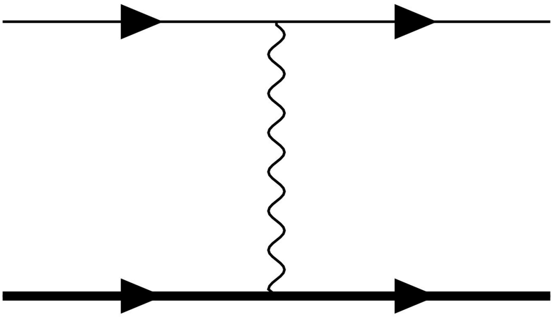

Figure 4.1: The μe scattering LO Feynman diagram. The thicker line indicates the muon current, the lighter one indicates the electron current.

In Sec. 4.1, all the milestones that have been reached towards this goal will be discussed. The calculation and the inclusion of the corrections at NLO and NNLO in the MC event generator MESMER will be dealt with in a much higher detail in sections 4.2 and 4.3, respectively. In Sec. 4.4, a brief overview of the missing pieces to reach the target precision of 10 ppm will be presented.

4.1 Review of calculations for MUonE

After the initial idea of using a spacelike approach to compute a_μ^{HLO} [186] and the experimental consensus that muon-electron scattering would be an ideal process to probe the hadronic running of the EM constant $\Delta\alpha_{\mathrm{had}}(t)$ [187], many theoretical milestones have been reached towards the goal of determining the μe scattering differential cross sections up to the 10 ppm precision.

In order to do so, one can expand the μe scattering cross section in the perturbative series in the fine structure constant α and consider all the contributions order by order.

At LO, the only diagram that contributes to the μe cross section is shown in Fig. 4.1. The cross section can be calculated by performing the following integral:

$$\sigma_0^{\mathrm{QED}} = \int \mathrm{d}\Phi_2 |\mathcal{M}_0|^2 \Theta\left(\mathrm{cuts}\right), \tag{4.1}$$

where the Heavyside theta function signals the application of arbitrary kinematical cuts. The subscript "0" indicates that the calculation is performed at the LO and the term $\mathrm{d}\Phi_2$ is the two-body Lorentz-Invariant Phase Space (LIPS).

The differential cross section of the LO muon-electron scattering process w.r.t. the transferred momentum squared t is given by the following analytic expression [204]:

$$\frac{\mathrm{d}\sigma_0^{\mathrm{QED}}}{\mathrm{d}t} = \frac{1}{\lambda(s, m_\mu^2, m_e^2)} \frac{4\pi\alpha^2}{t^2} \left[\frac{t^2}{2} + st + (s - m_e^2 - m_\mu^2)^2\right], \tag{4.2}$$

where u is the third Mandelstam variable such that:

$$u = \|\mathsf{p}_1 - \mathsf{p}_4\|^2 = \|\mathsf{p}_2 - \mathsf{p}_3\|^2 = 2(m_e^2 + m_\mu^2) - s - t \tag{4.3}$$

and $\lambda(x, y, z)$ is the Källén function:

$$\lambda\left(x, y, z\right) = x^2 + y^2 + z^2 - 2xy - 2xz - 2yz = (x - y - z)^2 - 4yz. \tag{4.4}$$

The contributions at LO due to the exchange of a Z^0 boson are not in principle excluded. However, they are suppressed because of the large Z^0 mass. The interference between the QED LO and the EW LO contributions is suppressed by a factor of $Q^2/M_Z^2 \simeq 10^{-5}$. This term needs to be included in the complete calculation, in order to reach the precision goal of 10 ppm on the differential observables. It was studied and included in the MESMER MC event generator in [205].

At NLO accuracy, the full set of QED and weak corrections was calculated without any approximation and retaining all finite mass effects [205]. Such calculations were then included in the MESMER MC generator. Details on this calculation will be shown in Sec. 4.2. The calculation of QED NLO effects has also been done in another MC code, McMule [206]. Many checks have been performed between the two codes, showing full compatibility.

Many important results were obtained at NNLO in QED. The master integrals for the two-loop planar and non-planar four-point Feynman diagrams were computed in Ref. [207] and in Ref. [208]. In these calculations, the electron mass was set to zero, whereas the muon mass dependence was kept. A procedure to extract the leading electron mass terms for processes that involve particles with large masses from the massless amplitudes was devised in [209] (massification procedure). A subtraction scheme for QED calculations with massive fermions at NNLO was studied in [210] as well as its generalisation at all orders.

The NNLO photonic corrections along the electron line have been implemented into MESMER [211] and McMule [206], including all the finite mass terms. In the former calculation, also the two-loop diagrams where at least two virtual photons connect the electron and muon lines have been computed using the Yennie–Frautschi–Suura (YFS) approach [212]. In this approach, the IR part is calculated exactly and some non-IR remnants have been approximated. Details of this calculation will be provided in Sec. 4.3.1. Moreover, the full set of NNLO leptonic corrections has been calculated in Refs. [213–215] and included in the MESMER MC event generator. All the details related to this calculation will be expanded in Sec. 4.3.2.

The analytic calculation of the two-loop corrections to the amplitude of four-fermion scattering in QED was performed keeping the full dependence on the mass of one fermionic current [216]. The calculation of the complete set of NNLO QED corrections to μe scattering was performed in the McMule framework, keeping full dependency on the muon mass and using the massification procedure on the electron mass [217]. The two-loop hadronic corrections to muon-electron scattering were calculated in Refs. [218] and [219]. The calculation of the two-loop vertices with the insertion of a VP using Master Integral (MI) techniques was performed in [220]. Moreover, possible contamination from New Physics (NP) effects has been studied in [221] and [222]. From these results it is clear that these effects are below the MUonE goal sensitivity.

Some important steps have been taken towards the study of Next-to-Next-to-Next-to-Leading Order (N^{3}LO) calculations for μe scattering. The triple-virtual corrections have been calculated in [223–225], whereas the massless real-virtual-virtual contribution has been calculated in [226].

A collaborative effort started to complete the N^{3}LO calculations for μe scattering [227]

In Ref. [228, 229], the calculation of the $\mu e \to \mu e \pi^0$ cross section was performed, since it could be a possible source of background for the MUonE experiment. Sec. 4.3.3 will be devoted to this calculation. Moreover, the calculation of $\mu X \to \mu X \ell^+ \ell^-$ has been performed in [230, 231]. Chapter 5 will be devoted to all the details of the calculation and the numerical results of this process. An assessment of the corrections that come from the atomic binding of the electrons of the MUonE target has been done in [232].

4.2 Muon-electron scattering at NLO

In this section, the details of the calculation of the full QED and weak NLO corrections to muon-electron scattering will be shown, following Ref. [205]. First, the idea of the calculation and then the numerical impact on a selection of differential observables will be shown in Sections 4.2.1 and 4.2.2, respectively.

4.2.1 The calculation

QED corrections are the most dominant contributions at NLO. The collinear emission of photons from a lepton gives enhanced contributions, that are proportional to $\alpha \ln\left(Q^2/m_\ell^2\right)$ for large Q^2, where m_ℓ is the mass of the lepton and Q^2 is the energy scale where the emission occurs. For this reason, NLO QED corrections are more dominant than the NLO weak corrections.

The QED NLO contributions include the one-loop virtual corrections and the single-photon real corrections. One can write the total QED NLO cross section as:

$$\sigma_1^{\mathrm{QED}} = \sigma_{2\to 2} + \sigma_{2\to 3}, \tag{4.5}$$

where the first term indicates the virtual contribution. This can be written explicitly in terms of the LO and NLO virtual amplitudes $\mathcal{M}_{\mathrm{LO}}$ and $\mathcal{M}_{\mathrm{NLO}}^{\mathrm{v}}$ as in the following relation [205]:

$$\sigma_{2\to 2} = \frac{1}{F} \int \mathrm{d}\Phi_2 \left[\left|\mathcal{M}_{\mathrm{LO}}\right|^2 + 2\,\mathrm{Re}\left(\mathcal{M}_{\mathrm{LO}}^{\dagger} \mathcal{M}_{\mathrm{NLO}}^{\mathrm{v}}(\lambda) \right) \right]. \tag{4.6}$$

In the previous equation, the virtual matrix element depends on the parameter λ. It is a vanishingly small fictitious mass that is assigned to the virtual and real photons in order to regularise the IR singularities. On the other hand, the UV divergences can be treated with the employment of dimensional regularisation. Moreover, the factor F represents the IS flux factor:

$$F = 2\sqrt{(s - m_e^2 - m_\mu^2)^2 - 4m_e^2 m_\mu^2}, \tag{4.7}$$

and $\mathrm{d}\Phi_2$ is the usual two-body LIPS.

The real photon contribution is computed using the PhSp slicing technique together with the photon mass prescription. By imposing an arbitrary energy cutoff ξ such that $\lambda \ll \xi \ll \sqrt{s}$ on the photon energy E_γ and by considering separately the two PhSp regions where $\lambda < E_\gamma < \xi$ and $E_\gamma > \xi$, one can write the real NLO cross section as [205]:

$$\sigma_{2\to 3} = \frac{1}{F}\left(\int_{\lambda < E_\gamma < \xi} \mathrm{d}\Phi_3 |\mathcal{M}^{\mathrm{r}}_{\mathrm{NLO}}|^2 + \int_{E_\gamma > \xi} \mathrm{d}\Phi_3 |\mathcal{M}^{\mathrm{r}}_{\mathrm{NLO}}|\right). \tag{4.8}$$

In the previous equation, $\mathrm{d}\Phi_3$ is the three-body LIPS and $\mathcal{M}^{\mathrm{r}}_{\mathrm{NLO}}$ is the real NLO amplitude where the real photon has the fictitious mass λ. By performing the first integral, Eq. 4.8 becomes:

$$\sigma_{2\to 3} = \eta_s(\lambda, \xi) \int \mathrm{d}\sigma_0^{\mathrm{QED}} + \frac{1}{F}\int_{E_\gamma > \xi} \mathrm{d}\Phi_3 |\mathcal{M}^{\mathrm{r}}_{\mathrm{NLO}}|, \tag{4.9}$$

where the factor $\eta_s(\lambda, \xi)$, which is called *eikonal factor*, is a term that factorises the LO cross section and keeps into account the real emission of soft photons.

The calculation of the matrix elements has been performed using the package FORM [233–235], and the packages LOOPTOOLS [236, 237] and COLLIER [238]. The tree-level and one-loop weak matrix elements have been calculated using RECOLA [239].

4.2.2 Numerical results

In this section the numerical impact of the NLO EW terms on the differential cross section will be shown, for specific observables that are important for the MUonE experiment.

Cross section	Setup 1	Setup 2	Setup 3	Setup 4
$\sigma_0^{\mathrm{QED}}(\mu^\pm)$	1265.060312(7)	245.038910(1)	1265.060312(7)	245.038910(1)
$\sigma_1^{\mathrm{QED}}(\mu^+)$	1325.217(3)	255.8437(5)	1162.447(2)	222.7714(3)
$\sigma_1^{\mathrm{QED}}(\mu^-)$	1323.478(3)	255.1176(5)	1161.888(1)	222.8545(3)
$\delta_1^{\mathrm{QED}}(\mu^+)$	0.047552(2)	0.044094(2)	−0.081114(1)	−0.090874(1)
$\delta_1^{\mathrm{QED}}(\mu^-)$	0.046177(2)	0.041130(2)	−0.081556(1)	−0.090535(1)

Table 4.1: Cross sections in μb for $\mu^\pm e^- \to \mu^\pm e^-$ scattering at LO, σ_0^{QED}, and NLO, σ_1^{QED}, in the four possible Setups and for both μ^+ and μ^-. In the last two lines the relative correction w.r.t. the LO δ_1^{QED} is shown, as defined in Eq. 4.10, for both μ^+ and μ^-. The error is the 1σ MC error [205].

Before detailing the numerical results, it is crucial to introduce four different event selections that were considered in Ref. [205]:

- Setup 1: ϑ_e, $\vartheta_\mu < 100$ mrad, $E_e > 0.2$ GeV;
- Setup 2: ϑ_e, $\vartheta_\mu < 100$ mrad, $E_e > 1$ GeV;
- Setup 3: the same criteria as Setup 1, with the acoplanarity bound: $|\pi - (\varphi_e - \varphi_\mu)| \leq 3.5$ mrad;
- Setup 4: the same criteria as Setup 2, with the acoplanarity bound: $|\pi - (\varphi_e - \varphi_\mu)| \leq 3.5$ mrad.

Three gauge-invariant subsets of all the real and virtual NLO contributions can be determined:

- Corrections on the electron line;
- Corrections on the muon line;
- Box contributions and up-down interference of real photons.

More than 95% of the total contribution to the cross section comes from the first subset. The corrections on the muon leg and the electron-muon leg interference weigh about 10^{-4} to 10^{-3} [205]. At the level of the integrated cross sections, Tab. 4.1 summarises the results of the MC generation with MESMER. One can see that the purely photonic corrections are about 4% to 5% w.r.t. the LO cross sections when no acoplanarity cuts are applied. However, if an acoplanarity cut is performed, the relative correction changes sign and increases in absolute vlaue to about 8% to 9%. The change of sign is due to the higher importance of the soft photon emission.

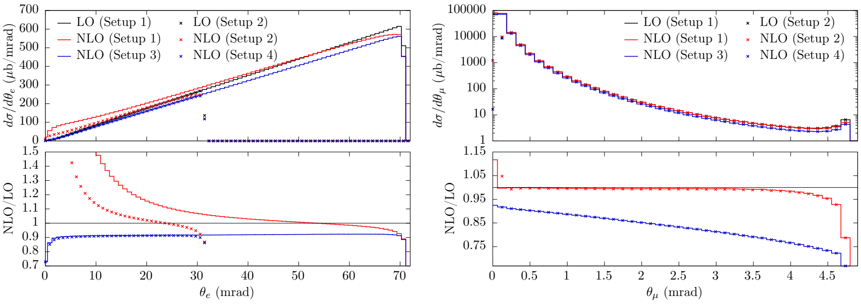

Figure 4.2: In the top plots there are the LO differential cross sections (in black) of the $\mu^+ e \to \mu^+ e$ process, the NLO differential cross section with acceptance cuts (in red) and the NLO differential cross section with also an acoplanarity cut (in blue) w.r.t. the outgoing electron angle ϑ_e (left side) and of the outgoing muon angle ϑ_μ (right side). In the bottom plots, there are the relative NLO QED corrections as a function of ϑ_e (left side) and ϑ_μ (right side) [205].

The relative difference is defined as:

$$\delta_1^{\text{QED}} = \frac{\sigma_1^{\text{QED}} - \sigma_0^{\text{QED}}}{\sigma_0^{\text{QED}}}. \tag{4.10}$$

As was already clarified in Chapter 3, for the MUonE experiment the differential cross sections as functions of angular variables are more relevant than the integrated cross sections. Thus, a differential study is needed. From now on in this section, the focus will be on the process with the positive muon $\mu^+ e \to \mu^+ e$.

In Fig. 4.2, the impact of the NLO QED corrections on the differential cross section w.r.t. the FS electron and FS muon angles, namely $\mathrm{d}\sigma/\,\mathrm{d}\vartheta_e$ and $\mathrm{d}\sigma/\,\mathrm{d}\vartheta_\mu$, is shown. The effect of the NLO contribution without the imposition of acoplanarity cuts becomes non-negligible in the region where ϑ_e is small. This region, as was shown in Fig. 3.4, is where the signal of interest will be extracted to estimate $\Delta\alpha_{\text{had}}(t)$. Therefore, a precise control of the radiative corrections is crucial. Another important piece of information that can be extracted from Fig. 4.2 is that the imposition of an acoplanarity cut reduces the effect of the NLO radiative corrections down to about 10 %, for small electron angles. If one looks at the ϑ_μ distribution, without the application of an acoplanarity cut the differential distribution

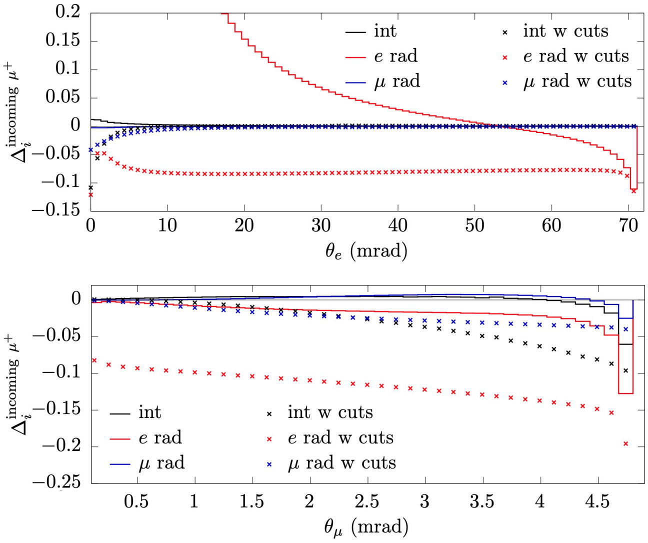

Figure 4.3: Pure photonic contributions to the QED cross section for $\mu^+ e \to \mu^+ e$ plotted as a function of the outgoing electron angle ϑ_e (top plot) and of the outgoing muon angle ϑ_μ (bottom plot). In red, the corrections along the electron line are plotted with(out) acoplanarity cut with a solid line (stars). In blue there are the corrections along the muon line and in black the electron-muon interference terms [205].

has a peak for very small ϑ_μ at the level of about 10 % and increases for larger angles up to the 20 % level. If the acoplanarity cut is imposed, however, the corrections to the cross section increase due to the higher importance of soft photon radiation [205].

By observing the behaviour of the contributions of the three aforementioned gauge-invariant subsets of the QED NLO contributions separately, one can indeed see that the electron line radiation corrections are more dominant than the muon line and the interference contributions, as can be seen in Fig. 4.3.

In Fig. 4.4 the LO and NLO EW contributions to the differential cross section $\mathrm{d}\sigma/\,\mathrm{d}\vartheta_e$ and $\mathrm{d}\sigma/\,\mathrm{d}\vartheta_\mu$ are shown. The LO $\gamma - Z^0$ contributions are at the 10^{-5} level for small ϑ_e and for large ϑ_μ. The NLO EW contributions, on the other hand, are below the 10 ppm precision goal on the differential

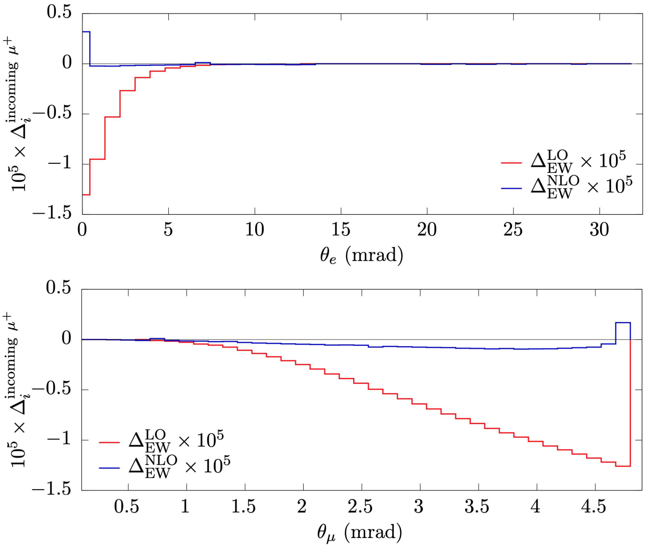

Figure 4.4: Contributions to the $\mu^+ e \to \mu^+ e$ cross section coming from LO EW (red line) and NLO EW (blue line) effects, plotted as a function of the outgoing electron angle ϑ_e (top plot) and of the outgoing muon angle ϑ_μ (bottom plot) [205].

observables [205]. The differential ratios that figure in Fig. 4.4 are defined as follows:

$$\Delta_{\text{EW}}^{\text{LO}} = \frac{\mathrm{d}\sigma_0^{\text{EW}} - \mathrm{d}\sigma_0^{\text{QED}}}{\mathrm{d}\sigma_0^{\text{QED}}} \tag{4.11}$$

and

$$\Delta_{\text{NLO}}^{\text{EW}} = \frac{\left(\mathrm{d}\sigma_1^{\text{EW}} - \mathrm{d}\sigma_0^{\text{EW}}\right) - \left(\mathrm{d}\sigma_1^{\text{QED}} - \mathrm{d}\sigma_0^{\text{QED}}\right)}{\mathrm{d}\sigma_1^{\text{QED}}}. \tag{4.12}$$

The results for the $\mu^- e \to \mu^- e$ process are of the same order of magnitude. They are shown in Ref. [205], along with many more details and studies on the NLO EW corrections.

4.3 Muon-electron scattering at NNLO

The NLO contributions to μe scattering are shown to be much bigger than the precision goal for the MUonE experiment of 10 ppm on the differential observables. For this reason, it is crucial to consider also NNLO corrections to the cross section. Since the NLO weak contributions are already below 10^{-5}, there is no need to calculate also the NNLO weak corrections. The focus of study, thus, will be reserved to the NNLO QED corrections.

The NNLO corrections can be divided into two subsets, as anticipated in Sec. 4.1: NNLO photonic contributions that will be summarised in 4.3.1 and NNLO leptonic contributions. They will be discussed in 4.3.2 with detail.

4.3.1 NNLO photonic contributions

In this section, the details of the calculation of the NNLO QED photonic corrections to μe scattering will be shown, following Ref. [211]. First, the idea of the calculation and then the numerical impact on a selection of differential observables will be shown in Sections 4.3.1.1 and 4.3.1.2, respectively.

4.3.1.1 The calculation

As was in the NLO case, the NNLO photonic contributions include the contributions where the photons are attached onto the electron leg, those attached onto the muon leg and those that are due to the electron-muon leg interference. Each of these subgroups is gauge-invariant. The set of NNLO photonic corrections to μe scattering along a single fermion line is divided into three groups:

- The two-loop pure virtual contribution $\mathrm{d}\sigma_2^{\mathrm{vv}}$. In this group, there are the squared modulus of the one-loop virtual diagrams and the interference between the tree-level μe scattering diagrams with the two-loop virtual diagrams;
- the contribution with a single real photon emission on top of the one-loop corrections $\mathrm{d}\sigma_2^{\mathrm{rv}}$;
- the double bremsstrahlung process $\mathrm{d}\sigma_2^{\mathrm{rr}}$.

The “v” and the “r” in the apices stand for *virtual* and *real*, respectively. All of the groups that were defined above diverge in the IR limit, but can be regularised with the fictitious photon mass prescription, as was already done in Sec. 4.2.1 in the NLO case. Moreover, by defining the energy slicing separator ξ, one can separate soft photon emission from hard photon emission. The pure NNLO contribution to the cross section then becomes [211]:

$$\mathrm{d}\sigma^{\mathrm{QED}}_{2,\,\mathrm{ph}} = \mathrm{d}\sigma_{0\gamma,\,\mathrm{h}}(\xi) + \mathrm{d}\sigma_{1\gamma,\,\mathrm{h}}(\xi) + \mathrm{d}\sigma_{2\gamma,\,\mathrm{h}}(\xi), \tag{4.13}$$

where

$$\begin{aligned} \mathrm{d}\sigma_{0\gamma,\,\mathrm{h}}(\xi) &= \mathrm{d}\sigma^{\mathrm{vv}}_{0\gamma,\,\mathrm{h}}(\lambda) + \mathrm{d}\sigma^{\mathrm{sv}}_{0\gamma,\,\mathrm{h}}(\lambda,\xi) + \mathrm{d}\sigma^{\mathrm{ss}}_{0\gamma,\,\mathrm{h}}(\lambda,\xi) \\ \mathrm{d}\sigma_{1\gamma,\,\mathrm{h}}(\xi) &= \mathrm{d}\sigma^{\mathrm{v}}_{1\gamma,\,\mathrm{h}}(\lambda,\xi) + \mathrm{d}\sigma^{\mathrm{s}}_{1\gamma,\,\mathrm{h}}(\lambda,\xi) \\ \mathrm{d}\sigma_{2\gamma,\,\mathrm{h}}(\xi) &= \mathrm{d}\sigma_{2\gamma,\,\mathrm{h}}(\lambda,\xi). \end{aligned} \tag{4.14}$$

The “h” and the “s” in the subscripts and apices stand for *hard* and *soft*, respectively. The “v” apex indicates the usual *virtual* photon emission. The subscript $_{\#\gamma,\,\mathrm{h}}$ indicate the number of hard photons that are emitted. Each term that appears on the r.h.s. of Eq. 4.13 is independent of the fictitious photon mass λ. The radiation of real soft photons is included with eikonal factors, as was the case for the NLO calculation.

The calculation of the double bremsstrahlung process was performed with FORM [233–235] and the one-loop tensor coefficients and scalar functions were calculated with COLLIER [238] and cross-checked with [240]. The two-loop virtual corrections were calculated in [241]. The diagram with a VP insertion on the vertex photonic correction was removed from the photonic corrections since its enhancement is proportional to $\alpha^2 L^3$ with $L = \ln\left(-t/m_\ell^2\right)$ and is cancelled by the real lepton pair production counterpart. This contribution was not studied in [211] but will be discussed in 4.3.2.

The same reasoning can be applied to the corrections along the muon line. However, as will be shown in 4.3.1.2, they are numerically less important.

One can describe the full two-loop virtual QED contribution using a YFS-inspired approximation. This can be done to study the IR-divergent diagrams [212]. This approach was used to approximate those diagrams where a virtual photon connects the electron and the muon lines on top of the one-loop box diagrams. The remaining part of the contributions that were already described above were calculated exactly [211].

One can start from the exact i-th order matrix element, written in terms of the IR contributions:

$$\begin{aligned}
\mathcal{M}_0 &= \mathcal{T} \\
\mathcal{M}_1 &= \eta\mathcal{T} + \mathcal{M}_1^{\mathrm{R}} \\
\mathcal{M}_2 &= \frac{1}{2}\eta^2\mathcal{T} + \eta\mathcal{M}_1^{\mathrm{R}} + \mathcal{M}_2^{\mathrm{R}} \\
&= -\frac{1}{2}\eta^2\mathcal{T} + \eta\mathcal{M}_1 + \mathcal{M}_2^{\mathrm{R}}.
\end{aligned} \tag{4.15}$$

The term $\mathcal{T}$ represents the tree-level amplitude, $\mathcal{M}_i$ are the full i-loop amplitudes, $\mathcal{M}_i^{\mathrm{R}}$ indicates the non-IR-divergent amplitudes and η is the IR YFS factor. The latter can be written as [211]:

$$\eta = \sum_{i,j=1,4}^{i\leq j} \eta_{ij} = \eta_e + \eta_\mu + \eta_{e\mu} \tag{4.16}$$

where all the terms can be rewritten in terms of the one-loop scalar functions B_0 and C_0:

$$\eta_{ij} = \begin{cases} \dfrac{\alpha}{8\pi} q_i^2 \left[B_0(0, m_i^2, m_i^2) - 4m_i^2 C_0(m_i^2, 0, m_i^2, \lambda^2, m_i^2, m_i^2)\right] & \text{for } i = j \\ \dfrac{\alpha}{\pi} q_i q_j \vartheta_i \vartheta_j \Big[\mathsf{p}_i \cdot \mathsf{p}_j C_0\left(m_i^2, (\vartheta_i \mathsf{p}_i + \vartheta_j \mathsf{p}_j)^2, m_j^2, \lambda^2, m_i^2, m_j^2\right) & \\ \qquad\qquad + \dfrac{1}{4} B_0\left((\vartheta_i \mathsf{p}_i + \vartheta_j \mathsf{p}_j)^2, m_i^2, m_j^2\right)\Big] & \text{for } i \neq j. \end{cases} \tag{4.17}$$

The term q_i is the charge of the i-th particle and ϑ_i equals -1 or 1 for an incoming or an outgoing fermion, respectively. The IR terms η_i factorise the IR divergence of the diagrams with a virtual photon on the i leg, with $i = e$, μ, $e\mu$. If $i = e\mu$, the virtual photon connects the electron and muon legs.

The complete approximate two-loop virtual amplitude $\mathcal{M}_2$ can be written [211]:

$$\begin{aligned}
\mathcal{M}_2 \approx \widetilde{\mathcal{M}}_2 = \mathcal{M}_2^{ee} + \mathcal{M}_2^{\mu\mu} + \mathcal{M}_2^{e\mu} \\
+ \frac{1}{2}\eta_{e\mu}^2\mathcal{T} + \eta_{e\mu}(\eta_e + \eta_\mu)\mathcal{T} + (\eta_e + \eta_\mu)\mathcal{M}_1^{e\mu,\,\mathrm{R}} + \eta_{e\mu}\mathcal{M}_1^{\mathrm{R}},
\end{aligned} \tag{4.18}$$

Cross section	Setup 2	Setup 4
$\sigma_{2,\,\mathrm{ph}}^{\mathrm{QED},\,\mathrm{e}}$	255.5725(5)	224.4796(4)
$\sigma_{2,\,\mathrm{ph}}^{\mathrm{QED},\,\mu}$	244.9706(1)	244.4154(1)
$\sigma_{2,\,\mathrm{ph}}^{\mathrm{QED},\,\mathrm{full}}(\mu^-)$‡	255.205(1)	224.041(1)
$\sigma_{2,\,\mathrm{ph}}^{\mathrm{QED},\,\mathrm{full}}(\mu^+)$‡	256.092(1)	224.088(1)

Table 4.2: Cross sections in μb for $\mu^\pm e^- \to \mu^\pm e^-$ scattering at NNLO, $\sigma_{2,\,\mathrm{ph}}^{\mathrm{QED}}$, in the two Setups. The apices "e", "μ" and "full" indicate the cross sections with corrections along the electron line only, the muon line only and the full approximate contributions, respectively. The digits in the parentheses correspond to 1σ MC error. The double daggers ‡ indicate that the YFS approximation has been used [211].

where $\mathcal{M}_2^{ee}$, $\mathcal{M}_2^{\mu\mu}$ and $\mathcal{M}_2^{e\mu}$ are the two-loop diagrams where the two virtual photons are both attached to the electron leg, the muon leg and one leg each, respectively.

In Eq. 4.18, the approximation consisted in putting the two-loop virtual non-IR remnants to zero $\mathcal{M}_2^{\mathrm{R}} = 0$ where at least two photons connect the electron and muon lines. The size of the non-IR contributions that are put to zero is estimated to be in the range of about $(\alpha/\pi)^2 \ln^2(m_\mu^2/m_e^2) \simeq 6 \times 10^{-4}$ [211]. Since it is larger than the MUonE experiment precision goal of 10 ppm, it will be necessary to include such corrections in MESMER in the future.

4.3.1.2 Numerical results

In this section, the numerical impact of the NNLO photonic contributions to the μe scattering cross section will be shown for specific observables that are important for the MUonE experiment. The following results have been produced with the MESMER MC event generator.

The event selections that were considered are Setup 2 and Setup 4. They were introduced in Sec. 4.2.2 [211]. Moreover, as already done in the NLO case, the only differential observables that will be shown are $\mathrm{d}\sigma/\,\mathrm{d}\vartheta_e$ and $\mathrm{d}\sigma/\,\mathrm{d}\vartheta_\mu$, for the sake of brevity.

In the plots, the percent difference between the NNLO and the NLO predictions, w.r.t. the LO cross section will be shown, since the 10 ppm

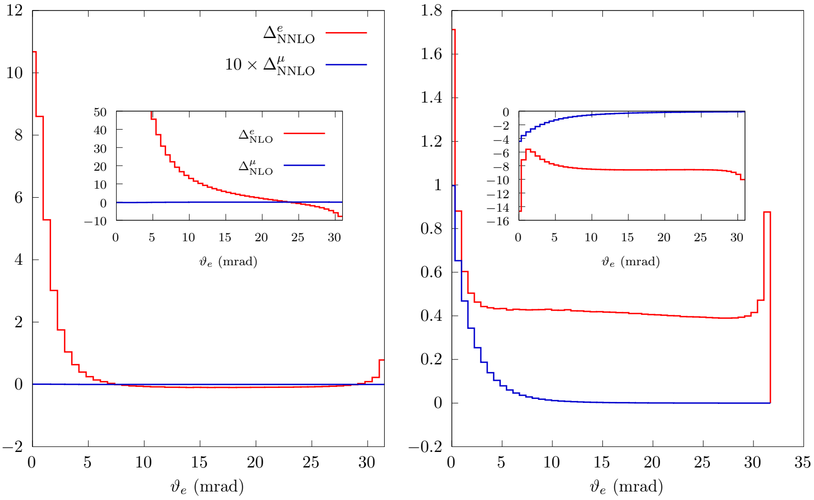

Figure 4.5: In red, NNLO corrections along the electron line for $\mu^\pm e \to \mu^\pm e$ as a function of the FS electron angle ϑ_e. In blue, the corrections along the muon line multiplied by 10. On the l.h.s. Setup 2 is considered, on the r.h.s. Setup 4 is considered. In the insets there are the NLO corrections [211].

are implicitly referred w.r.t. the LO differential cross section:

$$\Delta^i_{\rm NNLO} = \frac{d\sigma_2^{{\rm QED},\, i} - d\sigma_1^{{\rm QED},\, i}}{d\sigma_0^{\rm QED}} \times 100 \tag{4.19}$$

where the apices $i = {\rm e}, \mu, {\rm full}$ refer to corrections where photons are attached only onto the electron line, onto the muon line or to corrections where the full set of YFS-approximated NNLO contributions are included, respectively.

In figure 4.5, the NNLO corrections along a single lepton line for $d\sigma/\, d\vartheta_e$ are shown. The corrections on the electron line remain close to zero for electron scattering angles that are greater $\vartheta_e > 5$ mrad. As ϑ_e approaches zero, they increase up to about 10 %. The correction due to the muon line radiation remains close to zero on all the phase space. If acoplanarity cuts are applied, the shape of the distributions does not significantly change, remaining enhanced for small electron angles.

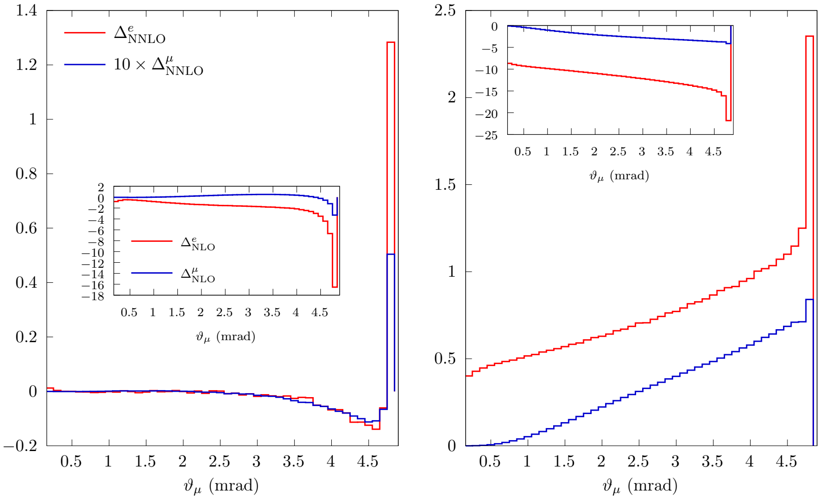

Figure 4.6: The same as 4.5 but plotted against the FS muon angle ϑ_μ [211].

Fig. 4.6 shows the numerical impact of NNLO corrections for the $\mathrm{d}\sigma/\,\mathrm{d}\vartheta_\mu$ differential cross section. If no acoplanarity cuts are applied, the corrections along the electron line remain at the level of 10^{-5} for small angles and decrease to about $-0.14\,\%$ at 4.5 mrad. Then, they increase to about 1.3 % at the kinematical limit. If acoplanarity cuts are applied, the corrections along the electron line increase from about 0.4 % to about 2.4 %. A similar behaviour occurs for the corrections along the muon line. They remain, however, depressed by a factor of about 10 to 30 in certain kinematical regions.

Now, one can look at some differential observables for the full YFS-approximated calculation of the NNLO photonic corrections, with also the interference terms. For the sake of brevity, only the $\mathrm{d}\sigma/\,\mathrm{d}\vartheta_e$ distribution will be presented, in Fig. 4.7. If no acoplanarity cuts are applied, the YFS-calculated NNLO corrections have a very similar shape w.r.t. the exact NNLO corrections along the electron leg. However, in Setup 4, the $\mu^+e^- \to \mu^+e^-$ corrections are very similar to the exact NNLO case on the electron leg above 5 mrad, but they increase to about 6.5 % below this angle. For the $\mu^-e^- \to \mu^-e^-$ process, the corrections remain stable also

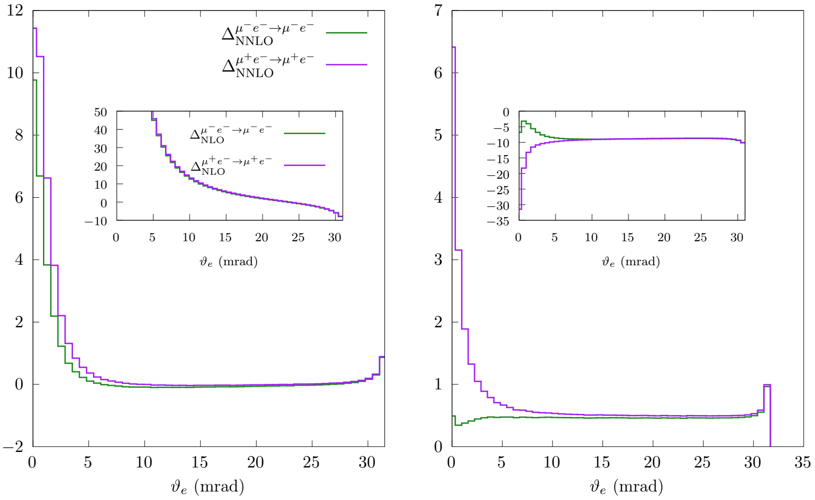

Figure 4.7: In green, the full YFS-approximated NNLO corrections, as in Eq. 4.18 for $\mu^- e \to \mu^- e$ as a function of the FS electron angle ϑ_e. In purple, the same corrections for $\mu^- e \to \mu^- e$. On the l.h.s. Setup 2 is considered, on the r.h.s. Setup 4 is considered. In the insets there are the NLO corrections [211].

for $\vartheta_e < 0.5$ mrad.

It is clear from the study in Ref. [211] that the size of the NNLO photonic corrections w.r.t. the LO differential cross sections is at the level of some 10^{-4} in certain PhSp regions. This suggests that the next step regarding the radiative corrections needs to be the matching of the fixed-order calculation with an all-order resummation procedure. This could be done with a QED PS technique.

4.3.2 NNLO lepton pair contributions

In this section, the calculation of the complete fixed-order NNLO QED corrections that include at least one leptonic pair is presented, following Ref. [213]. The corrections include all the relevant virtual and real contributions, summing over all contributing lepton flavours. After the calculation of the photonic contributions, this set of corrections completes the NNLO QED contributions to μe scattering.

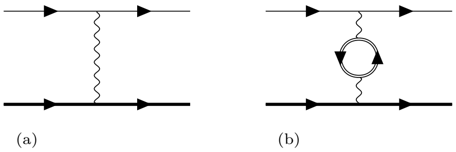

Figure 4.8: The LO diagram of μe scattering, (a), and the NLO diagram, (b), with leptonic corrections. The thicker fermionic line indicates the muon line, whereas the double line closed loop indicates the virtual leptonic contribution due to a generic lepton ℓ [213].

As a first step, the classification of the contributions and the methods used for their calculation are described in Sec. 4.3.2.1. Where it is needed, the computation of the virtual corrections is performed using DR techniques, as has been done for the hadronic calculations in [218,219], without neglecting any finite mass effect. The results of the hadronic NNLO corrections has also been computed in [213] and cross-checked with [218,219]. The size of these contributions is then compared with the leptonic corrections on all the relevant differential distributions for MUonE.

All these corrections have been included in the MESMER MC code: with this tool, numerical results under typical running conditions and event selections of the MUonE experiment can be produced. They will be discussed in Sections 4.3.2.2 and 4.3.2.3.

4.3.2.1 The calculation

The complete set of NNLO leptonic corrections to $\mu^{\pm}e^{-} \to \mu^{\pm}e^{-}$ can be divided into three main subsets:

$$\mathrm{d}\sigma^{\mathrm{QED}}_{2,1} = \mathrm{d}\sigma^{\mathrm{v}}_{2,1} + \mathrm{d}\sigma^{\gamma}_{2,1} + \mathrm{d}\sigma^{\mathrm{r}}_{2,1} \tag{4.20}$$

where the “l” subscript stands for *leptonic*, “v” stands for *virtual* and “r” stands for *real.* The apex “γ” indicates that there is a photon emission. The three terms in the previous equation include different contributions.

The first one, $\mathrm{d}\sigma^{\mathrm{v}}_{2,1}$, contains many diagrams:

- The squared modulus of the NLO VP insertion diagram, in 4.8 (b);

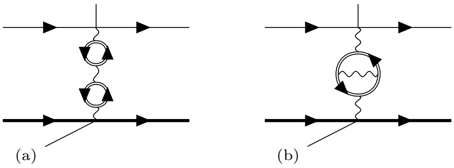

Figure 4.9: On the l.h.s. the NNLO reducible photon VP contribution. On the r.h.s. the QED NNLO irreducible VP contribution [213].

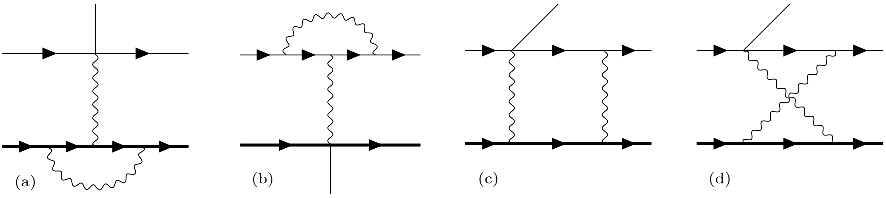

Figure 4.10: NLO virtual photonic corrections [213].

- The interference between the μe scattering LO diagram, in 4.8 (a), with the two-loop diagram with two VP insertions as well as a NLO VP insertion, namely the diagrams in Fig. 4.9 (a) and (b), respectively;
- The interference between the NLO virtual diagram with the VP insertion (Fig. 4.8 (b)) and any one-loop photonic virtual diagram (Fig. 4.10).
- The interference between the LO diagram (Fig. 4.8 (a)) with the two-loop virtual diagrams where the one-loop photonic diagrams have an additional VP correction in the non-loop photon (Fig. 4.11).
- The interference between the LO diagram (Fig. 4.8 (a)) with the two-loop virtual diagrams where the one-loop photonic diagrams have an additional VP correction in the loop photon. The diagrams in 4.12 are IR safe, whereas the diagrams in 4.13 are IR divergent. The IR divergence is cancelled by the interplay with real radiation diagrams that are in the $\mathrm{d}\sigma^{\gamma}_{2,1}$ class, described below.

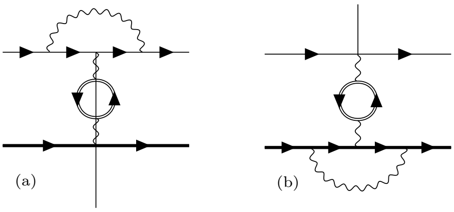

Figure 4.11: Factorisable NNLO contribution with the insertion of a VP on the non-loop photon propagator of the one-loop photonic correction diagrams [213].

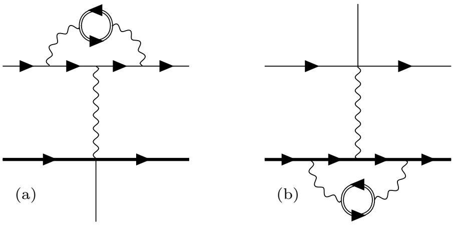

Figure 4.12: NNLO irreducible vertex diagrams [213].

The second set, $\mathrm{d}\sigma^{\gamma}_{2,1}$, includes the diagrams where there are both leptonic VP insertions and real photon emission. In this group of contributions, the interference between the tree-level $\mu e \to \mu e \gamma$ process and the diagrams with a leptonic VP insertion on the photon propagator and a real photon emission (Fig. 4.14) is accounted for.

The third set, $\mathrm{d}\sigma^{\mathrm{r}}_{2,1}$, includes the tree-level $\mu e \to \mu e \ell^+ \ell^-$ process, with $\ell = e, \mu$. The $\tau^+\tau^-$ pair production is kinematically prohibited at the MUonE experiment, given the small CM energy and the big τ mass. In this last set, three gauge-invariant subsets can be determined:

- Real lepton pair production from a photon that is emitted from the electron line (Figs. 4.15 (a) and (b));
- Real lepton pair production from a photon that is emitted from the muon line (Figs. 4.15 (c) and (d));
- Real lepton pair production from peripheral diagrams, also called

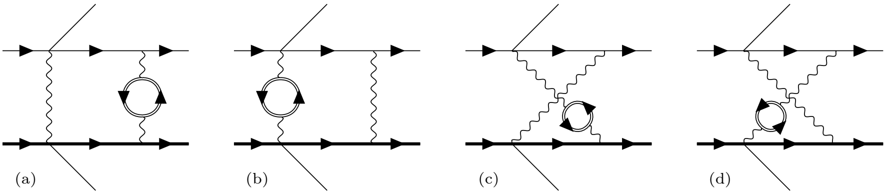

Figure 4.13: NNLO Box diagrams [213].

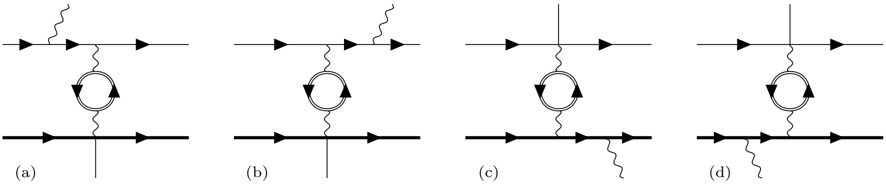

Figure 4.14: NNLO real photon radiation diagrams [213].

trident diagrams (Figs. 4.15 (e) and (f)). The pair is produced in the photon propagator.

The last set of contributions $\mathrm{d}\sigma^{\mathrm{r}}_{2,1}$ is crucial for two main reasons. It represents a four-body final state. This means that in certain kinematic regions two FS particles could escape the MUonE experimental acceptance, thus leaving two seen tracks. This implies that this four-fermion final state could perfectly mimic a signal event. This makes this contribution a reducible background for the MUonE experiment and needs to be precisely studied under MUonE running conditions.

Moreover, the interference between two radiative channels from the same line, when integrated over the PhSp, gives a contribution that is proportional to $\alpha^2 \ln^3(-t/m_\ell^2)$. From previous Bhabha scattering studies [242–249], it is known that this contribution will cancel with a similar term coming from the virtual counterpart, *i.e.* the diagrams in Fig. 4.12. All the other interference terms between the diagrams in Fig. 4.15 cancel out similar contributions with the fully virtual diagrams with closed fermion loop.

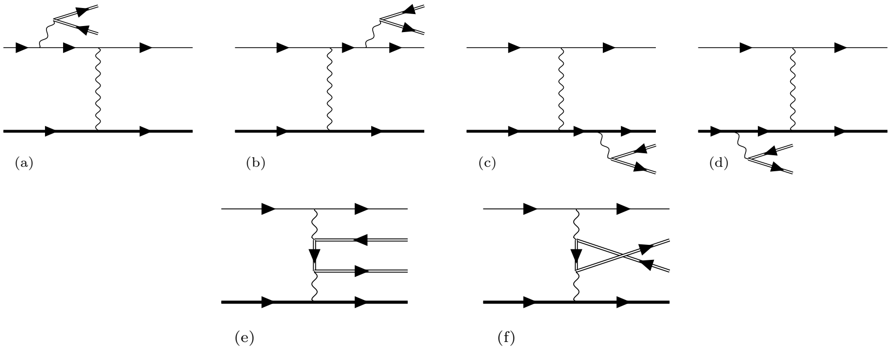

Figure 4.15: Real NNLO lepton pair production $\mu e \to \mu e \ell^+ \ell^-$. The diagrams that exchange the outgoing fermionic lines due to the identity of the FS leptons are not displayed. However, they have been calculated [213].

Details on the NNLO virtual and real-virtual leptonic corrections calculation

The calculation of the purely virtual and the real-virtual leptonic corrections has been performed using DR techniques. The starting point is the NLO amplitudes that were already computed in [205] and already inserted in the MESMER MC event generator. It is known that the insertion of a leptonic VP function on top of a virtual photon in an amplitude amounts to substituting the normal photon propagator with a DR as in the following equation [250–254]:

$$\frac{-ig_{\mu\nu}}{q^2+i\varepsilon} \to \frac{-ig_{\mu\delta}}{q^2+i\varepsilon} i \left(q^2 g^{\delta\lambda} - q^\delta q^\lambda\right) \hat{\Pi}_\ell(q^2) \frac{-ig_{\lambda\nu}}{q^2+i\varepsilon}, \tag{4.21}$$

where $\hat{\Pi}_\ell(q^2)$ is the renormalised VP function obtained from its imaginary part, by considering a SDR:

$$\hat{\Pi}_\ell(q^2) = -\frac{q^2}{\pi} \int_{4m_\ell^2}^{\infty} \frac{\mathrm{d}z}{z} \frac{\operatorname{Im} \hat{\Pi}_\ell(z)}{q^2 - z + i\varepsilon}. \tag{4.22}$$

The mass of the circulating lepton is m_ℓ. Moreover, one can write the imaginary part of the leptonic subtracted VP function as:

$$\mathrm{Im}\,\hat{\Pi}_\ell(z) = -\frac{\alpha}{3}R_\ell(z), \tag{4.23}$$

with

$$R_\ell(z) = \left(1+\frac{4m_\ell^2}{2z}\right)\sqrt{1-\frac{4m_\ell^2}{z}}. \tag{4.24}$$

The term in Eq. 4.21 with $q^\delta q^\lambda$ does not contribute because it is not gauge-invariant. Thus, the final DR that has to substitute the photon propagator reads:

$$\frac{-ig_{\mu\nu}}{q^2+i\varepsilon} \to -ig_{\mu\nu}\left(\frac{\alpha}{3\pi}\right)\int_{4m_\ell^2}^{\infty}\frac{\mathrm{d}z}{z}\frac{1}{q^2-z+i\varepsilon}\left(1+\frac{4m_\ell^2}{2z}\right)\sqrt{1-\frac{4m_\ell^2}{z}}. \tag{4.25}$$

The dispersive integral can be computed using MC techniques in the variable z. The final form of the two-loop purely virtual and real-virtual matrix element is [213]:

$$\mathcal{M}_2(\mu e\to\mu e) = \left(\frac{\alpha}{3\pi}\right)\int_{4m_\ell^2}^{\infty}\frac{\mathrm{d}z}{z}R_\ell(z)\mathcal{M}_1(\mu e\to\mu e;z), \tag{4.26}$$

where $\mathcal{M}_1$ is the one-loop amplitude with the mass of the virtual photon with the VP insertion set to $\sqrt{z}$.

This procedure has been recently used in Refs. [218, 219] to compute the NNLO hadronic corrections to muon-electron scattering.

Details on the NNLO real leptonic corrections calculation

The real lepton pair production from muon-electron scattering $\mu e\to\mu e\ell^+\ell^-$, with $\ell = e,\mu$, is a tree-level $2\to 4$ process. However, the complicated matrix element needs to be integrated with proper sampling techniques. As a matter of fact, the small electron mass and the large PhSp for this process make the integration of the very peaky matrix elements a difficult task.

The QED NNLO real pair production matrix elements have been calculated using FORM [233–235] and their correctness has been cross-checked with the RECOLA package [238, 239].

In the following part of this Section, the momenta are labelled as follows:

- p_1: IS muon
- p_2: IS electron
- p_3: FS muon
- p_4: FS electron
- p_5: FS ℓ^+
- p_6: FS ℓ^-

To be sure of the PhSp implementation and integration, two different parametrisations were chosen and their description follows [213]. The four-body LIPS is defined as:

$$\mathrm{d}\Phi_4 = \int \frac{\mathrm{d}^3\mathbf{p}_3}{(2\pi)^3 2E_3} \frac{\mathrm{d}^3\mathbf{p}_4}{(2\pi)^3 2E_4} \frac{\mathrm{d}^3\mathbf{p}_5}{(2\pi)^3 2E_5} \frac{\mathrm{d}^3\mathbf{p}_6}{(2\pi)^3 2E_6} \times \delta^4\left(\mathsf{p}_1 + \mathsf{p}_2 - \sum_{i=3}^{6} \mathsf{p}_i\right). \quad (4.27)$$

Diagrams in Figs. 4.15 (a) and (b) follow the PhSp separation as in the following equation:

$$\mathrm{d}\Phi_4 = (2\pi)^3 \int \mathrm{d}Q^2\, \mathrm{d}\Phi_3(\mathsf{p}_1 + \mathsf{p}_2 \to \mathsf{p}_3 + \mathsf{p}_4 + \mathsf{Q}) \times \mathrm{d}\Phi_2(\mathsf{Q} \to \mathsf{p}_5 + \mathsf{p}_6). \quad (4.28)$$

The first PhSp parametrisation for the diagram with the IS radiative pair production on the electron line in Fig. 4.15 (a) is defined by the following 8 independent variables:

$$Q^2, \cos\vartheta_4, \phi_4, \cos\vartheta_{56}, \phi_5, E_{56}, \cos\vartheta_5^*, \phi_5^*. \quad (4.29)$$

The variables $\cos\vartheta_5^*$ and ϕ_5^* are generated in the rest frame of the $\ell^+\ell^-$ pair, where $\mathbf{p}_5 + \mathbf{p}_6 = \mathbf{0}$. The two variables ϑ_{56} and ϕ_{56} are the polar and azimuthal angles of the pair with momentum $\mathsf{p}_5 + \mathsf{p}_6$ in the CM frame. The parametrisation of the diagram in Fig. 4.15 (b) is very similar, but the pair polar and azimuthal angles ϑ_{56} and ϕ_{56} are in the CM frame where the $\hat{z}$ axis is directed along $\mathbf{p}_4$. The diagrams with the pair produced after the radiative emission along the muon line do not have a dedicated parametrisation, since these diagrams give rise to logarithms of the type $L = \ln s/m_\mu^2$ which are not leading, since $\sqrt{s} \simeq m_\mu$.

The last important terms that have to be accounted for are the peripheral diagrams, as in Fig. 4.15 (e) and (f). They require a different PhSp parametrisation [255, 256]:

$$\mathrm{d}\Phi_4 = (2\pi)^6 \int \mathrm{d}Q^2_{356}\, \mathrm{d}Q^2_{56}\, \mathrm{d}\Phi_2(\mathsf{p}_1 + \mathsf{p}_2 \to \mathsf{p}_4 + \mathsf{Q}_{356}) \\ \times \mathrm{d}\Phi_2(\mathsf{Q}_{356} \to \mathsf{p}_3 + \mathsf{Q}_{56})\, \mathrm{d}\Phi_2(\mathsf{Q}_{56} \to \mathsf{p}_5 + \mathsf{p}_6). \quad (4.30)$$

The independent variables are:

$$Q^2_{356}, Q^2_{56}, \cos\vartheta_4, \phi_4, \cos\vartheta^*_3, \phi^*_3, \cos\vartheta^{**}_5, \phi^{**}_5, \quad (4.31)$$

where Q^2_{356} and Q^2_{56} are invariant masses, $\cos\vartheta^*_3$ and ϕ^*_3 are generated in the Q_{356} rest frame, and $\cos\vartheta^{**}_5$ and ϕ^{**}_5 are generated in the Q_{56} rest frame. This implementation of the PhSp calculation is symmetrised for when the FS e^+e^- particles are considered to be identical [213].

The second PhSp parametrisation makes use of a different set of independent generated variables:

$$Q^2_{456}, Q^2_{56}, t_{13}, \phi_3, \cos\vartheta^\dagger_{56}, \phi^\dagger_{56}, \cos\vartheta^*_5, \phi^*_5. \quad (4.32)$$

In this parametrisation, which is the one that is present in MESMER, $\mathsf{Q}_{456} = \mathsf{p}_4 + \mathsf{p}_5 + \mathsf{p}_6$, $\mathsf{Q}_{56} = \mathsf{p}_5 + \mathsf{p}_6$, $t_{13} = \|\mathsf{p}_1 - \mathsf{p}_3\|^2$, ϕ_3 is the FS muon azimuthal angle in the $\mathsf{p}_1 + \mathsf{p}_2$ rest frame, $\vartheta^\dagger_{56}$ and $\phi^\dagger_{56}$ are the polar and azimuthal angles of the $5+6$ intermediate-state particle in the $\mathsf{p}_1 - \mathsf{p}_3 + \mathsf{p}_2$ rest frame, and ϑ^*_5 and ϕ^*_5 are the FS ℓ^+ polar and azimuthal angles in the $\mathsf{p}_5 + \mathsf{p}_6$ rest frame.

The variables in this parametrisation are not generated uniformly but are sampled according to the shape and peaks of the matrix elements. Moreover, to closely follow each of the functions peaks, a multi-channel generation has been employed. For example, if an electronic pair is produced, ϕ_3, $\phi^\dagger_{56}$ and ϕ^*_5 are generated with a flat sampling, whereas Q^2_{456} follows the fermion propagator peaking behaviour of $1/Q^2_{456}$, t_{13} follows the peaking behaviour of the photon propagator that connects the electron leg with the muon leg of $1/t_{13}$. The pair invariant mass Q^2_{56} is sampled as $1/Q^2_{56}$. The cosine of the electron pair $\cos\vartheta^\dagger_{56}$ is generated either with the sampling function $1/(1-\beta_2\cos\vartheta^\dagger_{56})$ where β_2 is the FS electron speed in the $\mathsf{p}_1 -$

$\mathsf{p}_3 + \mathsf{p}_2$ rest frame, or with the sampling function $1/(1 - \beta_{13} \cos\vartheta^{\dagger}_{56})$ where β_{13} is the speed of $\mathsf{p}_1 - \mathsf{p}_3$ in the $\mathsf{p}_1 - \mathsf{p}_3 + \mathsf{p}_2$ rest frame, in two different channels. The cosine of the FS pair electron $\cos\vartheta^*_5$ is generated either with the sampling function $1/(1 - \beta'_{13} \cos\vartheta^*_5)$ where β'_{13} is the speed of $\mathsf{p}_1 - \mathsf{p}_3$ in the $\mathsf{p}_5 + \mathsf{p}_6$ rest frame, or with the sampling function $1/(1 - \beta_{24} \cos\vartheta^*_5)$ where β_{24} is the speed of $\mathsf{p}_2 - \mathsf{p}_4$ in the $\mathsf{p}_5 + \mathsf{p}_6$ rest frame, in two different channels.

The identity of the FS particles is kept into account with the inclusion of other channels where there is an exchange between particles $\mathsf{p}_4 \leftrightarrow \mathsf{p}_6$. To correctly sample the emission of the pair from the muon leg (see Figs. 4.15 (c) and (d)), other channels are implemented where the IS electron and FS electron that is not coming from the pair are exchanged with the IS muon and FS muon, namely $\mathsf{p}_1 \leftrightarrow \mathsf{p}_2$ and $\mathsf{p}_3 \leftrightarrow \mathsf{p}_4$ [213].

4.3.2.2 Inputs, cuts and observables

In this section, all the input parameters and the choice of kinematical cuts that were used in Ref. [213] are defined. They will be applied to the calculation described in 4.3.2.1. A selection of the differential cross sections that were studied in Ref. [213] will be then shown in Sec. 4.3.2.3.

The simulations with MESMER were performed with an input muon beam energy of 150 GeV. The FS electron and muon angles are generated with ϑ_e, $\vartheta_\mu < 100$ mrad and the FS electron is generated with an energy of $E_e > 1$ GeV. This choice of generation bounds is based on the MUonE experimental acceptance.

In the $2 \to 2$ kinematics, if the IS muon beam has an energy of $E_\mu = 150$ GeV, the FS muon has an angle $\vartheta_\mu < \widetilde{\vartheta}_\mu = \arccos\left(\sqrt{1 - m_e^2/m_\mu^2}\right) \simeq 4.84$ mrad and an energy of $E_\mu > \widetilde{E}_\mu \simeq 10.28$ GeV, which corresponds to the energy in the laboratory frame of a muon that is scattered backwards in the CM frame. If an additional lepton pair $\ell^+\ell^-$ is produced, there will be a $2 \to 4$ kinematics. This implies that more than two particles could be into acceptance. For this reason, a different event selection criterion needs to be investigated.

One can define a *muon-like* track such that it has $\vartheta_\mu < \widetilde{\vartheta}_\mu$ and $E_\mu > \widetilde{E}_\mu$ and an *electron-like* track such that $\vartheta_e < 100$ mrad and $E_e > 1$ GeV [213]. The final selection criterion, which will be called basic acceptance cuts

(BAC), is to accept exactly two tracks in the detector, one of which has to be *muon-like* and the other has to be *electron-like*.

On top of the BAC, in Ref. [213] a set of additional cut selections was investigated. As will be clear from the study of the differential cross sections displayed in 4.3.2.3, the BAC need to be complemented with some other PhSp restrictions that select elastic events and suppress the reducible background from the pair production. The aforementioned additional cuts are:

- A lower bound on the *electron-like* and on the *muon-like* angles can be defined: $\vartheta_c = 0.2$ mrad, such that $\vartheta_e, \vartheta_\mu > \vartheta_c$. This selection allows to reduce the effect of the peripheral diagrams (Fig. 4.15 (e) and (f)) without losing sensitivity to the running of α for large $|t|$;
- An acoplanarity cut such that $\xi = |\pi - |\phi_e - \phi_\mu|| < \xi_c = 3.5$ mrad, as was already defined in Setups 3 and 4 for the NLO case in Sec. 4.2.2;
- An elasticity cut where the elasticity distance is considered as $\delta < \delta_c = 0.2$ mrad. The distance is the minimum distance between the generated point $(\vartheta_e, \vartheta_\mu)$ and the elastic curve, which is univocally defined from the $2 \to 2$ kinematics. As was already pointed out in Ref. [187], the elastic curve can be parametrised as:

$$\vartheta_\mu(\vartheta_e) = \arctan\left[\frac{2m_e r \cos\vartheta_e \sin\vartheta_e}{E_\mu - r(rE_\mu + 2m_e)\cos^2\vartheta_e}\right], \tag{4.33}$$

where

$$r = \frac{\sqrt{E_\mu^2 - m_\mu^2}}{E_\mu + m_e} \tag{4.34}$$

and the distance is:

$$\delta = \min_{\vartheta_e} \sqrt{(\vartheta_e - \bar{\vartheta}_e)^2 + [\vartheta_\mu(\vartheta_e) - \bar{\vartheta}_\mu]^2}. \tag{4.35}$$

The differential observables that were studied in Ref. [213] are:

$$\frac{\mathrm{d}\sigma}{\mathrm{d}t_{ee}}, \quad \frac{\mathrm{d}\sigma}{\mathrm{d}t_{\mu\mu}}, \quad \frac{\mathrm{d}\sigma}{\mathrm{d}\vartheta_e}, \quad \frac{\mathrm{d}\sigma}{\mathrm{d}\vartheta_\mu}, \tag{4.36}$$

where $t_{ee} = \|\mathsf{p}_2 - \mathsf{p}_4\|^2$ and $t_{\mu\mu} = \|\mathsf{p}_1 - \mathsf{p}_3\|^2$. Following what has been done for the NLO and the NNLO phenomenological reviews in Sections 4.2.2 and 4.3.1.2, only the differential cross sections w.r.t. the FS angles will be shown here. Moreover, the corrections are presented using the differential K factor:

$$K_{\mathrm{NNLO}} = \frac{\mathrm{d}\sigma_{2,1}^{\mathrm{QED}}}{\mathrm{d}\sigma_0^{\mathrm{QED}}}. \tag{4.37}$$

This choice makes it possible to compare the NNLO observables directly with the LO results to which the precision goal of 10 ppm is referred.

4.3.2.3 Numerical results

In this section, the numerical impact of the NNLO leptonic contributions to the μe scattering cross section, as described in Sec. 4.3.2.1, will be shown for the observables and the event selection criteria that were shown in Sec. 4.3.2.2. The following results have been produced with the MESMER MC event generator.

NNLO virtual pair production

As a first step, one can consider the subset of NNLO virtual lepton pair contributions that come from the diagrams in Figs. 4.8 and 4.9, which contribute to the running of the EM constant $\alpha(t)$. In Fig. 4.16, the effects of e, μ and hadrons in the VP at LO, indicated with $\left(\Delta\alpha^{\mathrm{LO}}\right)^2$, and also in the VP at NLO, indicated with $\Delta\alpha^{\mathrm{NLO}}$, are shown. One can see that an electron circulating in $\left(\Delta\alpha^{\mathrm{LO}}\right)^2$ gives positive contributions. They go from about 2.4×10^{-4} for small ϑ_e to about 0.8×10^{-4} at 32 mrad. If also the $\Delta\alpha^{\mathrm{NLO}}$ contribution is considered, the effect is shifted upwards by about 0.5×10^{-4} across the whole ϑ_e range. The effects of muons circulating in the VPs and hadronic blobs is not negligible for about $\vartheta_e \lesssim 15$ mrad, increasing to about 0.6×10^{-4} in both cases. The hadronic corrections have been calculated using the KNT routine [61].

On the r.h.s. of Fig. 4.16, one can see that the effect of $\left(\Delta\alpha^{\mathrm{LO}}\right)^2$ and $\Delta\alpha^{\mathrm{NLO}}$ increases as ϑ_μ increases. The former, for electronic VPs, goes from about 0.8×10^{-4} for small ϑ_μ to about 2.4×10^{-4} at the kinematical limit $\vartheta_\mu = 4.84$ mrad. As in the ϑ_e distribution, the effect of $\Delta\alpha^{\mathrm{NLO}}$ is stable

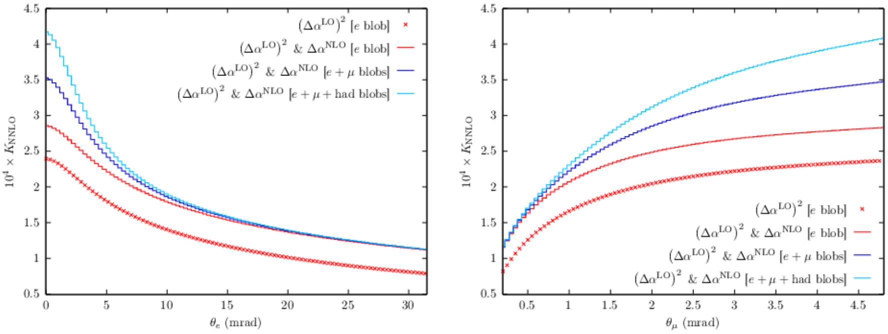

Figure 4.16: On the l.h.s., the differential $K_{\rm NNLO}$ factor w.r.t. the electron scattering angle, including the two diagrams in Fig. 4.9. On the r.h.s., the same quantity is displayed, but is plotted w.r.t. the muon scattering angle. The red crosses show only the effect of the double VP insertion, where only electrons circulate. The red solid line shows the effect of both the double VP and the VP at NLO insertions, where only electrons circulate. The blue solid line shows the same as the red solid line, but both electrons and muons circulate in the VPs. The light blue solid line shows contributions also from hadronic blobs [213].

across the ϑ_μ range and yields about 0.5×10^{-4}. The effects of muons circulating in the VPs and hadronic blobs are monotonically increasing as ϑ_μ increases and go from zero to about 0.6×10^{-4} at $\vartheta_\mu = 4.84$ mrad [213].

In Fig. 4.17, the effects of the two-loop irreducible vertex corrections that come from the diagrams in Fig. 4.12 are shown. The largest effect comes from an electron loop that is attached onto the electronic leg. It is negative and yields about -3.7×10^{-4} around $\vartheta_e \simeq 0$. This term is enhanced by a factor of $\alpha^3 \ln^3(m_e^2/-t)$ and is cancelled by the real counterparts, as shown in the next paragraph where the real lepton pair production numerical effects are discussed. For $\vartheta_e \to 32$ mrad, this contribution decreases to about -0.7×10^{-4}. It is also important to note that the simulations were cross-checked with an analytical calculation that comes from Ref. [257] and the distributions perfectly match. The effect of an electronic loop along the muon line is smaller. It goes from a maximum value of about -1.4×10^{-4} for small ϑ_e and decrease to zero, for larger electron angles. The effects of muon loops are extremely suppressed and they contribute to

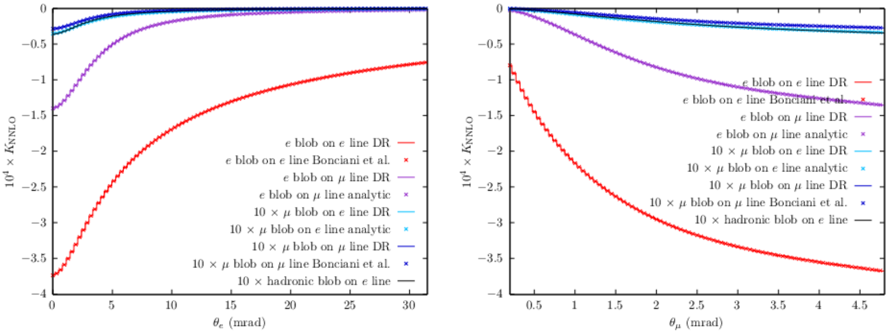

Figure 4.17: On the l.h.s., the differential $K_{\rm NNLO}$ factor w.r.t. the electron scattering angle, including the two diagrams in Fig. 4.12. On the r.h.s., the same quantity is displayed, but is plotted w.r.t. the muon scattering angle. The red solid line shows a e loop on the e leg. The purple solid line shows a μ loop on the e leg. The light blue solid line shows a μ loop on the e leg. The blue solid line shows a μ loop on the μ leg. The black solid line shows the effect of a hadronic loop on the e leg. The results are compared with analytic results that come from [257] or from [213]. The latter are displayed in crosses [213].

at most about 0.5×10^{-5} for small ϑ_e. The muon loops on the muon leg has also been cross-checked with the results from [257] and the results are in perfect agreeement. Moreover, in Appendix A of Ref. [213], an analytical calculation of the insertion of a lepton VP where the internal loop mass is different from the mass of the external fermion line is shown. The results are used as a cross-check of the simulations that make use of the DR. Also in this case, the results are in perfect agreement, as clearly seen in Fig. 4.17. Moreover, the hadronic corrections are of the same order of magnitude as the corrections coming from loops of muons, namely at the level of few ppm.

On the r.h.s. of Fig. 4.17, one can see the same contributions, in the differential K factor plotted w.r.t. the muon angle ϑ_μ. As is the case for the l.h.s. plot, the most important contribution comes from electron loops on the electron line, increasing in absolute value from about 0.8×10^{-4} at $\vartheta_\mu = 0$ to about -3.6×10^{-4} at the kinematical limit of $\vartheta_\mu = 4.84$ mrad. The effect of an electron loop on the muon line increases from zero

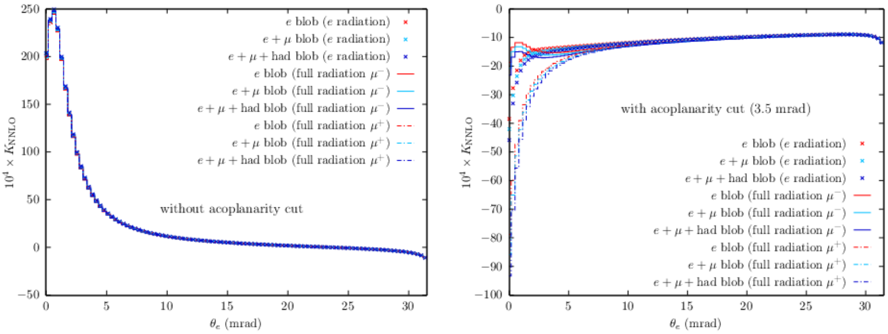

Figure 4.18: On the l.h.s., the differential $K_{\rm NNLO}$ factor w.r.t. the electron scattering angle ϑ_e, including all the NNLO virtual lepton pair corrections and photonic real radiation. On the r.h.s. the same quantity is shown, but acoplanarity cuts are included, as discussed in Sec. 4.3.2.2. The red colour refers to electrons circulating in the VPs. The light blue colour refers to e and μ circulating in the VPs. The blue colour refers to e, μ and hadronic blobs. The crosses indicate that the real photons are emitted along the electron line. The solid histograms indicate the emission from all the legs for an incoming μ^-. The dashdotted histograms indicate the emission from all the legs for an incoming μ^+ [213].

to about -1.4×10^{-4} whereas muon loops and hadronic blobs effects stay below about 0.4×10^{-5}.

In Fig. 4.18, the impact of all the NNLO virtual pair corrections is shown. They include all the photonic one-loop amplitudes with an additional closed lepton VP. They are the sum of the interference of the diagram in 4.8 (a) with the diagrams in 4.11, 4.12 and 4.13 and the interference between 4.8 (b) and the diagrams in 4.10. On top of this, the interference of the diagrams in 4.14 with the same diagrams without the lepton VP insertion is included. As was already known from the NLO studies [205] and the photonic NNLO studies [211], radiative corrections can give non-negligible contributions on the differential observables.

On the l.h.s. of Fig. 4.18, one can see that the virtual pair corrections can have a very large impact on the electron scattering angle ϑ_e distribution, at the level of about about 2.5 % for small ϑ_e. The largest contribution comes from the effect of electron loops on top of real radiation from the

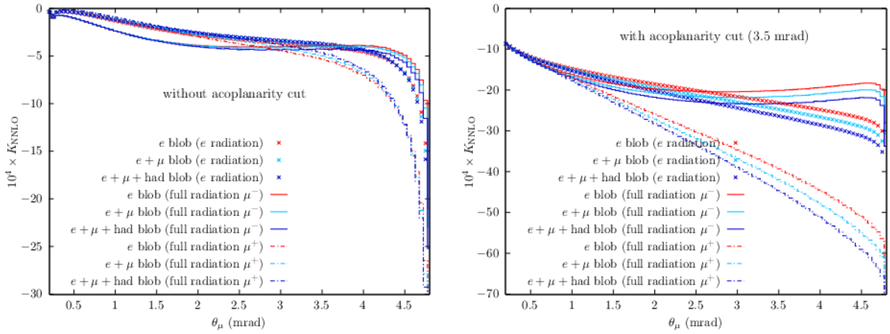

Figure 4.19: The same as 4.18, but plotted w.r.t. the muon scattering angle ϑ_μ [213].

electron line. The sum of all the possible particles circulating in the VP and the contribution of radiation coming from the muon line are almost degenerate with the e blob with emission from the e leg.

On the r.h.s. of Fig. 4.18, one can see the effect of acoplanarity cuts on the same observable. The imposition of such cuts changes sign to the overall correction. The K factor now reaches about $-1\,\%$ at small electron scattering angles for the full radiation and with e, μ and hadronic blobs in the VPs. The contribution from the electron loop and radiation from the electron leg reaches about $-0.4\,\%$ for small scattering angles and decreases to about $-0.1\,\%$ for $\vartheta_e \to 32$ mrad.

On the l.h.s. of Fig. 4.19 the K_{NNLO} is plotted w.r.t. the muon scattering angle. The effects increase in absolute value from zero at $\vartheta_\mu \simeq 0.2$ mrad to about $-0.2\,\%$ for $\vartheta_\mu = 4.84$ mrad for the e, μ loops and hadronic blobs with radiation from all the external legs. In the plots, the distributions for $\vartheta_\mu < 0.2$ mrad are not shown because the corrections peak at very high values, making the plot difficult to read. This is due to the fact that the LO differential cross section is extremely small below 0.2 mrad due to the imposed cuts. The shape of the distribution is very peaked for large muon angles, while it is constant at about -5×10^{-4} for $\vartheta \lesssim 3.5$ mrad. In general, the plot shows that the effect is dominated by the electron loop insertion. On the r.h.s. of Fig 4.19, one can see that the shape of the differential K factor is slightly modified. The contributions are monotonically increasing

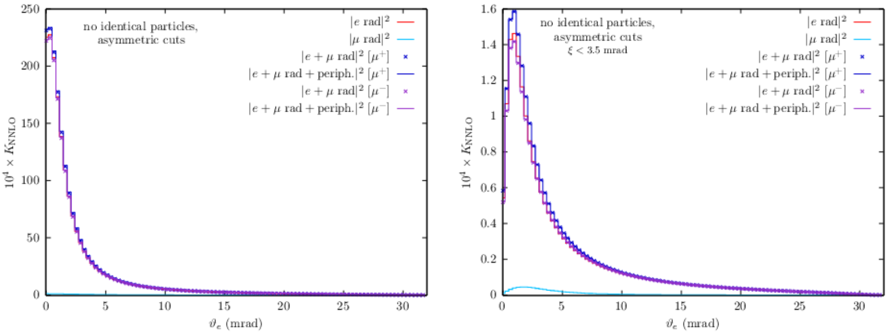

Figure 4.20: On the l.h.s., the differential K_{NNLO} factor w.r.t. the electron scattering angle ϑ_e for various real e^+e^- production processes, without identical FS particles. On the r.h.s. the same quantity is shown, but acoplanarity cuts are included, as discussed in Sec. 4.3.2.2. The red and light blue solid lines refer to radiative processes where the pair is exclusively emitted from the electron and muon leg, respectively. The blue solid lines and blue crosses refer to processes where the pair is emitted from the electron and muon leg, and all the possible real channels in Fig. 4.15 with all the relative interference terms, respectively, for an incoming beam of μ^+. The purple solid lines and crosses show the same as the blue ones, but for an incoming beam of μ^- [213].

in absolute value and go from about $-0.1\,\%$ for $\vartheta_\mu \simeq 0.2$ mrad to about $-0.7\,\%$ for the e, μ loop and hadronic blob insertion with radiation from all the external legs. The application of elasticity cuts does not significantly change the shape and size of the virtual corrections. As will be shown in the next paragraph, however, they greatly reduce the size of the real pair production effects [213].

NNLO real pair production

In this section, the impact of the emission of a real lepton pair from μe scattering is shown. As an intermediate step, the process has been studied in an academic case where the real lepton pair is treated in an inclusive way. This has been done to exclude all the contributions where the final state leptons are exchanged, due to their indistinguishability. This corresponds to the calculation of the $\mu^\pm e^- \to \mu^\pm e^- \tau^+ \tau^-$ process, with $m_\tau = m_e$.

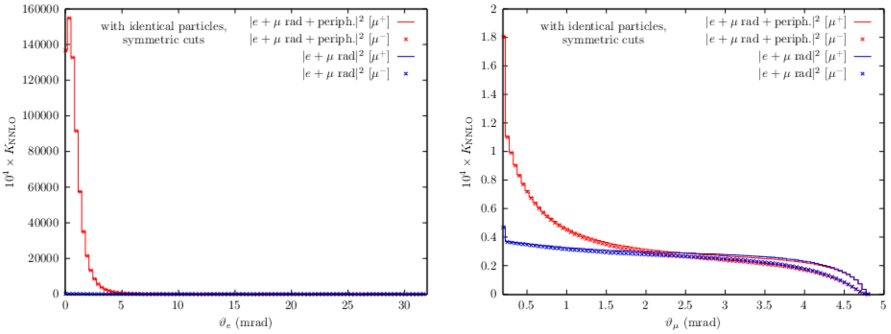

Figure 4.21: On the l.h.s., the differential K_{NNLO} factor w.r.t. the electron scattering angle ϑ_e for various real e^+e^- production processes, with identical FS particles. On the r.h.s. the same quantity is shown, but plotted w.r.t. the muon scattering angle ϑ_μ. The solid lines refer to processes with an IS μ^+ beam. The crosses refer to processes with an IS μ^- beam. The colour red indicates that all the diagrams in Fig. 4.15 contribute, including all the interference terms. The colour blue indicates that only the radiative diagrams contribute, with all the relative interference terms. [213].

On the l.h.s. of Fig. 4.20, one can clearly see that a large contribution to the cross section comes from the pair production from the radiative diagrams where the photon is emitted from the electron line. This contribution, for small electron angles $\vartheta_e \to 0$, peaks at about 2.5 %. For $\vartheta_e > 10$ mrad the impact of real e^+e^- production goes to zero very quickly. The enhancement of the K_{NNLO} factor is due to the fact that the LO cross section is vanishing for small electron angles. For this reason, acoplanarity cuts had been devised already in Ref. [205] as a way to tame the radiative peaks for small ϑ_e.

On the r.h.s. of Fig. 4.20 the effect of the application of the acoplanarity cut is visible. The shape of the distribution is not changed w.r.t. the l.h.s. plot. However, the peaking behaviour at small ϑ_e is reduced to about 1.6×10^{-4} for the full set of contributions. It is also worth noting that in this case the contribution from the peripheral diagrams is almost negligible. Moreover, in Ref. [213], the effect of real $\mu^+\mu^-$ production has been studied. It was shown that this process gives a completely negligible contribution, reaching a few 10^{-8} in the differential observables w.r.t. the LO differential

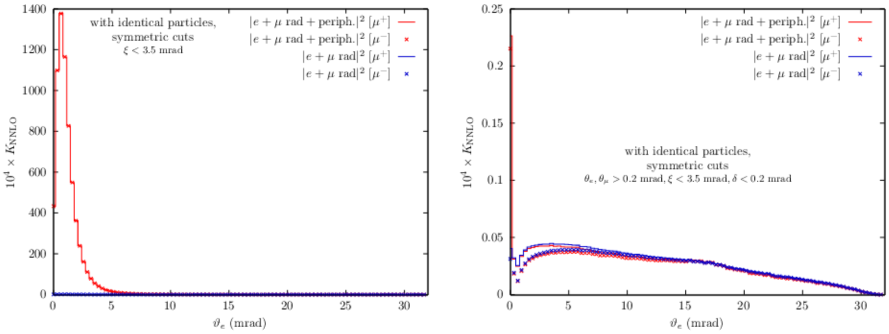

Figure 4.22: The same as the l.h.s. plot of Fig. 4.21. On the l.h.s. also the acoplanarity cut has been imposed. On the r.h.s., the cut on the minimum electron and muon scattering angles as well as the elasticity cut have been included, as described in Sec. 4.3.2.2 [213].

cross section.

After discussing the inclusive case, in order to give a realistic assessment of the effect of real pair production in the MUonE experiment, one has to devise a more realistic event selection. In the MUonE experiment, each charged lepton can produce a visible track in the detector. Thus, for real lepton pair production processes, one could potentially have four distinct tracks in the detector. In order to mimic an elastic event, however, only two tracks need to be into acceptance. One of them has to be *muon-like* and the other one has to be *electron-like*, as discussed in Sec. 4.3.2.2. Moreover, the MUonE experiment does not distinguish an electron from a positron, since no magnetic field is applied to the tracker area.

For this reason, the calculation of $\mu^\pm e^- \to \mu^\pm e^- e^+ e^-$ with all the due crossings in the FS electrons due to the fact that particles are identical has been performed. On top of this, consistent event selection criteria need to be imposed, such that identical particles are not distinguished in the final state.

Since there is no possibility to discriminate the electron that comes from the tree-level process with the electron or positron of the pair, the exchanged momentum can get very close to zero, thus enhancing the cross section and the distributions in certain kinematical regimes, especially at

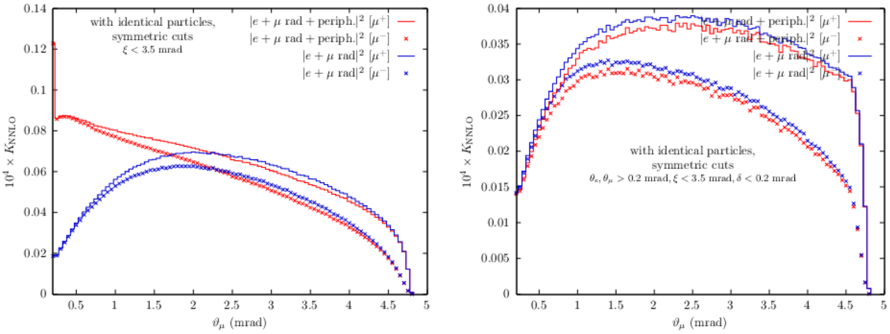

Figure 4.23: The same as the r.h.s. plot of Fig. 4.21. On the l.h.s. also the acoplanarity cut has been imposed. On the r.h.s., the cut on the minimum electron and muon scattering angles as well as the elasticity cut have been included, as described in Sec. 4.3.2.2 [213].

the border of the PhSp. In Ref. [213], it was shown that the peripheral diagrams hugely contribute to this effect, as will be shown in the next paragraphs.

On the l.h.s. of Fig. 4.21, it is clear that the effect of the peripheral diagrams gives a dramatic contribution for small electron angles, $\vartheta_e < 5$ mrad, if only the BAC are imposed and the FS electrons and positron are considered as indistinguishable. On the r.h.s. of Fig. 4.21, the effect of the peripheral diagrams is also visible. The distribution is peaked for small muon angles ϑ_μ and has a plateau for $\vartheta_\mu > 1.5$ mrad. The enhanced configurations correspond to events with small momentum transfer, where the sensitivity of the MUonE experiment to the hadronic running of alpha $\Delta\alpha_{\mathrm{had}}(t)$ is very high. The imposition of a dedicated selection cut is mandatory to control these very big effects which could potentially spoil the MUonE experimental analyses.

On the l.h.s. of Fig. 4.22, the effects of the acoplanarity cut imposition on the realistic e^+e^- production process are shown w.r.t. the ϑ_e distribution. It is clear that many acoplanar events are rejected by this cut. However, for small electron angle, a sharp peak at the level of about 10 % still remains, driven by the peripheral diagrams. For $\vartheta_e > 5$ mrad, the pair production contributions are greatly suppressed.

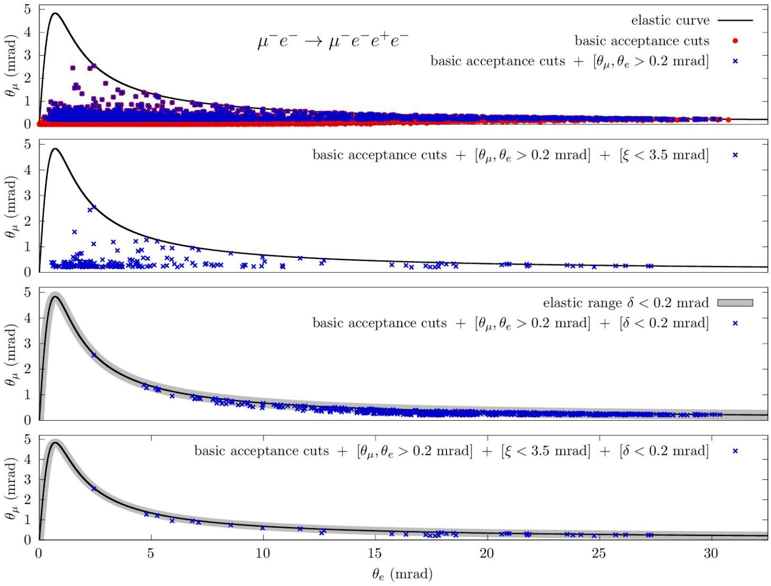

Figure 4.24: Scatter plot of 5×10^5 generated points for the $\mu^- e^- \to \mu^- e^- e^+ e^-$ process. In the top panel, BAC and minimum electron and muon angle cuts have been imposed. In the second panel, BAC, minimum electron and muon angle cuts and the acoplanarity cut have been imposed. In the third panel, BAC, minimum electron and muon angle cuts and the elasticity cut have been imposed. In the bottom panel, all cuts have been imposed. The black line is the correlation curve defined in 4.33 [213].

On the r.h.s. of Fig. 4.22, the effects of all the cuts described in 4.3.2.2 on the realistic e^+e^- production process are shown w.r.t. the ϑ_e distribution. This contribution is reduced to the ppm level over the whole ϑ_e range.

The same conclusions can be traced from the r.h.s. plot in Fig. 4.23. The imposition of all the cuts that were described in Sec. 4.3.2.2 reduces the differential K_{NNLO} to a maximum value of 0.4 ppm, which is lower than the MUonE sensitivity goal.

A much clearer effect of each of the imposed cuts can be seen in Fig. 4.24, which shows the scatter plot in the $(\vartheta_e, \vartheta_\mu)$ plane of the generated events, in comparison with the correlation curve that was written in Eq. 4.33. In the top panel, if only BAC are imposed, it is clearly visible that many of the events (red circles) are very far from the elastic curve, which defines what an elastic event looks like for the tree-level process. If a minimum angle threshold is imposed, all the events with a very small muon angle are rejected (blue crosses). In the second panel from the top, the effect of the acoplanarity cut is shown. In the third panel from the top, the effect of the elasticity cut is shown. In this case, it is clear that the only accepted events are those who stay close to the elastic curve. From this plot, one can also note that the acoplanarity and elasticity cuts seem to have a partially complementary behaviour on the events that they reject. In the fourth panel, the combination of all the cut choices can be seen. As already seen in the differential distributions, this combination is very effective in reducing the real electron pair production, mitigating a potentially very large background. With all the cuts imposed, the rejection efficiency was calculated to be of about 99.993%, confirming again the effectiveness of this choice of cuts [213].

4.3.3 π^0 production in μe scattering

The NNLO virtual hadronic corrections were studied in Refs. [218, 219] and were included in the MESMER MC event generator in [228]. The corresponding real-emission contributions are the $\mu^\pm e \to \mu^\pm e \pi^+ \pi^-$, $\mu^\pm e \to \mu^\pm e \pi^0 \pi^0$ and $\mu^\pm e \to \mu^\pm e \pi^0$ processes. After the studies on the lepton pair production in μe scattering, it is clear that the charged pion pair production is a very suppressed channel. As a matter of fact, the available PhSp is very constrained by the low CM energy at the MUonE experiment. Moreover, a realistic event selection makes the cross section vanishing. For these reasons, the only possible channel that is available at MUonE is the single neutral pion production. This process is enhanced for small electron and muon scattering angles where the sensitivity to $\Delta\alpha_{\text{had}}(t)$ is very high. Moreover, since the main decay mode for the neutral pion is $\pi^0 \to \gamma\gamma$, the two FS photons are not detected in the MUonE experimental setup. This means that the $\mu^\pm e \to \mu^\pm e \pi^0$ process has exactly the same signature in the detector as the one of $\mu e \to \mu e$ scattering.

In Sec. 4.3.3.1, the calculation of the $\mu^\pm e \to \mu^\pm e \pi^0$ cross section is described. In Sec. 4.3.3.2, the impact on some relevant differential observables will be shown.

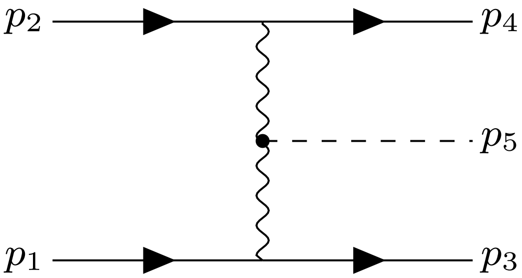

Figure 4.25: The LO Feynman diagram for the process $\mu e \to \mu e \pi^0$ [228].

4.3.3.1 The calculation

In this section, the calculation of the single neutral pion production from muon-electron scattering is presented, following Ref. [228]. From now on, the momenta are labelled as follows:

- p_1: IS muon
- p_2: IS electron
- p_3: FS muon
- p_4: FS electron
- p_5: FS π^0

and the corresponding Feynman diagram is represented in Fig. 4.25.

In order to calculate the matrix element, one can start from the $\pi^0\gamma\gamma$ interaction Lagrangian density:

$$\mathcal{L}_\mathrm{I} = \frac{g}{2!}\varepsilon^{\mu\nu\kappa\lambda}F_{\mu\nu}F_{\kappa\lambda}\varphi_{\pi^0}, \tag{4.38}$$

where a form factor $F_{\pi^0\gamma^*\gamma^*}(p^2, q^2)$ that depends on the two photon virtualities needs to be inserted [258]. From the Lagrangian, one can compute the Feynman rule for the $\pi^0\gamma\gamma$ vertex:

$$-4ig\varepsilon_{\mu\nu\kappa\lambda}p^\nu q^\lambda F_{\pi^0\gamma^*\gamma^*}(p^2, q^2), \tag{4.39}$$

where p and q are the four-momenta of the photon propagators.

In the Feynman rule, a coupling constant g can be seen. In order to obtain its value, one can exploit a relation that holds between the coupling g and the neutral pion decay width $\Gamma_{\pi^0\to\gamma\gamma}$ [258]:

$$g^2 = \frac{4\pi\Gamma_{\pi^0\to\gamma\gamma}}{m^3_{\pi^0}}, \tag{4.40}$$

where $m_{m_{\pi^0}}$ is the neutral pion mass, taken as $m_{\pi^0} = 134.9766$ MeV [259]. Moreover, the decay width $\Gamma_{\pi^0\to\gamma\gamma}$ is related to the f_π parameter by the following relation:

$$\Gamma_{\pi^0\to\gamma\gamma} = \frac{\alpha^2 m^3_{\pi^0}}{64\pi^3 f^2_\pi}. \tag{4.41}$$

If one takes a value of $f_\pi = 0.092388$ GeV [260], all the components to calculate the matrix element are known.

In Ref. [228], the calculation of the exact tree-level matrix element for $\mu e \to \mu e \pi^0$ was performed using FORM [233–235], keeping all the finite mass terms. Moreover, the form factor has been calculated using the resonance chiral symmetric model with SU(3) breaking in Ref. [260].

The PhSp can be parametrised using the following decomposition [228]:

$$\mathrm{d}\Phi_3 = (2\pi)^3 \int \mathrm{d}Q^2\, \mathrm{d}\Phi_2(\mathsf{p}_1 + \mathsf{p}_2 \to \mathsf{p}_3 + \mathsf{Q})\, \mathrm{d}\Phi_2(\mathsf{Q} \to \mathsf{p}_4 + \mathsf{p}_5). \tag{4.42}$$

The set of independent variables that are generated in order to calculate the PhSp is:

$$\vartheta_\mu, \varphi_\mu, Q^2, \vartheta^*_e, \varphi^*_e. \tag{4.43}$$

The two variables ϑ^*_e and φ^*_e are generated in the rest frame of the pair 45, namely $\mathbf{p}_4 + \mathbf{p}_5 = \mathbf{0}$. This calculation was then inserted into the MESMER MC event generator.

The results in Ref. [228] are checked in a tuned comparison with the event generator EKHARA [261, 262].

4.3.3.2 Numerical results

In this section, the numerical impact of the single neutral pion production from muon-electron scattering $\mu e \to \mu e \pi^0$ will be shown, for typical running conditions and event selections of the MUonE experiment.

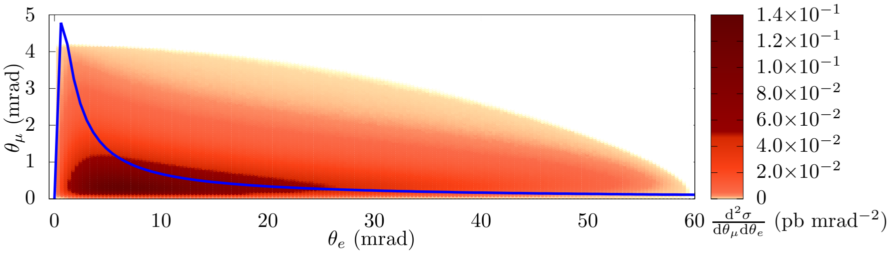

Figure 4.26: The configuration space for the $\mu e \to \mu e \pi^0$ process plotted w.r.t. the electron scattering angle ϑ_e and the muon scattering angle ϑ_μ, with BAC. The colour gradient represents the doubly differential cross section $\mathrm{d}^2\sigma/\,\mathrm{d}\vartheta_e\,\mathrm{d}\vartheta_\mu$. In blue, there is the elasticity curve as in Eq. 4.33 [228].

The pion production cross section is expected to be suppressed w.r.t. the LO μe scattering by a factor of about $g^2 m_{\pi^0}^2 \sim 10^{-6}$. Indeed, the total cross section for this process, with the incoming muon beam of energy $E_\mu = 150$ GeV and the IS electron at rest is [228]:

$$\sigma_{\pi^0} = 6.53589(6)\,\mathrm{pb}. \tag{4.44}$$

On top of this, if one considers the BAC that were designed in [205, 211, 213], with a minimum FS electron energy of $E_e = 0.2$ GeV, the cross section is [228]:

$$\sigma_{\pi^0}^{0.2\,\mathrm{GeV}} = 2.69836(4)\,\mathrm{pb}. \tag{4.45}$$

For $E_e > 1$ GeV, the cross section is [228]:

$$\sigma_{\pi^0}^{1\,\mathrm{GeV}} = 1.61597(3)\,\mathrm{pb}. \tag{4.46}$$

These values have to be compared with a tree-level μe scattering elastic cross section of about $\sigma_0^{0.2\,\mathrm{GeV}} \sim 1265\,\mu\mathrm{b}$ and $\sigma_0^{1\,\mathrm{GeV}} \sim 245\,\mu\mathrm{b}$. From these integrated cross sections, it is clear that $\mu e \to \mu e \pi^0$ is not a numerically relevant background process at MuonE. However, given the enhancements of this process at small electron angles shown in Fig. 4.26, a differential study on the FS muon and electron angles will be shown. As was the case in Sec. 4.3.2.3, the differential ratio of the π^0 production cross section with the LO μe scattering is plotted:

$$K_{\pi^0} = \frac{\mathrm{d}\sigma_{\pi^0}}{\mathrm{d}\sigma_0^{\mathrm{QED}}}. \tag{4.47}$$

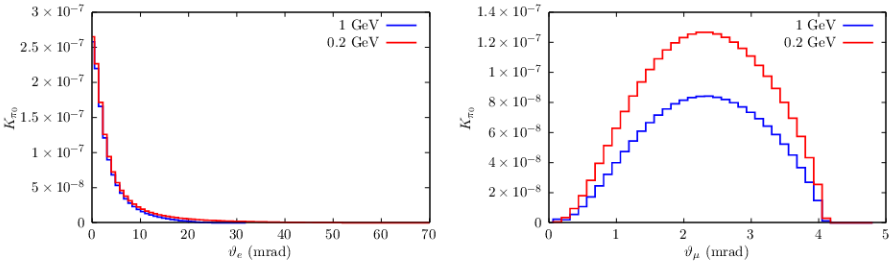

Figure 4.27: On the l.h.s., the differential K_{π^0} factor w.r.t. the electron scattering angle ϑ_e. On the r.h.s. the same quantity is shown, but plotted w.r.t. the muon scattering angle ϑ_μ. The red curve represents the choice of cuts where the minimum energy is $E_e > 0.2$ GeV. The blue curve represents the choice of cuts where the minimum energy is $E_e > 1$ GeV [228].

On the l.h.s. of Fig 4.27, one can see that the impact of the neutral pion production yields at most about 3×10^{-7} for small ϑ_e and very quickly decreases as the electron scattering angle increases. This behaviour holds both for $E_e > 1$ GeV and for $E_e > 0.2$ GeV. On the r.h.s. of Fig 4.27, one can see that the impact of the neutral pion production yields at most about 1.3×10^{-7} for $E_e > 0.2$ GeV and at most about 8×10^{-8} for $E_e > 1$ GeV. More differential distributions are plotted in Ref. [228] but have been excluded in this section, for the sake of brevity.

The investigation on the differential K ratios confirms that the $\mu e \to \mu e \pi^0$ process surely does not constitute a problematic background source for MUonE, since they are way below the 10 ppm precision goal for the experiment [228].

4.4 What do we need for the 10 ppm?

In this section, a brief wish-list of the missing pieces that will surely be needed in order to reach a precision of about 10 ppm on the theoretical calculation of the differential μe cross section will be written.

As was shown in Sec. 4.3, the impact on the differential observables for the NNLO fixed-order contributions are at the level of some 10^{-4} in certain regions of the PhSp, which is higher than the 10 ppm goal. For this reason, the missing IR-non-divergent terms of the NNLO photonic corrections that were approximated in Ref. [211] will need to be calculated.

Moreover, when soft and/or collinear radiation is emitted, large logarithms will be present in the cross section formula. If one performs a N^{n}LO fixed-order calculation, the cross section contains terms proportional to:

$$\alpha^2 \left(\alpha \ln \frac{m^2}{Q^2} \right)^n \tag{4.48}$$

that might not be small, since the logarithmic term is not necessarily small.

The theoretical error that comes with the MC calculation needs to include all the missing higher-order terms. In order to reduce this error, a procedure of resummation of all the large collinear logarithms needs to be devised and implemented in the MESMER MC event generator, for example using a QED PS approach. The MUonE required precision goal is expected to be reached with a full NNLO+PS calculation.

Chapter 5

Lepton pair emission in μX scattering

In Chapter 4, the state of the art of precision theory for muon-electron scattering was reviewed. The higher-order calculations that have been performed using the MC event generator MESMER were described in a more detailed way.

On top of the μe scattering higher-order corrections that are needed to reach the 10 ppm precision goal on the differential cross section, it is also crucial to address all the possible physics background processes that could spoil the measurement. In this regard, in Sec. 4.3.2, the calculation of the $\mu^\pm e^- \to \mu^\pm e^- \ell^+ \ell^-$, where $\ell = e$, μ, was discussed. Moreover, in Sec. 4.3.3 the calculation of the $\mu^\pm e^- \to \mu^\pm e^- \pi^0$ process as a possible source of reducible background for the MUonE experiment was shown.

In this section, the calculation of the lepton pair production in the muon-nucleus scattering, namely $\mu^\pm X \to \mu^\pm X \ell^+ \ell^-$ will be shown, following [230]. In Sec. 5.1, details on the calculation will be provided. In Sec. 5.2, the input variables and the definition of the event selection cuts that were used will be shown. In Sec. 5.3, the impact on some relevant differential observables will be shown.

5.1 The calculation

In the MUonE experiment, as already shown in Chapter 3, the muon beam impinges on a fixed beryllium or carbon target. The process that is used to extract the hadronic running of the EM constant $\Delta\alpha_{\mathrm{had}}(t)$ is the scattering of the muons onto electrons. However, the electrons are bound in the low Z target. For this reason, the main source of background in the MUonE experiment has been identified as the scattering of the IS muon with the nucleus [191]. The cross section of the nuclear processes is proportional to Z^2 while μe scattering is proportional only to Z.

When the muon interacts with the nucleus at rest, a real lepton pair can be produced. It is crucial to carefully study this process because, in certain kinematic regions, it could mimic an elastic event. As a matter of fact, when one of the FS leptons is not detected, two possible tracks can be reconstructed in acceptance. On top of this, it could be a relevant background process also for possible NP studies at the MUonE experiment where light mediators decay in a e^+e^- pair [263–265].

The process $\mu^\pm X \to \mu^\pm X e^+ e^-$ is included and implemented in the Geant4 simulation toolkit [266, 267] and is based on Refs. [268, 269]. In this implementation, the muon scattering angle ϑ_μ is always neglected. Since the MUonE experiment needs a very precise measurement on the FS lepton angles within acceptance, this approximation is not valid. Hence, a fully differential calculation of the pair production from muon-nucleus scattering was required [230].

From now on, the momenta are labelled as follows:

- p_1: IS muon
- p_2: FS muon
- p_3: FS ℓ^+
- p_4: FS ℓ^-

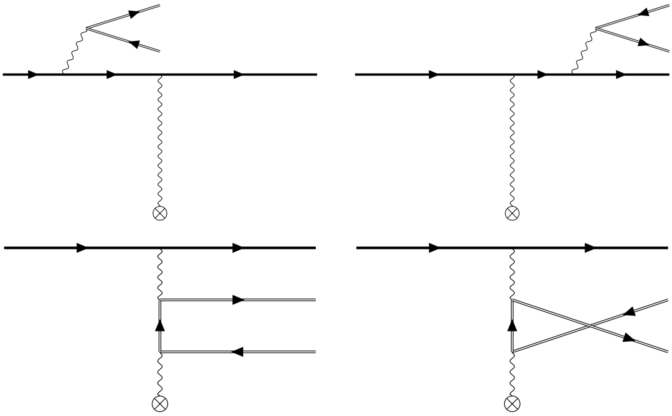

Figure 5.1: The four diagrams that contribute for $\mu X \to \mu X \ell^+ \ell^-$ [230].

where $\ell = e, \mu$. Due to the low CM energy at typical MUonE running conditions and to the high tau lepton mass m_τ, the production of a real $\tau^+\tau^-$ pair is negligible w.r.t. the MUonE precision goal of 10 ppm. For this reason, tau lepton pair production was not considered in Ref. [230].

The muon-nucleus scattering process is described as the scattering of a muon in an external Coulomb potential that is generated by the nucleus X at rest in the laboratory rest frame. An approximation has been used in this calculation as the nucleus is considered to never have a recoil from the scattered muon. This means that in this process the total energy is conserved, whereas the total three-momentum is not. Moreover, the nucleus is considered to have a spatial charge distribution which is closely connected to the electric form factors that are known from Refs. [270, 271].

In Fig. 5.1, there are the four tree-level diagrams that contribute to the process under consideration. As was the case for the $\mu^\pm e^- \to \mu^\pm e^- \ell^+ \ell^-$ process, the pair can be emitted from the incident muon via a radiated photon that creates a lepton pair or via the virtual photon that is exchanged with the nucleus. The latter diagrams are called *peripheral diagrams*, or *trident diagrams*.

The matrix elements of this process have been calculated using FORM [233–235] and cross-checked with Package-X [272, 273], keeping into account all the finite mass effects.

The calculation is performed assuming that the nucleus, which is considered as point-like and with charge Ze, creates the Coulomb potential $A_\mu(\mathsf{x})$ that interacts with the IS muon. On top of this, to keep into account that the nucleus has a finite size, a form factor $F(|\mathbf{q}|)$ is inserted, where $\mathbf{q}$ is the three-momentum that is transferred from the virtual photon to the nucleus. The form factor is related to the nuclear spatial charge distribution in spherical coordinates $\rho(r)$ via a Fourier transformation:

$$F(|\mathbf{q}|) = \frac{4\pi}{Ze}\int_0^\infty \mathrm{d}r r^2 \rho(r) \frac{\sin(|\mathbf{q}|r)}{|\mathbf{q}|r}. \tag{5.1}$$

In the previous equation, the charge distribution is normalised such that:

$$4\pi \int_0^\infty \mathrm{d}r r^2 \rho(r) = Ze. \tag{5.2}$$

In general, the choice of the spatial charge distribution affects the behaviour of the form factor. In Ref. [230], different models for the same isotope are used, as was done in [274, 275].

Different parametrisations were considered [230]:

- One-point Fermi (1pF) model. The spatial charge distribution is parametrised as:

$$\rho(r) = \frac{\rho_0}{1+\exp\frac{r-c}{z}}, \tag{5.3}$$

  where ρ_0 is a constant that is included in the model such that the distribution is normalised:

$$\rho_0 = \frac{-Ze}{8\pi z^3 \,\mathrm{Li}_3\left(-\exp\frac{c}{z}\right)}, \tag{5.4}$$

  $z \simeq 0.52$ fm is the surface thickness and c is the half-density radius that depends on the root-mean-square (rms) charge radius;
- modified harmonic oscillator (MHO) model. The spatial charge distribution is parametrised as:

$$\rho(r) = \rho_0'\left(1+\omega\frac{r^2}{a^2}\right)\exp\left(-\frac{r^2}{a^2}\right), \tag{5.5}$$

where ρ_0' is a constant that keeps into account the normalisation of the distribution:

$$\rho_0' = \frac{Ze}{4\pi}\frac{8}{a^3\sqrt{\pi}(2+3\omega)}, \tag{5.6}$$

a and ω are input parameters that can be extracted from the fit of this model with experimental data;

- Fourier–Bessel (FB) expansion. The spatial charge distribution is parametrised as:

$$\rho(r) = \begin{cases} \displaystyle\sum_{i=1}^{n} a_i \, J_0\left(\frac{k\pi r}{R}\right) & r \leq R \\ 0 & r > R. \end{cases} \tag{5.7}$$

In the previous definition of $\rho(r)$, $J_0(x)\sin(x)/x$ is the zeroth order spherical Bessel function, and R is an input parameter. Moreover, the coefficients a_i are defined so that the following relation holds:

$$\sum_{i=1}^{n} a_i \frac{(-1)^{i+1}}{i^2} = Ze\frac{\pi}{4R^3}. \tag{5.8}$$

In Ref. [230], the 1pF model for the EM form factor was used both for $\mu\,\mathrm{Be} \to \mu\,\mathrm{Be}\,\ell^+\ell^-$ and for $\mu\,\mathrm{C} \to \mu\,\mathrm{C}\,\ell^+\ell^-$, using the nuclear radii that were categorised in Ref. [276]. Moreover, an alternative parametrisation for each nucleus has been implemented in the calculation. For the process that involves the beryllium nucleus, also the MHO model has been studied. For the process that involves the carbon nucleus, also the FB expansion has been included, following [277, 278].

The PhSp can be parametrised starting from the usual three-body PhSp unit volume:

$$\mathrm{d}\Phi_3 = \prod_{i=2}^{4} \frac{\mathrm{d}^3\mathbf{p}_i}{(2\pi)^3 2E_i}\delta\left(E_1 - \sum_{j=2}^{4} E_j\right). \tag{5.9}$$

In the previous equation, E_i is the energy of the i-th particle, with three-momentum given by $\mathbf{p}_i$.

As was already the case for the real lepton pair production from μe scattering, a multi-channel approach has been implemented in the

MESMER MC event generator, to improve the convergence of integration. Four channels corresponding to the four diagrams in Fig. 5.1 were designed. In the following list, for each sampling channel, the specific form of the PhSp parametrisation will be shown [230]:

Channel 1: IS radiation:

$$\mathrm{d}\Phi_3 = \frac{1}{4(2\pi)^2}\,\mathrm{d}Q^2\,\mathrm{d}E_Q\,\mathrm{d}\cos\vartheta_Q\,\mathrm{d}\phi_Q\,\mathrm{d}\cos\vartheta_2\,\mathrm{d}\phi_2 \\ \times E_Q|\mathbf{Q}|\,\mathrm{d}\Phi_2(\mathsf{Q}\to\mathsf{p}_3+\mathsf{p}_4). \quad (5.10)$$

In the previous equation, $Q^2 = \|\mathsf{p}_3+\mathsf{p}_4\|^2$ is the squared invariant mass of the leptonic pair $\ell^+\ell^-$ that is emitted from the IS muon. The term $\mathrm{d}\Phi_2(\mathsf{Q}\to\mathsf{p}_3+\mathsf{p}_4)$ is the two-body LIPS where the pair decays into two leptons. In this channel, the z axis of the laboratory rest frame is assumed parallel to the three-momentum of the IS muon. The Q^2 term is sampled as $1/Q^2$. The FS muon polar angle ϑ_2 is sampled as $1/|\mathbf{q}|^4$, where the momentum exchanged between the muon and the nucleus was introduced, namely $\mathsf{q} = \mathsf{p}_1-\mathsf{p}_2-\mathsf{p}_3-\mathsf{p}_4$. The pair momenta are generated in the $\ell^+\ell^-$ rest frame, namely where $\mathbf{Q} = \mathbf{0}$. The azimuthal angle of the FS muon is generated according to an uniform distribution. All the momenta are generated in the rotated reference frame where $\phi_2 = 0$ and then are rotated by ϕ_2, since the system has a cylindrical symmetry around the z axis.

Channel 2: FS radiation:

$$\mathrm{d}\Phi_3 = \frac{1}{4(2\pi)^2}\,\mathrm{d}Q^2\,\mathrm{d}E_Q\,\mathrm{d}\cos\vartheta_Q\,\mathrm{d}\phi_Q\,\mathrm{d}\cos\vartheta_2\,\mathrm{d}\phi_2 \\ \times E_Q|\mathbf{Q}|\,\mathrm{d}\Phi_2(\mathsf{Q}\to\mathsf{p}_3+\mathsf{p}_4). \quad (5.11)$$

In the previous equation, ϑ_Q is the polar angle of the lepton pair three-momentum $\mathbf{Q}$, whereas ϕ_Q is the corresponding azimuthal angle. In this sampling channel, unlike the previous one, the z axis is considered such that it is parallel to the FS muon three-momentum $\mathbf{p}_2$. The pair angles are thus generated with $\phi_2 = 0$. The generation of the lepton pair momenta p_3 and p_4 follow the same reasoning of CHANNEL 1, as the Q^2 term is sampled as $1/Q^2$ and the FS muon polar angle ϑ_2 is sampled as $1/|\mathbf{q}|^4$. All the other variables are sampled uniformly.

CHANNEL 3: Peripheral diagram:

$$\begin{aligned} \mathrm{d}\Phi_3 = & \frac{1}{8(2\pi)^9}\,\mathrm{d}|\mathbf{p}_2|\,\mathrm{d}|\mathbf{p}_3|\,\mathrm{d}\phi_2\,\mathrm{d}\phi_3\,\mathrm{d}\phi_4\,\mathrm{d}\cos\vartheta_2\,\mathrm{d}\cos\vartheta_3 \\ & \times \mathrm{d}\cos\vartheta_4 \frac{|\mathbf{p}_2|^2}{E_2}\frac{|\mathbf{p}_3|^2}{E_3}\sqrt{(E_\mu - E_2 - E_3)^2 - m_\ell^2}. \end{aligned} \tag{5.12}$$

In the previous equation, E_μ is the IS muon energy and m_ℓ is the mass of the lepton of the pair. Also in this channel, as was the case for the two radiative ones, all the momenta are generated in the frame where $\phi_2 = 0$ and then are rotated by ϕ_2. The FS muon polar angle ϑ_2 is sampled as $1/\|\mathsf{p}_1 - \mathsf{p}_2\|^2$, ϑ_3 is sampled as $1/(\|\mathsf{p}_1 - \mathsf{p}_2 - \mathsf{p}_3\|^2 - m_\ell^2)$ and ϑ_4 is sampled as $1/|\mathbf{q}|^4$.

CHANNEL 4: Crossed peripheral diagram:

$$\begin{aligned} \mathrm{d}\Phi_3 = & \frac{1}{8(2\pi)^9}\,\mathrm{d}|\mathbf{p}_2|\,\mathrm{d}|\mathbf{p}_4|\,\mathrm{d}\phi_2\,\mathrm{d}\phi_3\,\mathrm{d}\phi_4\,\mathrm{d}\cos\vartheta_2\,\mathrm{d}\cos\vartheta_3 \\ & \times \mathrm{d}\cos\vartheta_4 \frac{|\mathbf{p}_2|^2}{E_2}\frac{|\mathbf{p}_4|^2}{E_4}\sqrt{(E - E_2 - E_4)^2 - m_\ell^2}. \end{aligned} \tag{5.13}$$

The same comments as in CHANNEL 3 apply here, but with the exchange of the pair leptons, namely $\mathsf{p}_3 \leftrightarrow \mathsf{p}_4$.

5.2 Inputs, cuts and observables

In this section, all the input parameters and choices of kinematical cuts that were used in Ref. [230] are defined. They will be applied to the calculation described in Sec. 5.1. A selection of the differential cross sections that were studied in Ref. [230] will be then shown in Sec. 5.3.

The energy of the incoming muon beam is fixed at 160 GeV and the momentum is directed towards the centre of the nucleus. As was already done for the calculation of the corrections at NLO and NNLO in Sections 4.2, 4.3.1 and 4.3.2, one can define the BAC [230]:

- $0.2\ \text{mrad} < \vartheta_\mu < 4.84\ \text{mrad}$, $E_\mu > 10.23$ GeV, $\vartheta_e < 32$ mrad and $E_e > 0.2$ GeV.

Since the lepton pair production is very enhanced for small muon scattering angles, a cut on the muon minimum angle was included in the BAC to reduce the cross section. This has the effect of selecting the elastic μe scattering events, rejecting most of the unwanted background.

For the process $\mu X \to \mu X e^+ e^-$, the cuts on the electron angle ϑ_e and on the electron energy E_e are applied to both the e^+ and the e^- of the produced pair. That is because the MUonE experiment does not distinguish the charge of the FS particles in acceptance. For the process $\mu X \to \mu X \mu^+ \mu^-$, the assumption that only one FS muon is reconstructed as a muon and the other particles are reconstructed as electrons is made [230]. This choice is made because in the real experiment the event where two muons are reconstructed in the final state will be rejected. As a matter of fact, the signature of the $\mu X \to \mu X \mu^+ \mu^-$ process is different from the elastic μe scattering event. Thus, in order to produce the phenomenological results that will be discussed in Sec. 5.3 if only one muon satisfies the cuts on ϑ_μ and E_μ, it will be considered as the *muon track*, whereas all the other FS muons will have to satisfy the cuts on ϑ_e and E_e. If more than one muon satisfies the cuts on ϑ_μ and E_μ, the *muon track* will be chosen at random, while the others will be treated as electrons.

All the events of this process can have either two distinct tracks in the detector or three tracks. Two-track events are those where the reconstructed particles are exactly one muon and one electron. The muon satisfies the selection cuts on ϑ_μ and E_μ, whereas only one of the FS electrons satisfies the cuts on ϑ_e and E_e. This case study is very important to address because these events mimic the signal of interest of the MUonE experiment, which is the elastic μe scattering signature.

On the other hand, three-track events are those where all the involved particles (one muon and two reconstructed electrons) satisfy the respective cuts. In order to keep into account the spatial resolution of the MUonE silicon trackers, if two tracks are sufficiently collinear, they will be considered as a single track. More specifically, if the angular separation of two tracks is less than the angular sensitivity $\delta\vartheta < 20\ \mu\text{rad}$, the number of tracks will be reduced by one.

Additional selection cuts have been studied in Ref. [230] and have been

Process	Cross section (nb)
$\mu^+\,\mathrm{Be} \to \mu^+\,\mathrm{Be}\,e^+e^-$	488.31(25)
$\mu^-\,\mathrm{Be} \to \mu^-\,\mathrm{Be}\,e^+e^-$	488.38(27)
$\mu^+\,\mathrm{Be} \to \mu^+\,\mathrm{Be}\,\mu^+\mu^-$	10.624(28)
$\mu^-\,\mathrm{Be} \to \mu^-\,\mathrm{Be}\,\mu^+\mu^-$	10.625(27)
$\mu^+\,\mathrm{C} \to \mu^+\,\mathrm{C}\,e^+e^-$	1102.58(55)
$\mu^-\,\mathrm{C} \to \mu^-\,\mathrm{C}\,e^+e^-$	1103.08(63)
$\mu^+\,\mathrm{C} \to \mu^+\,\mathrm{C}\,\mu^+\mu^-$	24.111(55)
$\mu^-\,\mathrm{C} \to \mu^-\,\mathrm{C}\,\mu^+\mu^-$	24.106(61)

Table 5.1: Total cross section for $\mu^\pm X \to \mu^\pm X \ell^+\ell^-$ for $X = \mathrm{Be}$, C and for $\ell = e$, μ [230].

applied to the $\mu X \to \mu X \ell^+\ell^-$ process:

- *Maximum transferred momentum*: $|\mathbf{q}|^2 < 0.6$ GeV^2. This threshold corresponds to the maximum three-momentum that can be exchanged in the tree-level Mott scattering process, with an IS muon energy of $E_\mu = 160$ GeV and a FS muon scattering angle of $\vartheta_\mu = 4.84$ mrad.
- *Acoplanarity cut*: $\xi = |\pi - |\phi_e - \phi_\mu|| < \xi_c = 400$ mrad, as was similarly defined in Sections 4.2.2, 4.3.1.2 and 4.3.2.2;
- *Elasticity cut*: $\delta < \delta_c = 0.2$ mrad. The elasticity distance is the minimum distance between the generated point $(\vartheta_e, \vartheta_\mu)$ and the elastic curve, which is univocally defined from the $2 \to 2$ kinematics, as already shown in Sec. 4.3.2.2.

Since the three-track events can be rejected experimentally, the acoplanarity and elasticity selection cuts have been applied only to the two-track events.

5.3 Numerical results

In this Section, the numerical impact of the $\mu^\pm X \to \mu^\pm X \ell^+\ell^-$ cross section as described in Sec. 5.1, will be shown for both differential and integrated observables and for the event selection criteria that were described in Sec. 5.2. The following results have been produced with the MESMER MC event generator.

$E_{e^+e^-}$ (GeV)	MESMER (μb)	Geant4 (μb)	Difference
5	47.700(74)	45.986	+3.7 %
10	12.080(20)	12.082	−0.02 %
20	2.737(54)	2.766	−1.0 %
40	0.5213(88)	0.543	−4.0 %

Table 5.2: Comparison between MESMER and Geant4 for $\mu^+\,\mathrm{C} \to \mu^+\,\mathrm{C}\,e^+e^-$ [230].

As a first step, the total cross section for the processes under study will be shown. They are obtained using the BAC as defined in Sec. 5.2 and are shown in Tab. 5.1. The reference tree-level Mott scattering integrated cross section with the same cut selection is 4.064 mb for beryllium and 9.145 mb for carbon.

In order to be sure that the calculation is correct, a number of internal and external cross-checks have been performed. As said in Sec. 5.1, this calculation was already implemented in the Geant4 simulation toolkit, although with some structural differences. It is natural, therefore, to compare the solidity of the results from MESMER with those that come from Geant4. For this reason, the cross section with a fully inclusive angular acceptance and with a cut on the minimum energy of the emitted pair $E_{e^+e^-}$ has been computed. The results are summarised in Tab. 5.2 for various pair energy thresholds. As can be seen, the relative difference between the two simulations is always below 4 %.

In addition to this, the fully inclusive cross section of the $\mu^+\,\mathrm{C} \to \mu^+\,\mathrm{C}\,\mu^+\mu^-$ process can be directly compared with the analytical expression that comes from Ref. [279]. In this case, the result obtained with MESMER is 196.3(9) nb, compared with the analytical value of 196.74 nb.

In addition to the integrated cross section, it is crucial to investigate the differential impact of this background process, since the MUonE experimental precision goal is referred to the differential observables. As was the case for all the calculations that were discussed in Chapter 4, only the differential cross sections w.r.t. the FS electron and muon angles $d\sigma/\,d\vartheta_e$ and $d\sigma/\,d\vartheta_\mu$ will be shown, for the sake of brevity. More phenomenological studies on the lepton pair production from muon-nucleus scattering can be found in Ref. [230].

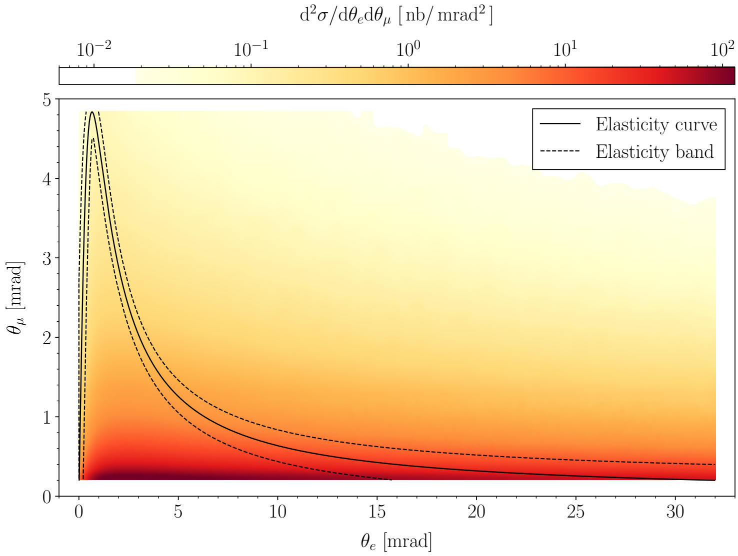

Figure 5.2: Double differential cross section $d^2\sigma/\, d\vartheta_e\vartheta_\mu$ when there are two accepted tracks for the $\mu^+\,\mathrm{C} \to \mu^+\,\mathrm{C}\,e^+e^-$ process. The solid line indicates the elastic curve as defined in Eq. 4.33. The two dotted lines indicate the region where the distance from the elastic curve is less than the elasticity cut value of $\delta_c = 0.2$ mrad [230].

As a first step, it is important to study the process with only the imposition of the BAC. A good characterisation of the process can be seen in the double differential cross section, as in Fig. 5.2. The plot shows that the pair production is very enhanced at small muon scattering angles. This was expected, as was the case in the real lepton pair production [213]. Moreover, this confirms the soundness of the approximation in the Geant4 calculation where the muon scattering angle is always considered as null, namely $\vartheta_\mu = 0$. Another important piece of information that can be extracted from the plot is that in the normalisation region, *i.e.* for $\vartheta_\mu \gtrsim 15$ mrad, the contribution is not negligible near the elastic curve. This means that for a precise determination of the signal in that region, the calculation of this background process is very important.

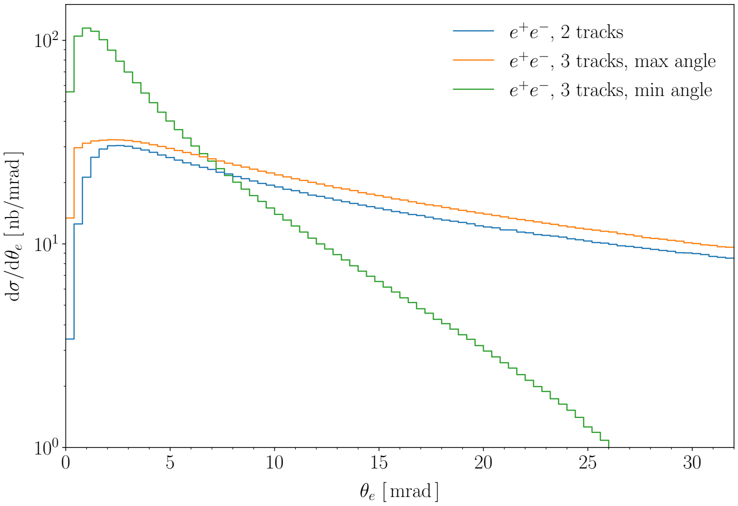

Figure 5.3: Differential cross section or the $\mu^+\,\mathrm{C} \to \mu^+\,\mathrm{C}\,e^+e^-$ process w.r.t. the electron scattering angle ϑ_e. In this plot, the BAC have been imposed. The blue histogram represents the two-tracks case. The orange histogram represents the three-tracks case plotted w.r.t. the maximum electron angle. The green histogram represents the three-tracks case plotted w.r.t. the minimum electron angle [230].

In Fig. 5.3, the shape of the differential cross section of $\mu^+\,\mathrm{C} \to \mu^+\,\mathrm{C}\,e^+e^-$ w.r.t. the FS electron angle $\mathrm{d}\sigma/\,\mathrm{d}\vartheta_e$ is shown. In the case where two tracks are reconstructed in the detector, the cross section decreases as the electron angle increases. The cross section peaks at about 30 nb/mrad for $\vartheta_e \simeq 2$ mrad and slowly decreases, reaching about 10 nb/mrad at $\vartheta_e = 32$ mrad. In the case where three tracks are reconstructed in the detector the cross section plotted w.r.t. the maximum electron angle is very similar to the two-tracks case, but it is shifted upwards by some tens of nb/mrad, at most. The differential cross section plotted w.r.t. the minimum angle is quite different, peaking for small electron angles at about 10^2 nb/mrad and quickly decreasing as the electron angle increases.

In Fig. 5.4, the shape of the differential cross section of $\mu^+\,\mathrm{C} \to \mu^+\,\mathrm{C}\,\ell^+\ell^-$ w.r.t. the FS muon angle $\mathrm{d}\sigma/\,\mathrm{d}\vartheta_\mu$ is shown. In the case with

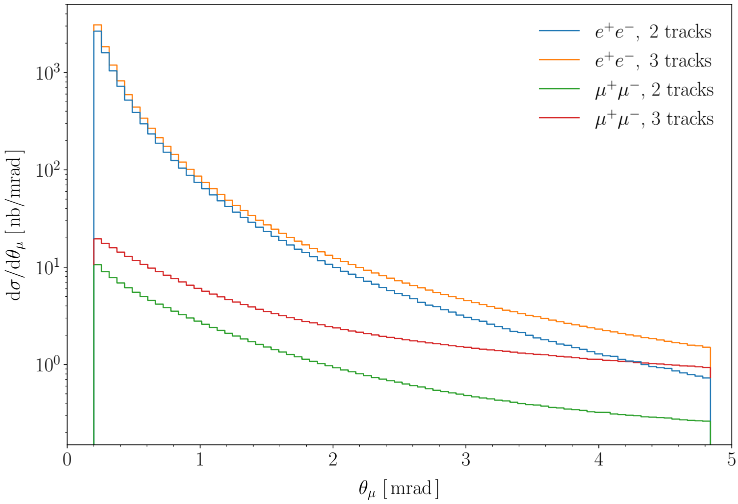

Figure 5.4: Differential cross section or the $\mu^+\,\mathrm{C} \to \mu^+\,\mathrm{C}\,e^+e^-$ process w.r.t. the muon scattering angle ϑ_μ. In this plot, the BAC have been imposed. The blue histogram represents the two-tracks case where $\ell = e$. The orange histogram represents the three-tracks case where $\ell = e$. The green histogram represents the two-tracks case where $\ell = \mu$. The red histogram represents the three-tracks case where $\ell = \mu$ [230].

$\ell = e$ and with two reconstructed tracks, the cross section peaks at $\vartheta_\mu = 0.2$ mrad and yields about 3×10^3 nb/mrad, decreasing rapidly as ϑ_μ increases. It reaches about 0.8 nb/mrad at the kinematical limit. The shape of the e^+e^- production in the three-tracks case is very similar. The muon pair production contributions are way less important for all the muon angles. They weigh at least two orders of magnitude less than the electron pair contributions. If two tracks are reconstructed, the peak at small ϑ_μ yields about 10 nb/mrad and decreases for increasing FS muon angles. The same behaviour is seen in the three-tracks case.

In Fig. 5.5, the effect of the nuclear form factor is shown for $\mu^+\,\mathrm{C} \to \mu^+\,\mathrm{C}\,e^+e^-$ and in the case of the $d\sigma/\,d\vartheta_\mu$ differential distribution. The plot shows the events where exactly two tracks are reconstructed in acceptance. As can be seen in the lower panel, the relative effect between the inclusion

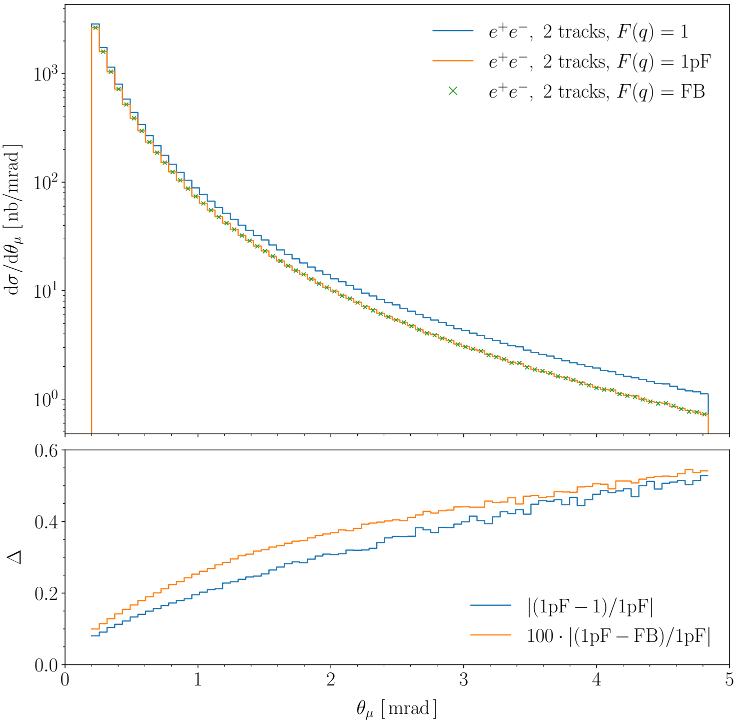

Figure 5.5: In the top plot, the differential cross section or the $\mu^+\,\mathrm{C} \to \mu^+\,\mathrm{C}\,e^+e^-$ process w.r.t. the muon scattering angle ϑ_μ is shown, with BAC. In blue, the two-tracks case where the nuclear form factor is not included. In orange, the two-tracks case where the nuclear form factor is parametrised by the 1pF model. In green, the two-tracks case where the nuclear form factor is parametrised by the FB expansion. In the bottom plot, the relative difference between the 1pF parametrisation and the case without form factor is in blue. The relative difference, times a factor of 100, between the 1pF model parametrisation and the FB expansion parametrisation is in orange [230].

of the 1pF parametrisation and not using the form factor is monotonically increasing as ϑ_μ increases. It goes from about 10 % for $\vartheta_\mu = 0.2$ mrad to about 55 % for $\vartheta_\mu = 4.84$ mrad. Moreover, the relative difference between

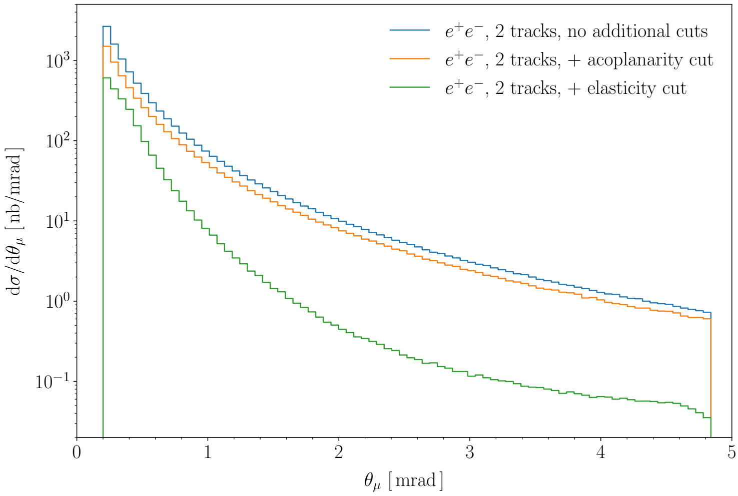

Figure 5.6: Differential cross section of the $\mu^+\,\mathrm{C} \to \mu^+\,\mathrm{C}\,e^+e^-$ process w.r.t. the muon scattering angle ϑ_μ. The blue histogram represents the two-tracks case where the BAC are imposed. The orange histogram represents the two-tracks case where the BAC and the acoplanarity cut are imposed. The green histogram represents the two-tracks case where all the cuts described in Sec. 5.2 are imposed [230].

the use of the 1pF model and the FB expansion parametrisation is lower than 0.6 % in the ϑ_μ space.

In Fig. 5.6, the shape of the differential cross section of $\mu^+\,\mathrm{C} \to \mu^+\,\mathrm{C}\,e^+e^-$ w.r.t. the FS muon angle $d\sigma/\,d\vartheta_\mu$ is shown. In this plot, the effect of the additional cuts can be seen in the case where two tracks are reconstructed in the detector. The additional cuts are the acoplanarity and elasticity selection criteria that were described in Sec. 5.2. In this plot, the effect of the form factor modelled as the 1pF parametrisation was included. The application of the acoplanarity cut reduces the contribution by a factor of about two in the whole ϑ_μ range. However, if one imposes an elasticity cut, the impact on the differential distribution is more important, namely of $\mathcal{O}(10)$ for $\vartheta_\mu \gtrsim 1$ mrad. For small muon angles, the peak of the distribution weighs about 5×10^2 nb/mrad, rapidly decreasing as ϑ_μ

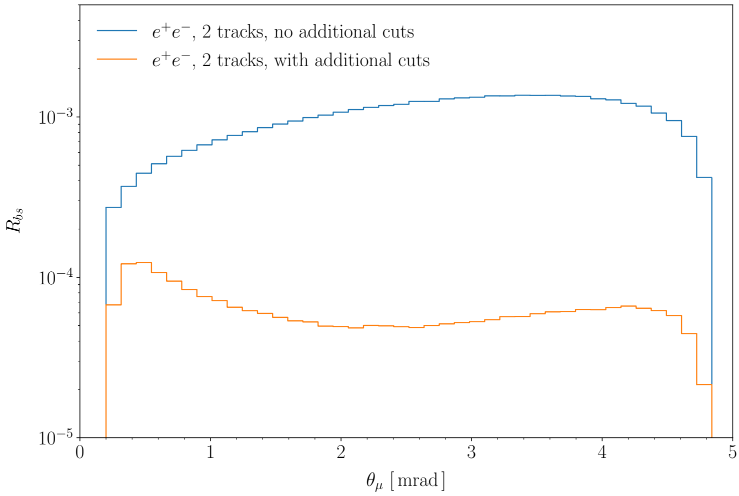

Figure 5.7: The differential background-to-signal ratio R_{bs} as defined in Eq. 5.14 is plotted w.r.t. the FS muon angle ϑ_μ. The blue histogram represents the two-tracks case where the BAC are imposed. The orange histogram represents the two-tracks case where all the cuts described in Sec. 5.2 are imposed [230].

increases.

In order to have an estimate of the impact of the $\mu^+\,\mathrm{C} \to \mu^+\,\mathrm{C}\,e^+e^-$ process on the MUonE differential observables, the background-to-signal ratio can be studied as a function of the muon scattering angle. It is defined as:

$$R_{\text{bs}} = \frac{\mathrm{d}\sigma(\mu^+ X \to \mu^+ X e^+ e^-; \vartheta_\mu)}{Z \times \mathrm{d}\sigma(\mu^+ e^- \to \mu^+ e^-; \vartheta_\mu)}, \tag{5.14}$$

where the $\mu e \to \mu e$ process is calculated with MESMER including all the corrections up to NNLO.

In Fig. 5.7, the differential background-to-signal ratio is shown, for the e^+e^- production. If only the BAC are included, the ratio ranges from some 10^{-4} to about 0.1 %. If one introduces all the cuts that were described in Sec. 5.2, the ratio is reduced to about 10^{-4} in all the ϑ_μ space. If one considers an uncertainty of about 10 % on the form factor, this means that a background subtraction procedure with a total uncertainty that is below 10 ppm is feasible. However, given the possible enhancements of radiative corrections in the small angles region, the calculation of the NLO corrections to the real pair production could be necessary for the final analysis of the MUonE data.

CONCLUSIONS AND OUTLOOK

In this thesis, the state of the art of the precision theory for muon-electron scattering has been presented. This work is framed within the precision studies of the muon anomalous magnetic moment, as a test of the Standard Model.

A major source of uncertainty in the theoretical predictions of the muon anomalous magnetic moment comes from hadronic effects. More specifically, within all the hadronic corrections, the Hadronic Leading Order term a_μ^{HLO} has the largest theoretical error. Given the very complex scenario of discrepancies between the Standard Model theoretical prediction, the lattice-QCD-based theoretical prediction and the experimentally measured values of a_μ, a novel approach to calculate a_μ^{HLO} based on a *spacelike* process has been proposed. This method is based on the measurement of the hadronic running of the electromagnetic constant $\Delta\alpha_{\mathrm{had}}(t)$ in a muon-electron scattering experiment, called MUonE.

MUonE requires a very high precision, at the level of about 10 parts per million on the differential cross section, to match the *timelike* and lattice QCD relative accuracy of about 0.4 parts per million. To reach this high level of precision, all the radiative corrections up to at least Next-to-Next-to-Leading Order have to be calculated. Such corrections were implemented into the MESMER Monte Carlo event generator, which is the main simulation tool for phenomenological studies as well as for data analysis and validation for the MUonE experiment.

The calculation of the NNLO lepton pair corrections has been performed. The impact of the virtual corrections weigh some 10^{-4} with respect to the LO at the differential level, with enhancements in some kinematic regions of the Phase Space, especially for small electron scattering angles ϑ_e. The real lepton pair production from muon-electron scattering, namely the $\mu e \to \mu e \ell^+ \ell^-$ process, was studied as a possible source of background for the MUonE experiment. As a matter of fact, when only two tracks are reconstructed into acceptance, this process could precisely mimic the elastic μe scattering signal. However, with the imposition of elasticity and acoplanarity cuts, the impact of the real lepton pair production becomes negligible with respect to the 10 ppm precision goal.

Another possible source of background at the MUonE experiment could be the single neutral pion production, namely $\mu e \to \mu e \pi^0$. Since the neutral pion most of the times decays into two photons the reconstructed track in the detector of this process could be mistaken for the one of elastic μe scattering. However, it was shown that this contribution is negligible both at integrated and at differential level, weighing some 10^{-7} on the differential observables with respect to the Leading Order.

Finally, the lepton pair production from muon-nucleus scattering $\mu X \to \mu X \ell^+ \ell^-$ was investigated, as a source of background for the MUonE experiment. This process, as was the case for the real lepton pair production from μe scattering, could mimic the elastic muon-electron scattering signal when only two tracks are reconstructed into acceptance. For this reason, a detailed study was necessary. Moreover, previous calculations with the Geant4 simulation toolkit hinted that the contribution of this process would be of about 10^{-4} with respect to the Leading Order, which is larger than the 10 ppm precision goal for MUonE. A differential calculation proved that indeed this process can be important in certain kinematic regions, especially in the MUonE normalisation region.

The work presented in this thesis does not conclude the list of the needed calculations for the MUonE experiment. As was shown for the NNLO contributions, radiative corrections can enhance the cross sections at very small scattering angles, making them larger than the MC theoretical error goal of 10 ppm on the differential observables. A very important missing block is the resummation of the large collinear logarithms that are due to radiative corrections. They enhance the cross sections in certain kinematic regions of the phase space, especially for small electron scattering angles. The resummation procedure could be included in the MC calculation with the implementation of a QED parton shower on top of the fixed-order calculation. The precision goal on the Monte Carlo generator will most probably be reached with the calculation of NNLO effects matched to a parton shower that includes all the Leading Logarithms.

Moreover, considering the importance of the tree-level lepton pair production from muon-nucleus scattering as a background for the MUonE experiment, the calculation of the radiative corrections to the tree-level approximation should be performed. It is expected that these corrections have non-negligible effects on the shape of the distributions with enhancements in particular kinematic regions.

Appendix A

THE MESMER MONTE CARLO EVENT GENERATOR

MESMER (Muon Electron Scattering with Multiple Electromagnetic Radiation)[1] is a MC event generator for high-precision simulation of muon-electron scattering at low energies. It was specifically developed to be the main simulation tool for the MUonE experiment. Its purpose is to provide the muon-electron scattering events with all the relative higher-order corrections that will be needed for the MUonE data analysis and detector simulation. In addition to this, the main background processes

---

[1] An up-to-date version of MESMER can be found at `https://github.com/cm-cc/mesmer`.

for the MUonE experiment can be calculated.

With the MESMER code, one can calculate the following corrections to μe scattering and background processes:

- LO QED [205];
- NLO EW corrections, for a single real or virtual photon [205];
- NNLO QED photonic corrections, where a subset of the corrections are approximated as explained in Sec. 4.3.1.1 [211];
- NNLO lepton pair contributions and $\mu e \to \mu e \ell^+ \ell^-$, with $\ell = e$, μ as explained in Sec. 4.3.2 [213];
- Single neutral pion production, $\mu e \to \mu e \pi^0$ as explained in Sec. 4.3.3 [228];
- Real pair production from muon-nucleus scattering, namely $\mu X \to \mu X \ell^+ \ell^-$, with $\ell = e$, μ as explained in Chapter 5 [230].

MESMER is a code that is mostly written in `Fortran 77`. Some external libraries are used to calculate one-loop integrals and pseudo-random number generation, such as LoopTools [236, 237], Collier [238] and the implementation in `C` of Ranlux. Moreover, MESMER includes three different parametrisations for the HVP function, by Jegerlehner[2], KNT[3] and by Ignatov[4].

The code can be built using a `Makefile`, provided that `cmake` is installed. The `make` command builds the executable `mesmer` and the needed libraries in `libmesmerfull.a`. After the compilation, the MESMER code can run in two separate modes:

- In standalone mode, with the command `./mesmer < input`;
- in embedded mode with wrappers of an external `C` or `C++` code, with `gcc file.c -L- -lmesmerfull -lm -lgfortran -o -executable.exe`.

The input data card contains all the possible values that define the different MESMER run modes. A list of the possible input parameters that can be specified in the data card can be seen by calling `help` in the MESMER interactive prompt. Otherwise, the MESMER `README` file has a comprehensive list. On top of the input parameters, it is possible to change

---

[2] http://www-com.physik.hu-berlin.de/~fjeger/software.html

[3] Available upon request from the authors.

[4] http://cmd.inp.nsk.su/~ignatov/vpl/

the event selection criteria in the file `cuts.F`. Moreover, a generic incoming muon momentum can be fed in input, event by event. This can be done for more realistic simulations where a beam profile is needed.

The output of the MC generator is stored in the directory that was indicated in the input data card. MESMER can save a `.txt` file with the integrated cross sections, several differential observables and also the generated events.

The MESMER code can provide events that are both weighted and unweighted. In the former case, each event comes with a different weight which has to be carried throughout the whole detector simulation and analysis. This procedure allows for a very fast generation and better MC error convergence. Moreover, the reweighting procedure is easier to perform.

On the other hand, in the case of unweighted generation all events come with the same weight. Thus, they are distributed according to the cross section. However, this procedure can be slow due to the unweighting procedure and can be affected by a bias since it can be difficult to guess a correct maximising value for weights before the generation.

The reweighting procedure allows to calculate in the same MC run different contributions. This technique allows to compute different reweighting coefficients r_i to include or exclude different effects, such as VP or different HVP parametrisation choices or different perturbative orders. When calculating a cross section, one can write it as:

$$\sigma = \sum_{i=0}^{n} \frac{w_i}{n}. \tag{A.1}$$

By allowing the reweighting procedure, the reweighting coefficients r_i can be calculated, such that the *new* cross section which includes different effects can be easily calculated as:

$$\sigma^{\mathrm{new}} = \sum_{i=0}^{n} \frac{w_i r_i}{n}, \tag{A.2}$$

where $r_i = w_i^{\mathrm{rew}}/w_i$.

The main advantage of this procedure is that it is not needed to regenerate another MC sample to account for the inclusion of different physics effects. On top of this, since the MC sample is the same, one can exploit the statistical correlation on the weights to reduce MC statistical errors. This procedure is widely used in the template fit procedure as shown in Sec. 3.2.

BIBLIOGRAPHY

[1] W. GERLACH AND O. STERN, *Experimental proof of the magnetic moment of the silver atom*, Z. Phys., 8 (1922), pp. 110–111.

[2] S. A. GOUDSMIT AND G. H. UHLENBECK, *Spinning electrons and the structure of spectra*, Nature, 117 (1926), pp. 264–265.

[3] P. A. M. DIRAC, *The quantum theory of the electron*, Proc. Roy. Soc. Lond. A, 117 (1928), pp. 610–624.

[4] J. S. SCHWINGER, *On Quantum electrodynamics and the magnetic moment of the electron*, Phys. Rev., 73 (1948), pp. 416–417.

[5] P. KUSCH AND H. M. FOLEY, *The magnetic moment of the electron*, Phys. Rev., 74 (1948), pp. 250–263.

[6] D. P. AGUILLARD ET AL., *Measurement of the Positive Muon Anomalous Magnetic Moment to* 0.20 *ppm*, Phys. Rev. Lett., (2023).

[7] G. W. BENNETT ET AL., *Final Report of the Muon E821 Anomalous Magnetic Moment Measurement at BNL*, Phys. Rev. D, 73 (2006), p. 072003.

[8] B. ABI ET AL., *Measurement of the Positive Muon Anomalous Magnetic Moment to* 0.46 *ppm*, Phys. Rev. Lett., 126 (2021), p. 141801.

[9] G. CHARPAK ET AL., *Measurement of the anomalous magnetic moment of the muon*, Phys. Rev. Lett., 6 (1961), pp. 128–132.

[10] J. BAILEY ET AL., *Precise Measurement of the Anomalous Magnetic Moment of the Muon*, Nuovo Cim. A, 9 (1972), pp. 369–432.

[11] J. BAILEY ET AL., *Final Report on the CERN Muon Storage Ring Including the Anomalous Magnetic Moment and the Electric Dipole Moment of the Muon, and a Direct Test of Relativistic Time Dilation*, Nucl. Phys. B, 150 (1979), pp. 1–75.

[12] R. M. CAREY ET AL., *New measurement of the anomalous magnetic moment of the positive muon*, Phys. Rev. Lett., 82 (1999), pp. 1632–1635.

[13] H. N. BROWN ET AL., *Improved measurement of the positive muon anomalous magnetic moment*, Phys. Rev. D, 62 (2000), p. 091101.

[14] H. N. Brown et al., *Precise measurement of the positive muon anomalous magnetic moment*, Phys. Rev. Lett., 86 (2001), pp. 2227–2231.

[15] G. W. Bennett et al., *Measurement of the positive muon anomalous magnetic moment to* 0.7 *ppm*, Phys. Rev. Lett., 89 (2002), p. 101804. [Erratum: Phys.Rev.Lett. 89, 129903 (2002)].

[16] G. W. Bennett et al., *Measurement of the negative muon anomalous magnetic moment to* 0.7 *ppm*, Phys. Rev. Lett., 92 (2004), p. 161802.

[17] J. Bailey et al., *The Anomalous Magnetic Moment of Positive and Negative Muons*, Phys. Lett. B, 67 (1977), p. 225.

[18] J. Grange et al., *Muon $g-2$ Technical Design Report*, tech. rep., FNAL, 1 2015. arXiv 1501.06858.

[19] D. W. Hertzog, *Next Generation Muon $g-2$ Experiments*, EPJ Web Conf., 118 (2016), p. 01015.

[20] H. Iinuma, *New approach to the muon $g-2$ and EDM experiment at J-PARC*, J. Phys. Conf. Ser., 295 (2011), p. 012032.

[21] N. Saito, *A novel precision measurement of muon $g-2$ and EDM at J-PARC*, AIP Conf. Proc., 1467 (2012), pp. 45–56.

[22] T. Mibe, *Measurement of muon $g-2$ and EDM with an ultra-cold muon beam at J-PARC*, Nucl. Phys. B Proc. Suppl., 218 (2011), pp. 242–246.

[23] F. Jegerlehner, *The Anomalous Magnetic Moment of the Muon*, vol. 274, Springer, Cham, 2017.

[24] T. Aoyama et al., *The anomalous magnetic moment of the muon in the Standard Model*, Phys. Rept., 887 (2020), pp. 1–166.

[25] A. Petermann, *Fourth order magnetic moment of the electron*, Helv. Phys. Acta, 30 (1957), pp. 407–408.

[26] C. M. Sommerfield, *The magnetic moment of the electron*, Annals of Physics, 5 (1958), pp. 26–57.

[27] S. Laporta and E. Remiddi, *The Analytical value of the electron $g-2$ at order α^3 in QED*, Phys. Lett. B, 379 (1996), pp. 283–291.

[28] P. Cvitanovic and T. Kinoshita, *Sixth Order Magnetic Moment of the electron*, Phys. Rev. D, 10 (1974), p. 4007.

[29] M. J. Levine and J. Wright, *Anomalous magnetic moment of the electron*, Phys. Rev. D, 8 (1973), pp. 3171–3179.

[30] R. Carroll and Y. P. Yao, *α^3 contributions to the anomalous magnetic moment of an electron in the mass-operator formalism*, Phys. Lett. B, 48 (1974), pp. 125–127.

[31] T. Kinoshita, *New value of the α^3 electron anomalous magnetic moment*, Phys. Rev. Lett., 75 (1995), pp. 4728–4731.

[32] S. Laporta, *High-precision calculation of the 4-loop contribution to the electron $g-2$ in QED*, Phys. Lett. B, 772 (2017), pp. 232–238.

[33] T. Aoyama, M. Hayakawa, T. Kinoshita, and M. Nio, *Tenth-Order Electron Anomalous Magnetic Moment — Contribution of Diagrams without Closed Lepton Loops*, Phys. Rev. D, 91 (2015), p. 033006. [Erratum: Phys.Rev.D 96, 019901 (2017)].

[34] S. Volkov, *New method of computing the contributions of graphs without lepton loops to the electron anomalous magnetic moment in QED*, Phys. Rev. D, 96 (2017), p. 096018.

[35] S. Volkov, *Numerical calculation of high-order QED contributions to the electron anomalous magnetic moment*, Phys. Rev. D, 98 (2018), p. 076018.

[36] T. Aoyama, T. Kinoshita, and M. Nio, *Theory of the Anomalous Magnetic Moment of the Electron*, Atoms, 7 (2019), p. 28.

[37] H. Elend, *On the anomalous magnetic moment of the muon*, Physics Letters, 20 (1966), pp. 682–684.

[38] G. Li, R. Mendel, and M. A. Samuel, *Precise mass ratio dependence of fourth order lepton anomalous magnetic moments: The Effect of a new measurement of m_τ*, Phys. Rev. D, 47 (1993), pp. 1723–1725.

[39] M. Passera, *Precise mass-dependent QED contributions to leptonic $g-2$ at order α^2 and α^3*, Phys. Rev. D, 75 (2007), p. 013002.

[40] S. Laporta and E. Remiddi, *The Analytical value of the electron light-light graphs contribution to the muon $g-2$ in QED*, Phys. Lett. B, 301 (1993), pp. 440–446.

[41] S. Laporta, *The Analytical contribution of the sixth order graphs with vacuum polarization insertions to the muon $g-2$ in QED*, Nuovo Cim. A, 106 (1993), pp. 675–683.

[42] A. Czarnecki and M. Skrzypek, *The Muon anomalous magnetic moment in QED: Three loop electron and tau contributions*, Phys. Lett. B, 449 (1999), pp. 354–360.

[43] S. Friot, D. Greynat, and E. De Rafael, *Asymptotics of Feynman diagrams and the Mellin-Barnes representation*, Phys. Lett. B, 628 (2005), pp. 73–84.

[44] B. Ananthanarayan, S. Friot, and S. Ghosh, *Three-loop QED contributions to the $g-2$ of charged leptons with two internal fermion loops and a class of Kampé de Fériet series*, Phys. Rev. D, 101 (2020), p. 116008.

[45] T. Aoyama, M. Hayakawa, T. Kinoshita, and M. Nio, *Complete Tenth-Order QED Contribution to the Muon $g-2$*, Phys. Rev. Lett., 109 (2012), p. 111808.

[46] T. Kinoshita and M. Nio, *Improved α^4 term of the electron anomalous magnetic moment*, Phys. Rev. D, 73 (2006), p. 013003.

[47] S. Laporta, *The Analytical contribution of some eighth order graphs containing vacuum polarization insertions to the muon $g-2$ in QED*, Phys. Lett. B, 312 (1993), pp. 495–500.

[48] A. Kurz, T. Liu, P. Marquard, and M. Steinhauser, *Anomalous magnetic moment with heavy virtual leptons*, Nucl. Phys. B, 879 (2014), pp. 1–18.

[49] A. L. Kataev, *Analytical eighth-order light-by-light QED contributions from leptons with heavier masses to the anomalous magnetic moment of electron*, Phys. Rev. D, 86 (2012), p. 013010.

[50] T. Aoyama, M. Hayakawa, T. Kinoshita, and M. Nio, *Tenth-Order QED Contribution to the Lepton Anomalous Magnetic Moment – Sixth-Order Vertices Containing an Internal Light-by-Light-Scattering Subdiagram*, Phys. Rev. D, 85 (2012), p. 093013.

[51] R. H. Parker, C. Yu, W. Zhong, B. Estey, and H. Müller, *Measurement of the fine-structure constant as a test of the Standard Model*, Science, 360 (2018), p. 191.

[52] A. Czarnecki, W. J. Marciano, and A. Vainshtein, *Refinements in electroweak contributions to the muon anomalous magnetic moment*, Phys. Rev. D, 67 (2003), p. 073006. [Erratum: Phys.Rev.D 73, 119901 (2006)].

[53] C. Gnendiger, D. Stöckinger, and H. Stöckinger-Kim, *The electroweak contributions to $(g-2)_\mu$ after the Higgs boson mass measurement*, Phys. Rev. D, 88 (2013), p. 053005.

[54] F. Jegerlehner and A. Nyffeler, *The Muon $g-2$*, Phys. Rept., 477 (2009), pp. 1–110.

[55] S. J. Brodsky and E. De Rafael, *Suggested boson-lepton pair couplings and the anomalous magnetic moment of the muon*, Phys. Rev., 168 (1968), pp. 1620–1622.

[56] B. E. Lautrup and E. De Rafael, *Calculation of the sixth-order contribution from the fourth-order vacuum polarization to the difference of the anomalous magnetic moments of muon and electron*, Phys. Rev., 174 (1968), pp. 1835–1842.

[57] M. Benayoun, L. Delbuono, and F. Jegerlehner, *$BHLS_2$, a New Breaking of the HLS Model and its Phenomenology*, Eur. Phys. J. C, 80 (2020), p. 81. [Erratum: Eur.Phys.J.C 80, 244 (2020)].

[58] M. Davier, A. Hoecker, B. Malaescu, and Z. Zhang, *A new evaluation of the hadronic vacuum polarisation contributions to the muon anomalous magnetic moment and to $\alpha(m_Z^2)$*, Eur. Phys. J. C, 80 (2020), p. 241. [Erratum: Eur.Phys.J.C 80, 410 (2020)].

[59] A. Keshavarzi, D. Nomura, and T. Teubner, *$g-2$ of charged leptons, $\alpha(m_Z^2)$, and the hyperfine splitting of muonium*, Phys. Rev. D, 101 (2020), p. 014029.

[60] M. Davier, A. Hoecker, B. Malaescu, and Z. Zhang, *Reevaluation of the hadronic vacuum polarisation contributions to the Standard Model predictions of the muon $g-2$ and $\alpha(m_Z^2)$ using newest hadronic cross-section data*, Eur. Phys. J. C, 77 (2017), p. 827.

[61] A. Keshavarzi, D. Nomura, and T. Teubner, *Muon $g-2$ and $\alpha(m_Z^2)$: a new data-based analysis*, Phys. Rev. D, 97 (2018), p. 114025.

[62] G. Colangelo, M. Hoferichter, and P. Stoffer, *Two-pion contribution to hadronic vacuum polarization*, JHEP, 02 (2019), p. 006.

[63] M. Hoferichter, B.-L. Hoid, and B. Kubis, *Three-pion contribution to hadronic vacuum polarization*, JHEP, 08 (2019), p. 137.

[64] K. Hagiwara, R. Liao, A. D. Martin, D. Nomura, and T. Teubner, *$(g-2)_\mu$ and $\alpha(m_Z^2)$ re-evaluated using new precise data*, J. Phys. G, 38 (2011), p. 085003.

[65] R. Alemany, M. Davier, and A. Hocker, *Improved determination of the hadronic contribution to the muon $g-2$ and to $\alpha(M_Z)$ using new data from hadronic τ decays*, Eur. Phys. J. C, 2 (1998), pp. 123–135.

[66] S. Narison, *Muon and τ anomalies updated*, Phys. Lett. B, 513 (2001), pp. 53–70. [Erratum: Phys.Lett.B 526, 414–415 (2002)].

[67] V. Cirigliano, G. Ecker, and H. Neufeld, *Radiative τ decay and the magnetic moment of the muon*, JHEP, 08 (2002), p. 002.

[68] K. Maltman and C. E. Wolfe, *Isospin breaking in the relation between the $\tau^- \to \nu_\tau \pi^- \pi^0$ and $e^+e^- \to \pi^+\pi^-$ versions of $|F_\pi(s)|^2$ and implications for $(g-2)_\mu$*, Phys. Rev. D, 73 (2006), p. 013004.

[69] K. Maltman, *Constraints on the $I = 1$ hadronic τ decay and $e^+e^- \to$ hadrons data sets and implications for $(g-2)_\mu$*, Phys. Lett. B, 633 (2006), pp. 512–518.

[70] M. Davier, A. Hoecker, B. Malaescu, and Z. Zhang, *Reevaluation of the Hadronic Contributions to the Muon $g-2$ and to $\alpha(m_Z)$*, Eur. Phys. J. C, 71 (2011), p. 1515. [Erratum: Eur.Phys.J.C 72, 1874 (2012)].

[71] M. Benayoun, P. David, L. DelBuono, and F. Jegerlehner, *Upgraded Breaking Of The HLS Model: A Full Solution to the $\tau^- e^+ e^-$ and ϕ Decay Issues And Its Consequences On $g-2$ VMD Estimates*, Eur. Phys. J. C, 72 (2012), p. 1848.

[72] M. Davier, A. Höcker, B. Malaescu, C.-Z. Yuan, and Z. Zhang, *Update of the ALEPH non-strange spectral functions from hadronic τ decays*, Eur. Phys. J. C, 74 (2014), p. 2803.

[73] S. Narison, *QCD parameters and SM-high precisions from $e^+e^-$to*hadrons, Nucl. Phys. A, 1039 (2023), p. 122744.

[74] L. Esparza-Arellano, A. Rojas, and G. Toledo, *Sizing the double pole resonant enhancement in $e^+e^- \to \pi^0\pi^0\gamma$ cross section and $\tau^- \to \pi^-\pi^0\nu_\tau\gamma$ decay.* arXiv 2308.02766, 8 2023.

[75] J. A. Miranda and P. Roig, *New τ-based evaluation of the hadronic contribution to the vacuum polarization piece of the muon anomalous magnetic moment*, Phys. Rev. D, 102 (2020), p. 114017.

[76] R. Escribano, A. Miranda, and P. Roig, *Radiative corrections to the $\tau^- \to (P_1P_2)^-\nu_\tau$ ($P_{1,2} = \pi, K$) decays.* arXiv 2303.01362, 3 2023.

[77] P. Masjuan, A. Miranda, and P. Roig, *τ data-driven evaluation of Euclidean windows for the hadronic vacuum polarization.* arXiv 2305.20005, 5 2023.

[78] P. Masjuan, A. Miranda, and P. Roig, *Tau data-driven evaluation of the Hadronic Vacuum Polarization*, in 26th High-Energy Physics International Conference in QCD, 10 2023.

[79] J. Prades, E. de Rafael, and A. Vainshtein, *The Hadronic Light-by-Light Scattering Contribution to the Muon and Electron Anomalous Magnetic Moments*, Adv. Ser. Direct. High Energy Phys., 20 (2009), pp. 303–317.

[80] A. Nyffeler, *Hadronic light-by-light scattering in the muon $g-2$: A New short-distance constraint on pion-exchange*, Phys. Rev. D, 79 (2009), p. 073012.

[81] G. Colangelo, M. Hoferichter, M. Procura, and P. Stoffer, *Dispersion relation for hadronic light-by-light scattering: theoretical foundations*, JHEP, 09 (2015), p. 074.

[82] G. Colangelo, M. Hoferichter, M. Procura, and P. Stoffer, *Dispersive approach to hadronic light-by-light scattering*, JHEP, 09 (2014), p. 091.

[83] D. Giusti, F. Sanfilippo, and S. Simula, *Light-quark contribution to the leading hadronic vacuum polarization term of the muon $g-2$ from twisted-mass fermions*, Phys. Rev. D, 98 (2018), p. 114504.

[84] D. Giusti and S. Simula, *Lepton anomalous magnetic moments in Lattice QCD+QED*, PoS, LATTICE2019 (2019), p. 104.

[85] C. T. H. Davies et al., *Hadronic-vacuum-polarization contribution to the muon's anomalous magnetic moment from four-flavor lattice QCD*, Phys. Rev. D, 101 (2020), p. 034512.

[86] S. Borsanyi et al., *Hadronic vacuum polarization contribution to the anomalous magnetic moments of leptons from first principles*, Phys. Rev. Lett., 121 (2018), p. 022002.

[87] B. Chakraborty, C. T. H. Davies, P. G. de Oliviera, J. Koponen, G. P. Lepage, and R. S. Van de Water, *The hadronic vacuum polarization contribution to a_μ from full lattice QCD*, Phys. Rev. D, 96 (2017), p. 034516.

[88] F. Burger, X. Feng, G. Hotzel, K. Jansen, M. Petschlies, and D. B. Renner, *Four-Flavour Leading-Order Hadronic Contribution To The Muon Anomalous Magnetic Moment*, JHEP, 02 (2014), p. 099.

[89] A. Gérardin, M. Cè, G. von Hippel, B. Hörz, H. B. Meyer, D. Mohler, K. Ottnad, J. Wilhelm, and H. Wittig, *The leading hadronic contribution to $(g-2)_\mu$ from lattice QCD with $N_\mathrm{f} = 2+1$ flavours of O(a) improved Wilson quarks*, Phys. Rev. D, 100 (2019), p. 014510.

[90] E. Shintani and Y. Kuramashi, *Hadronic vacuum polarization contribution to the muon $g-2$ with 2+1 flavor lattice QCD on a larger than (10 fm)^4 lattice at the physical point*, Phys. Rev. D, 100 (2019), p. 034517.

[91] T. Blum, P. A. Boyle, V. Gülpers, T. Izubuchi, L. Jin, C. Jung, A. Jüttner, C. Lehner, A. Portelli, and J. T. Tsang, *Calculation of the hadronic vacuum polarization contribution to the muon anomalous magnetic moment*, Phys. Rev. Lett., 121 (2018), p. 022003.

[92] M. Della Morte, A. Francis, V. Gülpers, G. Herdoíza, G. von Hippel, H. Horch, B. Jäger, H. B. Meyer, A. Nyffeler, and H. Wittig, *The hadronic vacuum polarization contribution to the muon $g-2$ from lattice QCD*, JHEP, 10 (2017), p. 020.

[93] S. Borsanyi et al., *Leading hadronic contribution to the muon magnetic moment from lattice QCD*, Nature, 593 (2021), pp. 51–55.

[94] C. Lehner and A. S. Meyer, *Consistency of hadronic vacuum polarization between lattice QCD and the R-ratio*, Phys. Rev. D, 101 (2020), p. 074515.

[95] G. Colangelo, M. Hoferichter, A. Nyffeler, M. Passera, and P. Stoffer, *Remarks on higher-order hadronic corrections to the muon $g-2$*, Phys. Lett. B, 735 (2014), pp. 90–91.

[96] G. Colangelo et al., *Prospects for precise predictions of a_μ in the Standard Model.* arXiv 2203.15810, 3 2022.

[97] T. Blum, N. Christ, M. Hayakawa, T. Izubuchi, L. Jin, C. Jung, and C. Lehner, *Hadronic Light-by-Light Scattering Contribution to the Muon Anomalous Magnetic Moment from Lattice QCD*, Phys. Rev. Lett., 124 (2020), p. 132002.

[98] T. Blum, N. Christ, M. Hayakawa, T. Izubuchi, L. Jin, C. Jung, and C. Lehner, *Connected and Leading Disconnected Hadronic Light-by-Light Contribution to the Muon Anomalous Magnetic Moment with a Physical Pion Mass*, Phys. Rev. Lett., 118 (2017), p. 022005.

[99] E.-H. Chao, R. J. Hudspith, A. Gérardin, J. R. Green, H. B. Meyer, and K. Ottnad, *Hadronic light-by-light contribution to $(g-2)_\mu$ from lattice QCD: a complete calculation*, Eur. Phys. J. C, 81 (2021), p. 651.

[100] N. Asmussen, J. Green, H. B. Meyer, and A. Nyffeler, *Position-space approach to hadronic light-by-light scattering in the muon $g-2$ on the lattice*, PoS, LATTICE2016 (2016), p. 164.

[101] N. Asmussen, E.-H. Chao, A. Gérardin, J. R. Green, R. J. Hudspith, H. B. Meyer, and A. Nyffeler, *Developments in the position-space approach to the HLbL contribution to the muon $g-2$ on the lattice*, PoS, LATTICE2019 (2019), p. 195.

[102] E.-H. Chao, A. Gérardin, J. R. Green, R. J. Hudspith, and H. B. Meyer, *Hadronic light-by-light contribution to $(g-2)_\mu$ from lattice QCD with $SU(3)$ flavor symmetry*, Eur. Phys. J. C, 80 (2020), p. 869.

[103] T. Blum, N. Christ, M. Hayakawa, T. Izubuchi, L. Jin, C. Jung, and C. Lehner, *Using infinite volume, continuum QED and lattice QCD for the hadronic light-by-light contribution to the muon anomalous magnetic moment*, Phys. Rev. D, 96 (2017), p. 034515.

[104] F. V. Ignatov et al., *Measurement of the $e^+e^- \to \pi^+\pi^-$ cross section from threshold to 1.2 gev with the CMD-3 detector.* arXiv 2302.08834, 2 2023.

[105] F. V. Ignatov et al., *Measurement of the pion formfactor with CMD-3 detector and its implication to the hadronic contribution to muon $g-2$.* arXiv 2309.12910, 9 2023.

[106] A. Gurgone, *Theory for the muone experiment.* EPS-HEP2023 conference, 2023.

[107] C. Bouchiat and L. Michel, *La résonance dans la diffusion méson* π*— méson* π *et le moment magnétique anormal du méson* μ, J. Phys. Radium, 22 (1961), pp. 121–121.

[108] M. Gourdin and E. De Rafael, *Hadronic contributions to the muon g-factor*, Nucl. Phys. B, 10 (1969), pp. 667–674.

[109] R. R. Akhmetshin et al., *Reanalysis of hadronic cross-section measurements at CMD-2*, Phys. Lett. B, 578 (2004), pp. 285–289.

[110] V. M. Aul'chenko et al., *Measurement of the pion form-factor in the range 1.04-GeV to 1.38-GeV with the CMD-2 detector*, JETP Lett., 82 (2005), pp. 743–747.

[111] R. R. Akhmetshin et al., *High-statistics measurement of the pion form factor in the rho-meson energy range with the CMD-2 detector*, Phys. Lett. B, 648 (2007), pp. 28–38.

[112] R. R. Akhmetshin et al., *Measurement of* $e^+e^- \to \phi \to K^+K^-$ *cross section with the CMD-2 detector at VEPP-2M Collider*, Phys. Lett. B, 669 (2008), pp. 217–222.

[113] R. R. Akhmetshin et al., *Measurement of* ϕ *meson parameters in* K_L^0 K_S^0 *decay mode with CMD-2*, Phys. Lett. B, 466 (1999), p. 385. [Erratum: Phys.Lett.B 508, 217–218 (2001)].

[114] R. R. Akhmetshin et al., *Measurement of omega meson parameters in* $\pi^+\pi^-\pi^0$ *decay mode with CMD-2*, Phys. Lett. B, 476 (2000), pp. 33–39.

[115] R. R. Akhmetshin et al., *Study of the process* $e^+e^- \to \pi^+\pi^-\pi^+\pi^-\pi^0$ *with CMD-2 detector*, Phys. Lett. B, 489 (2000), pp. 125–130.

[116] R. R. Akhmetshin et al., *Total cross section of the process* $e^+e^- \to \pi^+\pi^-\pi^+\pi^-$ *in the C.M. energy range 980-MeV to 1380-MeV*, Phys. Lett. B, 595 (2004), pp. 101–108.

[117] R. R. Akhmetshin et al., *a(1)(1260)* π *dominance in the process* $e^+e^- \to 4\pi$ *at energies 1.05-GeV - 1.38- eV*, Phys. Lett. B, 466 (1999), pp. 392–402.

[118] M. N. Achasov et al., *Update of the* $e^+e^- \to \pi^+\pi^-$ *cross-section measured by SND detector in the energy region* $400\ MeV < \sqrt{s} < 1000\ MeV$, J. Exp. Theor. Phys., 103 (2006), pp. 380–384.

[119] M. N. Achasov et al., *Study of the reaction* $e^+e^- \to \pi^0\gamma$ *with the SND detector at the VEPP-2M collider*, Phys. Rev. D, 93 (2016), p. 092001.

[120] M. N. Achasov et al., *Measurement of the* $e^+e^- \to \pi^0\gamma$ *cross section in the energy range 1.075-2 GeV at SND*, Phys. Rev. D, 98 (2018), p. 112001.

[121] M. N. Achasov et al., *Measurements of the parameters of the* $\phi(1020)$ *resonance through studies of the processes* $e^+e^- \to K^+K^-$*,* K_SK_L*, and* $\pi^+\pi^-\pi^0$, Phys. Rev. D, 63 (2001), p. 072002.

[122] M. N. Achasov et al., *Measurement of the* $e^+e^- \to K^+K^-$ *process cross-section in the energy range* $\sqrt{s}$ *= 1.04 - 1.38 GeV with the SND detector in the experiment at VEPP-2M* e^+e^- *collider*, Phys. Rev. D, 76 (2007), p. 072012.

[123] M. N. Achasov et al., *Measurement of the* $e^+e^- \to K^+K^-$ *cross section in the energy range* $\sqrt{s} = 1.05 - 2.0$ *GeV*, Phys. Rev. D, 94 (2016), p. 112006.

[124] M. N. Achasov et al., *Study of the process* $e^+e^- \to n\bar{n}$ *at the VEPP-2000* e^+e^- *collider with the SND detector*, Phys. Rev. D, 90 (2014), p. 112007.

[125] M. N. Achasov et al., *Study of the process* $e^+e^- \to \pi^+\pi^-\pi^0$ *in the energy region* $\sqrt{s}$ *from 0.98-GeV to 1.38-GeV*, Phys. Rev. D, 66 (2002), p. 032001.

[126] M. N. Achasov et al., *Precise measurements of the hadronic cross sections with the CMD-3 and SND detectors at the VEPP-2000* e^+e^- *collider*, EPJ Web Conf., 71 (2014), p. 00121.

[127] V. M. Aulchenko et al., *Measurement of the* $e^+e^- \to \eta\pi^+\pi^-$ *cross section in the center-of-mass energy range 1.22-2.00 GeV with the SND detector at the VEPP-2000 collider*, Phys. Rev. D, 91 (2015), p. 052013.

[128] M. N. Achasov et al., *Measurement of the* $e^+e^- \to \eta\pi^+\pi^-$ *cross section with the SND detector at the VEPP-2000 collider*, Phys. Rev. D, 97 (2018), p. 012008.

[129] M. N. Achasov et al., *Analysis of* $e^+e^- \to \pi^+\pi^-\pi^+\pi^-$ *and* $e^+e^- \to \pi^+\pi^-\pi^0\pi^0$ *processes in the energy range of* $\sqrt{s}$ *= 0.98-1.38-GeV in experiments with a spherical neutral detector*, J. Exp. Theor. Phys., 96 (2003), pp. 789–800.

[130] E. A. Kozyrev et al., *Study of the process* $e^+e^- \to K^+K^-$ *in the center-of-mass energy range 1010–1060 MeV with the CMD-3 detector*, Phys. Lett. B, 779 (2018), pp. 64–71.

[131] R. R. Akhmetshin et al., *Study of the process* $e^+e^- \to p\bar{p}$ *in the c.m. energy range from threshold to 2 GeV with the CMD-3 detector*, Phys. Lett. B, 759 (2016), pp. 634–640.

[132] R. R. Akhmetshin et al., *Study of the process* $e^+e^- \to \pi^+\pi^-\pi^0\eta$ *in the c.m. energy range 1394-2005 MeV with the CMD-3 detector*, Phys. Lett. B, 773 (2017), pp. 150–158.

[133] R. R. Akhmetshin et al., *Study of the process* $e^+e^- \to \pi^+\pi^-\pi^+\pi^-$ *in the c.m. energy range 920-1060 MeV with the CMD-3 detector*, Phys. Lett. B, 768 (2017), pp. 345–350.

[134] R. R. Akhmetshin et al., *Study of the process* $e^+e^- \to 3(\pi^+\pi^-)$ *in the c.m.energy range 1.5–2.0 gev with the CMD-3 detector*, Phys. Lett. B, 723 (2013), pp. 82–89.

[135] S. S. Gribanov et al., *Measurement of the* $e^+e^- \to \eta\pi^+\pi^-$ *cross section with the CMD-3 detector at the VEPP-2000 collider*, JHEP, 01 (2020), p. 112.

[136] J. Z. Bai et al., *Measurement of the total cross-section for hadronic production by* e^+e^- *annihilation at energies between 2.6-GeV - 5-GeV*, Phys. Rev. Lett., 84 (2000), pp. 594–597.

[137] J. Z. Bai et al., *Measurements of the cross-section for $e^+e^- \to$ hadrons at center-of-mass energies from 2-GeV to 5-GeV*, Phys. Rev. Lett., 88 (2002), p. 101802.

[138] M. Ablikim et al., *R value measurements for e^+e^- annihilation at 2.60-GeV, 3.07-GeV and 3.65-GeV*, Phys. Lett. B, 677 (2009), pp. 239–245.

[139] V. V. Anashin et al., *Measurement of R_{uds} and R between 3.12 and 3.72 GeV at the KEDR detector*, Phys. Lett. B, 753 (2016), pp. 533–541.

[140] V. V. Anashin et al., *Precise measurement of R_{uds} and R between 1.84 and 3.72 GeV at the KEDR detector*, Phys. Lett. B, 788 (2019), pp. 42–51.

[141] S. Eidelman and F. Jegerlehner, *Hadronic contributions to $g-2$ of the leptons and to the effective fine structure constant $\alpha(m(Z)^2)$*, Z. Phys. C, 67 (1995), pp. 585–602.

[142] A. Aloisio et al., *Measurement of $\sigma(e^+e^- \to \pi^+\pi^-\gamma)$ and extraction of $\sigma(e^+e^- \to \pi^+\pi^-)$ below 1-GeV with the KLOE detector*, Phys. Lett. B, 606 (2005), pp. 12–24.

[143] F. Ambrosino et al., *Measurement of $\sigma(e^+e^- \to \pi^+\pi^-\gamma(\gamma)$ and the dipion contribution to the muon anomaly with the KLOE detector*, Phys. Lett. B, 670 (2009), pp. 285–291.

[144] F. Ambrosino et al., *Measurement of $\sigma(e^+e^- \to \pi^+\pi^-)$ from threshold to 0.85 GeV^2 using Initial State Radiation with the KLOE detector*, Phys. Lett. B, 700 (2011), pp. 102–110.

[145] D. Babusci et al., *Precision measurement of $\sigma(e^+e^- \to \pi^+\pi^-\gamma)/\sigma(e^+e^- \to \mu^+\mu^-\gamma)$ and determination of the $\pi^+\pi^-$ contribution to the muon anomaly with the KLOE detector*, Phys. Lett. B, 720 (2013), pp. 336–343.

[146] B. Aubert et al., *Precise measurement of the $e^+e^- \to \pi^+\pi^-(\gamma)$ cross section with the Initial State Radiation method at BABAR*, Phys. Rev. Lett., 103 (2009), p. 231801.

[147] J. P. Lees et al., *Precise Measurement of the $e^+e^- \to \pi^+\pi^-(\gamma)$ Cross Section with the Initial-State Radiation Method at BABAR*, Phys. Rev. D, 86 (2012), p. 032013.

[148] J. P. Lees et al., *Study of additional radiation in the initial-state-radiation processes $e^+e^- \to \mu^+\mu^-\gamma$ and $e^+e^- \to \pi^+\pi^-\gamma$ in the BABAR experiment.* arXiv 2308.05233, 8 2023.

[149] B. Aubert et al., *Study of $e^+e^- \to \pi^+\pi^-\pi^0$ process using initial state radiation with BaBar*, Phys. Rev. D, 70 (2004), p. 072004.

[150] B. Aubert et al., *The $e^+e^- \to \pi^+\pi^-\pi^+\pi^-$, $K^+K^-\pi^+\pi^-$, and $K^+K^-K^+K^-$ cross sections at center-of-mass energies 0.5-GeV - 4.5-GeV measured with initial-state radiation*, Phys. Rev. D, 71 (2005), p. 052001.

[151] B. Aubert et al., *A Study of $e^+e^- \to p\bar{p}$ using initial state radiation with BABAR*, Phys. Rev. D, 73 (2006), p. 012005.

[152] B. Aubert et al., *The* $e^+e^- \to 3(\pi^+\pi^-), 2(\pi^+\pi^-\pi^0)$ *and* $K^+K^-2(\pi^+\pi^-)$ *cross sections at center-of-mass energies from production threshold to 4.5-GeV measured with initial-state radiation*, Phys. Rev. D, 73 (2006), p. 052003.

[153] B. Aubert et al., *Measurements of* $e^+e^- \to K^+K^-\eta$*,* $K^+K^-\pi^0$ *and* $K^0_sK^\pm\pi^\mp$ *cross- sections using initial state radiation events*, Phys. Rev. D, 77 (2008), p. 092002.

[154] B. Aubert et al., *Study of* $e^+e^- \to \Lambda\bar{\Lambda}$*,* $\Lambda\bar{\Sigma}^0$*,* $\Sigma^0\bar{\Sigma}^0$ *using initial state radiation with BABAR*, Phys. Rev. D, 76 (2007), p. 092006.

[155] B. Aubert et al., *The* $e^+e^- \to K^+K^-\pi^+\pi^-$*,* $K^+K^-\pi^0\pi^0$ *and* $K^+K^-K^+K^-$ *cross sections measured with initial-state radiation*, Phys. Rev. D, 76 (2007), p. 012008.

[156] B. Aubert et al., *The* $e^+e^- \to 2(\pi^+\pi^-)\pi^0$*,* $2(\pi^+\pi^-)\eta$*,* $K^+K^-\pi^+\pi^-\pi^0$ *and* $K^+K^-\pi^+\pi^-\eta$ *Cross Sections Measured with Initial-State Radiation*, Phys. Rev. D, 76 (2007), p. 092005. [Erratum: Phys.Rev.D 77, 119902 (2008)].

[157] J. P. Lees et al., *Cross Sections for the Reactions* $e^+e^- \to K^+K^-\pi^+\pi^-$*,* $K^+K^-\pi^0\pi^0$*, and* $K^+K^-K^+K^-$ *Measured Using Initial-State Radiation Events*, Phys. Rev. D, 86 (2012), p. 012008.

[158] J. P. Lees et al., *Initial-State Radiation Measurement of the* $e^+e^- - > \pi^+\pi^-\pi^+\pi^-$ *Cross Section*, Phys. Rev. D, 85 (2012), p. 112009.

[159] J. P. Lees et al., *Measurement of the* $e^+e^- \to \pi^+\pi^-\pi^0\pi^0$ *cross section using initial-state radiation at BABAR*, Phys. Rev. D, 96 (2017), p. 092009.

[160] J. P. Lees et al., *Measurement of the* $e^+e^- \to p\bar{p}$ *cross section in the energy range from 3.0 to 6.5 GeV*, Phys. Rev. D, 88 (2013), p. 072009.

[161] J. P. Lees et al., *Study of* $e^+e^- \to p\bar{p}$ *via initial-state radiation at BABAR*, Phys. Rev. D, 87 (2013), p. 092005.

[162] M. Ablikim et al., *Measurement of the* $e^+e^- \to \pi^+\pi^-$ *cross section between 600 and 900 mev using initial state radiation*, Phys. Lett. B, 753 (2016), pp. 629–638. [Erratum: Phys.Lett.B 812, 135982 (2021)].

[163] T. Xiao, S. Dobbs, A. Tomaradze, K. K. Seth, and G. Bonvicini, *Precision Measurement of the Hadronic Contribution to the Muon Anomalous Magnetic Moment*, Phys. Rev. D, 97 (2018), p. 032012.

[164] A. B. Arbuzov, G. V. Fedotovich, F. V. Ignatov, E. A. Kuraev, and A. L. Sibidanov, *Monte-Carlo generator for e+e- annihilation into lepton and hadron pairs with precise radiative corrections*, Eur. Phys. J. C, 46 (2006), pp. 689–703.

[165] S. Jadach, W. Placzek, and B. F. L. Ward, *BHWIDE 1.00: O(α) YFS exponentiated Monte Carlo for Bhabha scattering at wide angles for LEP-1 / SLC and LEP-2*, Phys. Lett. B, 390 (1997), pp. 298–308.

[166] S. Jadach, B. F. L. Ward, and Z. Was, *The Precision Monte Carlo event generator K K for two fermion final states in* e^+e^- *collisions*, Comput. Phys. Commun., 130 (2000), pp. 260–325.

[167] G. Balossini, C. M. Carloni Calame, G. Montagna, O. Nicrosini, and F. Piccinini, *Matching perturbative and parton shower corrections to Bhabha process at flavour factories*, Nucl. Phys. B, 758 (2006), pp. 227–253.

[168] H. Czyz, A. Grzelinska, J. H. Kuhn, and G. Rodrigo, *The Radiative return at ϕ and B factories: FSR for muon pair production at next-to-leading order*, Eur. Phys. J. C, 39 (2005), pp. 411–420.

[169] H. Czyz, J. H. Kuhn, E. Nowak, and G. Rodrigo, *Nucleon form-factors, B meson factories and the radiative return*, Eur. Phys. J. C, 35 (2004), pp. 527–536.

[170] A. Anastasi et al., *Combination of KLOE $\sigma\big(e^+e^- \to \pi^+\pi^-\gamma(\gamma)\big)$ measurements and determination of $a_\mu^{\pi^+\pi^-}$ in the energy range $0.10 < s < 0.95$ GeV^2*, JHEP, 03 (2018), p. 173.

[171] B. e. Lautrup, A. Peterman, and E. de Rafael, *Recent developments in the comparison between theory and experiments in quantum electrodynamics*, Phys. Rept., 3 (1972), pp. 193–259.

[172] E. de Rafael, *Hadronic contributions to the muon $g - 2$ and low-energy QCD*, Phys. Lett. B, 322 (1994), pp. 239–246.

[173] T. Blum, *Lattice calculation of the lowest order hadronic contribution to the muon anomalous magnetic moment*, Phys. Rev. Lett., 91 (2003), p. 052001.

[174] M. Golterman, K. Maltman, and S. Peris, *New strategy for the lattice evaluation of the leading order hadronic contribution to $(g - 2)_\mu$*, Phys. Rev. D, 90 (2014), p. 074508.

[175] C. Aubin, T. Blum, M. Golterman, and S. Peris, *Model-independent parametrization of the hadronic vacuum polarization and $g - 2$ for the muon on the lattice*, Phys. Rev. D, 86 (2012), p. 054509.

[176] B. Chakraborty, C. T. H. Davies, G. C. Donald, R. J. Dowdall, J. Koponen, G. P. Lepage, and T. Teubner, *Strange and charm quark contributions to the anomalous magnetic moment of the muon*, Phys. Rev. D, 89 (2014), p. 114501.

[177] C. Aubin, T. Blum, C. Tu, M. Golterman, C. Jung, and S. Peris, *Light quark vacuum polarization at the physical point and contribution to the muon $g - 2$*, Phys. Rev. D, 101 (2020), p. 014503.

[178] D. Bernecker and H. B. Meyer, *Vector Correlators in Lattice QCD: Methods and applications*, Eur. Phys. J. A, 47 (2011), p. 148.

[179] M. Cè et al., *Window observable for the hadronic vacuum polarization contribution to the muon $g - 2$ from lattice QCD*, Phys. Rev. D, 106 (2022), p. 114502.

[180] C. Aubin, T. Blum, M. Golterman, and S. Peris, *Muon anomalous magnetic moment with staggered fermions: Is the lattice spacing small enough?*, Phys. Rev. D, 106 (2022), p. 054503.

[181] G. Wang, T. Draper, K.-F. Liu, and Y.-B. Yang, *Muon $g - 2$ with overlap valence fermions*, Phys. Rev. D, 107 (2023), p. 034513.

[182] D. Giusti and S. Simula, *Window contributions to the muon hadronic vacuum polarization with twisted-mass fermions*, PoS, LATTICE2021 (2022), p. 189.

[183] C. Alexandrou et al., *Lattice calculation of the short and intermediate time-distance hadronic vacuum polarization contributions to the muon magnetic moment using twisted-mass fermions*, Phys. Rev. D, 107 (2023), p. 074506.

[184] T. Blum et al., *Update of Euclidean windows of the hadronic vacuum polarization*, Phys. Rev. D, 108 (2023), p. 054507.

[185] G. Colangelo, A. X. El-Khadra, M. Hoferichter, A. Keshavarzi, C. Lehner, P. Stoffer, and T. Teubner, *Data-driven evaluations of Euclidean windows to scrutinize hadronic vacuum polarization*, Phys. Lett. B, 833 (2022), p. 137313.

[186] C. M. Carloni Calame, M. Passera, L. Trentadue, and G. Venanzoni, *A new approach to evaluate the leading hadronic corrections to the muon* $g-2$, Phys. Lett. B, 746 (2015), pp. 325–329.

[187] G. Abbiendi et al., *Measuring the leading hadronic contribution to the muon* $g-2$ *via* μe *scattering*, Eur. Phys. J. C, 77 (2017), p. 139.

[188] E. Balzani, S. Laporta, and M. Passera, *Hadronic vacuum polarization contributions to the muon* $g-2$ *in the space-like region*, Phys. Lett. B, 834 (2022), p. 137462.

[189] M. Steinhauser, *Leptonic contribution to the effective electromagnetic coupling constant up to three loops*, Phys. Lett. B, 429 (1998), pp. 158–161.

[190] C. Sturm, *Leptonic contributions to the effective electromagnetic coupling at four-loop order in QED*, Nucl. Phys. B, 874 (2013), pp. 698–719.

[191] G. Abbiendi et al., *Letter of Intent: the MUonE project.* Tech. rep. CERN-SPSC-2019-026. SPSC-I-25, 2019.

[192] R. Pilato, *Feasibility study of the MUonE experiment.* PhD Thesis, 2023.

[193] R. N. Pilato, *Status of the MUonE experiment*, PoS, ICHEP2022 (2022), p. 788.

[194] G. Ballerini et al., *A feasibility test run for the MUonE project*, Nucl. Instrum. Meth. A, 936 (2019), pp. 636–637.

[195] S. Actis et al., *Quest for precision in hadronic cross sections at low energy: Monte Carlo tools vs. experimental data*, Eur. Phys. J. C, 66 (2010), pp. 585–686.

[196] F. Ignatov, R. N. Pilato, T. Teubner, and G. Venanzoni, *An alternative evaluation of the leading-order hadronic contribution to the muon* $g-2$ *with MUonE*, Phys. Lett. B, 848 (2024), p. 138344.

[197] C. M. Carloni Calame, *Muone, current status and future.* Third Plenary Workshop of the Muon $g-2$ Theory Initiative, 2019.

[198] CMS Collaboration. `https://cms-analysis.github.io/HiggsAnalysis-CombinedLimit`.

[199] ATLAS, CMS and LHC Higgs Combination Groups, *Procedure for the LHC Higgs boson search combination in Summer 2011*. https://cds.cern.ch/record/1379837, 2011.

[200] G. Abbiendi et al., *Results on multiple Coulomb scattering from 12 and 20 GeV electrons on carbon targets*, JINST, 15 (2020), p. 01.

[201] G. Abbiendi, *Status of the MUonE experiment*, PoS, ICHEP2020 (2021), p. 223.

[202] G. Abbiendi, *Status of the MUonE experiment*, Phys. Scripta, 97 (2022), p. 054007.

[203] G. Abbiendi et al., *A study of muon-electron elastic scattering in a test beam*, JINST, 16 (2021), p. P06005.

[204] P. Banerjee et al., *Theory for muon-electron scattering @ 10 ppm: A report of the MUonE theory initiative*, Eur. Phys. J. C, 80 (2020), p. 591.

[205] M. Alacevich, C. M. Carloni Calame, M. Chiesa, G. Montagna, O. Nicrosini, and F. Piccinini, *Muon-electron scattering at NLO*, JHEP, 02 (2019), p. 155. [Erratum: JHEP 02, 201 (2022)].

[206] P. Banerjee, T. Engel, A. Signer, and Y. Ulrich, *QED at NNLO with McMule*, SciPost Phys., 9 (2020), p. 027.

[207] P. Mastrolia, M. Passera, A. Primo, and U. Schubert, *Master integrals for the NNLO virtual corrections to μe scattering in QED: the planar graphs*, JHEP, 11 (2017), p. 198.

[208] S. Di Vita, S. Laporta, P. Mastrolia, A. Primo, and U. Schubert, *Master integrals for the NNLO virtual corrections to μe scattering in QED: the non-planar graphs*, JHEP, 09 (2018), p. 016.

[209] T. Engel, C. Gnendiger, A. Signer, and Y. Ulrich, *Small-mass effects in heavy-to-light form factors*, JHEP, 02 (2019), p. 118.

[210] T. Engel, A. Signer, and Y. Ulrich, *A subtraction scheme for massive QED*, JHEP, 01 (2020), p. 085.

[211] C. M. Carloni Calame, M. Chiesa, S. M. Hasan, G. Montagna, O. Nicrosini, and F. Piccinini, *Towards muon-electron scattering at NNLO*, JHEP, 11 (2020), p. 028.

[212] D. R. Yennie, S. C. Frautschi, and H. Suura, *The infrared divergence phenomena and high-energy processes*, Annals Phys., 13 (1961), pp. 379–452.

[213] E. Budassi, C. M. Carloni Calame, M. Chiesa, C. L. Del Pio, S. M. Hasan, G. Montagna, O. Nicrosini, and F. Piccinini, *NNLO virtual and real leptonic corrections to muon-electron scattering*, JHEP, 11 (2021), p. 098.

[214] G. Abbiendi et al., *Mini-Proceedings of the STRONG2020 Virtual Workshop on "Space-like and Time-like determination of the Hadronic Leading Order contribution to the Muon $g-2$"*, in STRONG2020 Virtual Workshop "Space-like and Time-like determination of the Hadronic Leading Order contribution to the Muon $g-2$ ", 1 2022.

[215] E. Budassi and C. L. Del Pio, *High precision calculations for the MUonE experiment*, PoS, ICHEP2022 (2022), p. 796.

[216] R. Bonciani et al., *Two-Loop Four-Fermion Scattering Amplitude in QED*, Phys. Rev. Lett., 128 (2022), p. 022002.

[217] A. Broggio et al., *Muon-electron scattering at NNLO*, JHEP, 01 (2023), p. 112.

[218] M. Fael, *Hadronic corrections to μ-e scattering at NNLO with space-like data*, JHEP, 02 (2019), p. 027.

[219] M. Fael and M. Passera, *Muon-Electron Scattering at Next-To-Next-To-Leading Order: The Hadronic Corrections*, Phys. Rev. Lett., 122 (2019), p. 192001.

[220] T. Ahmed, G. Crisanti, F. Gasparotto, S. M. Hasan, and P. Mastrolia, *Two-loop vertices with vacuum polarization insertion*, JHEP, 01 (2024), p. 010.

[221] P. S. B. Dev, W. Rodejohann, X.-J. Xu, and Y. Zhang, *MUonE sensitivity to new physics explanations of the muon anomalous magnetic moment*, JHEP, 05 (2020), p. 053.

[222] A. Masiero, P. Paradisi, and M. Passera, *New physics at the MUonE experiment at CERN*, Phys. Rev. D, 102 (2020), p. 075013.

[223] M. Fael, F. Lange, K. Schönwald, and M. Steinhauser, *Singlet and nonsinglet three-loop massive form factors*, Phys. Rev. D, 106 (2022), p. 034029.

[224] M. Fael, F. Lange, K. Schönwald, and M. Steinhauser, *Massive Vector Form Factors to Three Loops*, Phys. Rev. Lett., 128 (2022), p. 172003.

[225] M. Fael, F. Lange, K. Schönwald, and M. Steinhauser, *Massive three-loop form factors: Anomaly contribution*, Phys. Rev. D, 107 (2023), p. 094017.

[226] S. Badger, J. Kryś, R. Moodie, and S. Zoia, *Lepton-pair scattering with an off-shell and an on-shell photon at two loops in massless QED*, JHEP, 11 (2023), p. 041.

[227] Y. Ulrich, *N^3LO kick-off workstop/thinkstart*, 2022.

[228] E. Budassi, C. M. Carloni Calame, C. L. Del Pio, and F. Piccinini, *Single π^0 production in μe scattering at MUonE*, Phys. Lett. B, 829 (2022), p. 137138.

[229] C. L. Del Pio and E. Budassi, *Neutral pion production in μe scattering at MUonE*, PoS, ICHEP2022 (2022), p. 1035.

[230] G. Abbiendi, E. Budassi, C. M. Carloni Calame, A. Gurgone, and F. Piccinini, *Lepton pair production in muon-nucleus scattering*, (2024). arXiv 2401.06077.

[231] A. Gurgone, *Theory for the MUonE experiment*, 1 2024.

[232] R. Plestid and M. B. Wise, *Atomic binding corrections for high energy fixed target experiments*, (2024).

[233] J. A. M. Vermaseren, *New features of FORM*. arXiv math-ph/0010025, 2000.

[234] J. Kuipers, T. Ueda, J. A. M. Vermaseren, and J. Vollinga, *FORM version 4.0*, Comput. Phys. Commun., 184 (2013), pp. 1453–1467.

[235] B. Ruijl, T. Ueda, and J. Vermaseren, *FORM version 4.2*. arXiv 1707.06453, 2017.

[236] T. Hahn and M. Perez-Victoria, *Automatized one loop calculations in four-dimensions and D-dimensions*, Comput. Phys. Commun., 118 (1999), pp. 153–165.

[237] T. Hahn, *Feynman Diagram Calculations with FeynArts, FormCalc, and Loop-Tools*, PoS, ACAT2010 (2010), p. 078.

[238] A. Denner, S. Dittmaier, and L. Hofer, *Collier: a fortran-based Complex One-Loop LIbrary in Extended Regularizations*, Comput. Phys. Commun., 212 (2017), pp. 220–238.

[239] S. Actis, A. Denner, L. Hofer, J.-N. Lang, A. Scharf, and S. Uccirati, *RECOLA: REcursive Computation of One-Loop Amplitudes*, Comput. Phys. Commun., 214 (2017), pp. 140–173.

[240] W. Bernreuther, R. Bonciani, T. Gehrmann, R. Heinesch, T. Leineweber, P. Mastrolia, and E. Remiddi, *Two-loop QCD corrections to the heavy quark form-factors: The Vector contributions*, Nucl. Phys. B, 706 (2005), pp. 245–324.

[241] P. Mastrolia and E. Remiddi, *Two loop form-factors in QED*, Nucl. Phys. B, 664 (2003), pp. 341–356.

[242] C. Carloni Calame, H. Czyz, J. Gluza, M. Gunia, G. Montagna, O. Nicrosini, F. Piccinini, T. Riemann, and M. Worek, *NNLO leptonic and hadronic corrections to Bhabha scattering and luminosity monitoring at meson factories*, JHEP, 07 (2011), p. 126.

[243] S. Jadach, M. Skrzypek, and B. F. L. Ward, *Analytical results for low angle Bhabha scattering with pair production*, Phys. Rev. D, 47 (1993), pp. 3733–3741.

[244] S. Jadach, M. Skrzypek, and B. F. L. Ward, *Soft pairs real and virtual infrared functions in QED*, Phys. Rev. D, 49 (1994), pp. 1178–1182.

[245] S. Jadach, M. Skrzypek, and B. F. L. Ward, *Soft pairs corrections to low angle Bhabha scattering: YFS Monte Carlo approach*, Phys. Rev. D, 55 (1997), pp. 1206–1215.

[246] A. B. Arbuzov, E. A. Kuraev, N. P. Merenkov, and L. Trentadue, *Pair production in small angle Bhabha scattering*, J. Exp. Theor. Phys., 81 (1995), pp. 638–646.

[247] A. B. Arbuzov, E. A. Kuraev, N. P. Merenkov, and L. Trentadue, *Virtual and soft real pair production in large angle Bhabha scattering*, Phys. Atom. Nucl., 60 (1997), pp. 591–600.

[248] G. Montagna, M. Moretti, O. Nicrosini, A. Pallavicini, and F. Piccinini, *Light pair correction to Bhabha scattering at small angle*, Nucl. Phys. B, 547 (1999), pp. 39–59.

[249] G. Montagna, M. Moretti, O. Nicrosini, A. Pallavicini, and F. Piccinini, *Light pair corrections to small angle Bhabha scattering in a realistic set up at LEP*, Phys. Lett. B, 459 (1999), pp. 649–652.

[250] S. Actis, M. Czakon, J. Gluza, and T. Riemann, *Virtual hadronic and leptonic contributions to Bhabha scattering*, Phys. Rev. Lett., 100 (2008), p. 131602.

[251] J. H. Kuhn and S. Uccirati, *Two-loop QED hadronic corrections to Bhabha scattering*, Nucl. Phys. B, 806 (2009), pp. 300–326.

[252] A. H. Hoang, J. H. Kuhn, and T. Teubner, *Radiation of light fermions in heavy fermion production*, Nucl. Phys. B, 452 (1995), pp. 173–187.

[253] R. Barbieri, J. A. Mignaco, and E. Remiddi, *Electron form-factors up to fourth order. 1.*, Nuovo Cim. A, 11 (1972), pp. 824–864.

[254] R. Barbieri, J. A. Mignaco, and E. Remiddi, *Electron form factors up to fourth order. 2.*, Nuovo Cim. A, 11 (1972), pp. 865–916.

[255] F. A. Berends, R. Pittau, and R. Kleiss, *All electroweak four fermion processes in electron - positron collisions*, Nucl. Phys. B, 424 (1994), pp. 308–342.

[256] B. P. Kersevan and E. Richter-Was, *Improved phase space treatment of massive multi-particle final states*, Eur. Phys. J. C, 39 (2005), pp. 439–450.

[257] R. Bonciani, A. Ferroglia, P. Mastrolia, E. Remiddi, and J. J. van der Bij, *Two-loop $N(F) = 1$ QED Bhabha scattering differential cross section*, Nucl. Phys. B, 701 (2004), pp. 121–179.

[258] S. J. Brodsky, T. Kinoshita, and H. Terazawa, *Two Photon Mechanism of Particle Production by High-Energy Colliding Beams*, Phys. Rev. D, 4 (1971), pp. 1532–1557.

[259] C. Patrignani et al., *Review of Particle Physics*, Chin. Phys. C, 40 (2016), p. 100001.

[260] H. Czyż, P. Kisza, and S. Tracz, *Modeling interactions of photons with pseudoscalar and vector mesons*, Phys. Rev. D, 97 (2018), p. 016006.

[261] H. Czyz and S. Ivashyn, *EKHARA: A Monte Carlo generator for $e^+e^- \to e^+e^-\pi^0$ and $e^+e^- \to e^+e^-\pi^+\pi^-$ processes*, Comput. Phys. Commun., 182 (2011), pp. 1338–1349.

[262] H. Czyz and P. Kisza, *EKHARA 3.0: an update of the EKHARA Monte Carlo event generator*, Comput. Phys. Commun., 234 (2019), pp. 245–255.

[263] K. Asai, K. Hamaguchi, N. Nagata, S.-Y. Tseng, and J. Wada, *Probing the $L_\mu - L_\tau$ gauge boson at the MUonE experiment*, Phys. Rev. D, 106 (2022), p. L051702.

[264] I. Galon, D. Shih, and I. R. Wang, *Dark photons and displaced vertices at the MUonE experiment*, Phys. Rev. D, 107 (2023), p. 095003.

[265] G. Grilli di Cortona and E. Nardi, *Probing light mediators at the MUonE experiment*, Phys. Rev. D, 105 (2022), p. L111701.

[266] S. Agostinelli et al., *GEANT4–a simulation toolkit*, Nucl. Instrum. Meth. A, 506 (2003), pp. 250–303.

[267] A. G. Bogdanov et al., *Geant4 simulation of production and interaction of muons*, IEEE Trans. Nucl. Sci., 53 (2006), pp. 513–519.

[268] R. P. Kokoulin and A. A. Petrukhin, *Analysis of the cross-section of direct pair production by fast muons*, in 11th International Conference on Cosmic Rays, vol. 29, 1970, pp. 277–284.

[269] R. P. Kokoulin and A. A. Petrukhin, *Influence of the nuclear form factor on the cross-section of electron pair production by high energy muons*, in 12th International Conference on Cosmic Rays, vol. 6, 1971, pp. 2436–2444.

[270] H. De Vries, C. W. De Jager, and C. De Vries, *Nuclear charge and magnetization density distribution parameters from elastic electron scattering*, Atom. Data Nucl. Data Tabl., 36 (1987), pp. 495–536.

[271] G. Fricke, C. Bernhardt, K. Heilig, L. A. Schaller, L. Schellenberg, E. B. Shera, and C. W. de Jager, *Nuclear Ground State Charge Radii from Electromagnetic Interactions*, Atom. Data Nucl. Data Tabl., 60 (1995), pp. 177–285.

[272] H. H. Patel, *Package-X: A Mathematica package for the analytic calculation of one-loop integrals*, Comput. Phys. Commun., 197 (2015), pp. 276–290.

[273] H. H. Patel, *Package-X 2.0: A Mathematica package for the analytic calculation of one-loop integrals*, Comput. Phys. Commun., 218 (2017), pp. 66–70.

[274] J. Heeck, R. Szafron, and Y. Uesaka, *Isotope dependence of muon decay in orbit*, Phys. Rev. D, 105 (2022), p. 053006.

[275] J. Heeck, R. Szafron, and Y. Uesaka, *Isotope dependence of muon-to-electron conversion*, Nucl. Phys. B, 980 (2022), p. 115833.

[276] I. Angeli and K. P. Marinova, *Table of experimental nuclear ground state charge radii: An update*, Atomic Data and Nuclear Data Tables, 99 (2013), pp. 69–95.

[277] E. A. J. M. Offermann, L. S. Cardman, C. W. de Jager, H. Miska, C. de Vries, and H. de Vries, *Energy dependence of the form-factor for elastic electron scattering from* ^{12}C, Phys. Rev. C, 44 (1991), pp. 1096–1117.

[278] J. A. Jansen, R. T. Peerdeman, and C. De Vries, *Nuclear charge radii of* ^{12}C *and* ^{9}Be, Nucl. Phys. A, 188 (1972), pp. 337–352.

[279] R. N. Lee, A. A. Lyubyakin, and V. A. Smirnov, *Total Born cross section of* e^+e^- *pair production by an electron in the Coulomb field of a nucleus.* arXiv 2309.02904, 9 2023.

ANALYTICAL INDEX

List of Figures

List of Tables

List of Epigraphs